SKB

Modelling and evaluation report of Task 9C Extension regarding migration of radium and radon in fractured rock

Task 9 of SKB Task Force GWFTS – Increasing the realism in solute transport modelling based on the field experiments REPRO and LTDE-SD

Johan Byegård

James Crawford

Luis Moreno

Ivars Neretnieks

Aitor Iraola

Paolo Trinchero

Kerttuli Helariutta

Marja Siitari-Kauppi

Bill Lanyon

Björn Gylling

Josep M Soler

SVENSK KÄRNBRÄNSLEHANTERING

Modelling and evaluation report of Task 9C Extension regarding migration of radium and radon in fractured rock

Task 9 of SKB Task Force GWFTS – Increasing the realism in solute transport modelling based on the field experiments REPRO and LTDE-SD

Johan Byegård[1], James Crawford[2], Luis Moreno[3], Ivars Neretnieks[3], Aitor Iraola[4], Paolo Trinchero[4], Kerttuli Helariutta[5], Marja Siitari-Kauppi[5], Bill Lanyon[6], Björn Gylling[7], Josep M Soler[8]

1 Geosigma AB
2 Kemakta Konsult AB
3 KTH
4 Amphos 21
5 Helsinki University
6 Fracture Systems Ltd.
7 Gylling GeoSolutions
8 IDAEA-CSIC

Abstract

In the modelling exercise Task 9C, which is based on the REPRO TDE (Through Diffusion Experiment), attempts are made to use diffusion models to interpret the diffusive transport of tracers between boreholes. In the extended study presented here, the developed diffusion models are used to simulate transport of radium and radon from their place of decay production in the rock matrix to the water conducting fractures. It has been proposed that the presence of radium in fracture groundwater can be indicative of interactions taking place between the matrix pore water and the fracture groundwater. This extension to Task 9C consists of a literature study, modelling results of Ra/Rn migration, results from TDE laboratory measurements, comparisons of the modelling and experimental results, comparisons to similar laboratory experiments, and inverse model calculations. The work was defined by a task description written for the SKB Task Force on modelling of Groundwater Flow and Transport of Solutes (TF GWFTS).

From the laboratory measurements of radon/radium performed on the in-situ groundwater, one can see a clear relationship between calcium concentrations in the groundwater and the Ra concentrations. This can be explained by a cation exchange competition where high calcium concentration causes release of Ra from the rock matrix. A comparison between the groundwaters from natural fractures and the TDE shows that groundwaters from the artificial 1 mm slit have significantly lower Ra concentrations.

The radon concentrations in the different groundwaters vary significantly and cannot be correlated to either depth, radium concentrations in water and/or calcium concentrations. The radon concentrations in the synthetic borehole 1-mm slit are also significantly lower than any radon concentration found in groundwater from natural fractures. Hence, there must be a mechanistic difference in the radon/radium production and diffusion in rock close to natural fractures compared to the rock matrix studied in the TDE experiment. The TDE results were also compared to studies of radon concentrations in through-diffusion-experiment cells. These experiments were targeted towards Äspö Hard Rock Laboratory conditions, but also natural fractures.

Also, one can see that both presented modelling studies overestimate the radon and radium concentrations in the TDE. For Rn, the modelling results are closer to concentrations found in natural fractures. Radium activities varies significantly and follow the Ca concentrations for most fractures. The modelling attempts seem to capture the steady state conditions for radium and radon distributions in natural fractures but are less successful in the prediction of the radon and radium mobility in the rock matrix. This is a bit unsatisfactory since the used diffusion models were developed to investigate matrix transport.

The general outcome is that the diffusion models used for the transport between the TDE boreholes cannot in their present form match the measured radon transport characteristics. One can, however, observe a closer match between the field experiment of the TDE and the laboratory experiments of radon flux. Still, it is obvious that there are some mechanisms in the in-situ matrix diffusion of radon and radium that cannot solely be reproduced by laboratory data and an ordinary diffusion model.

To obtain a better match, it is necessary to set up a model including a source of radon flux closer to the natural fractures compared to the intact rock matrix. Transfer of dissolved gasses from pore liquids to fracture and/or borehole water is difficult to reproduce in the laboratory and in in-situ experiments. A "skin effect" could possibly explain the deviations observed in this report, e.g., lack of high-pressure conditions in the laboratory experiment combined with restricted dissolved gas transfer from synthetically produced rock surfaces.

For the inverse modelling, it is necessary to invoke a very low production rate of Ra and Rn in the rock matrix to obtain a satisfactory match with the TDE data. This implies that the bulk of U enriched mineral phases are insufficiently accessible to porewater to contribute significantly to Ra and Rn production.

Sammanfattning

I modelleringsövningen Task 9C, som är baserad på REPRO TDE (Through Diffusion Experiment), görs försök att använda diffusionsmodeller för att tolka den diffusiva transporten av spårämnen mellan borrhål. I den utökade studien som presenteras här används de utvecklade diffusionsmodellerna för att simulera transport av radium och radon från deras plats för sönderfall i bergmatrisen till de vattenledande sprickorna. Det har föreslagits att förekomsten av radium i sprickgrundvatten kan tyda på interaktioner som äger rum mellan matrisporvattnet och sprickgrundvattnet. Denna utvidgning till Task 9C består av en litteraturstudie, modelleringsresultat av Ra/Rn-migrering, resultat från TDE-laboratoriemätningar, jämförelser av modellerings- och experimentresultat, jämförelser med liknande laboratorieexperiment och resultat från inversmodellering. Arbetet definierades av en uppgiftsbeskrivning skriven för SKB Task Force för modellering av grundvattenflöde och transport av lösta ämnen (TF GWFTS).

Från de laboratoriemätningar av radon/radium som utförts på grundvattnet (in-situ) kan man se ett tydligt samband mellan kalciumhalterna i grundvattnet och Ra-halterna. Detta kan förklaras av en katjonbyteskonkurrens där hög kalciumkoncentration orsakar frisättning av Ra från bergmatrisen. En jämförelse mellan grundvattnet från naturliga sprickor och TDE visar att grundvattnet från den konstruerade 1 mm slitsen har betydligt lägre Ra-koncentrationer.

Radonhalterna i de olika grundvatten varierar avsevärt och kan inte korreleras till vare sig djup, radiumhalter i vatten och/eller kalciumhalter. Radonhalterna i den 1 mm konstruerade slitsen i borrhålet är också betydligt lägre än någon radonhalt som finns i grundvatten från naturliga sprickor. Det måste därför finnas en mekanistisk skillnad i radon/radiumproduktion och diffusion i berg nära naturliga sprickor jämfört med bergmatrisen som studerades i TDE-experimentet. TDE-resultaten jämfördes också med studier av radonkoncentrationer i genomdiffusionsexperimentceller. Dessa experiment var inriktade på förhållanden i Äspölaboratoriet, men även i naturliga sprickor.

Man kan också se att de båda presenterade modelleringsstudierna överskattar radon- och radiumhalterna i TDE. För Rn är modelleringsresultaten närmare de koncentrationer som finns i naturliga sprickor. Radiumaktiviteter varierar avsevärt och följer Ca-koncentrationerna för de flesta sprickor. Modelleringsförsöken verkar fånga steady state-förhållandena för radium- och radonfördelningar i naturliga sprickor men är mindre framgångsrika i förutsägelsen av radon- och radiumrörligheten i bergmatrisen. Detta är lite otillfredsställande eftersom de använda diffusionsmodellerna utvecklades för att undersöka matristransport.

Det generella utfallet är att de diffusionsmodeller som används för transporten mellan TDE-borrhålen inte i sin nuvarande form kan matcha de uppmätta radontransportegenskaperna. Man kan dock observera en närmare överensstämmelse mellan TDE:s fältexperiment och laboratorieförsöken med radonflöde. Ändå är det uppenbart att det finns vissa mekanismer av matrisdiffusion in-situ för radon och radium som inte enbart kan reproduceras med laboratoriedata och en vanlig diffusionsmodell.

För att få en bättre matchning är det nödvändigt att sätta upp en modell som inkluderar en radonflödeskälla belägen närmare de naturliga sprickorna än den intakta bergmatrisen. Överföring av lösta gaser från porvätskor till sprick- och/eller borrhålsvatten är svår att reproducera i laboratoriet och i in-situ experiment. En "skin effect" kan möjligen förklara de avvikelser som observerats i denna rapport, t ex avsaknad av högtrycksförhållanden i laboratorieexperimentet kombinerat med begränsad överföring av löst gas från syntetiskt producerade bergytor.

För den inversa modelleringen är det nödvändigt att använda en mycket låg produktionshastighet av Ra och Rn i bergmatrisen för att få en tillfredsställande matchning med TDE-data. Detta innebär att huvuddelen av de U-berikade mineralfaserna är otillräckligt tillgängliga för porvattnet för att väsentligt bidra till Ra- och Rn-produktionen.

Contents

1 Introduction

In the REPRO TDE through diffusion experiment (Andersson et al. 2020, Soler et al. 2021) attempts are made to use diffusion models to interpret the diffusive transport of tracers from one borehole to another. This diffusion model should therefore also be a contributing part of the process of transport of uranium- and thorium-series daughter nuclides from their place of decay production in the rock matrix to the water conducting fractures. Since it has been proposed that the presence of radium in fracture groundwater can be regarded as indicative of interactions taking place between the matrix pore water and the fracture groundwater (Crawford 2010), it would be advantageous if one uses the TDE experimental setup to establish a connecting link for the transport of alpha decay daughters in the rock matrix.

This concept would therefore also give a mechanistic proof of the possibility of extending the diffusion model developed and calibrated for the across-borehole-diffusion to the case of diffusion of compounds produced in the matrix being transported to the water containing fractures. This extension to the Task 9C therefore consists of:

1) Using literature references for quantifying the process of the release of the alpha decay daughters from the crystalline lattice to the pore water, e.g., identified as a release factor and reviewed by Crawford in Chapter 2 in this report.

2) Using the developed and calibrated diffusion model in the Task 9C for the calculation of the expected ^{226}Ra and ^{222}Rn concentrations in the 1 mm slit in the observation boreholes, done by KTH and Amphos21 and presented in Chapter 3 in this report.

3) Performing and reporting measurements of radon concentrations in the TDE experiment boreholes and measure these concentrations in groundwater sampled from natural fractures, mainly performed by Helsinki University and described in Chapter 4 in this report.

4) Comparing the results from the model calculation with the experimental results, and comparisons to similar laboratory experiments, done by the editor and included in Chapter 5 in this report

5) Reverse model calculations, i.e., adjusting the model parameters to fit the measured concentrations, performed by Crawford and included in Chapter 5 in this report.

6) Concluding remarks of the task, presented in Chapter 6 in this report.

Please see Appendix A for the task description for this study performed by SKB Task Force on modelling of GroundWater Flow and Transport of Solutes (TF GWFTS).

2 Recoil processes

2.1 Background

Uranium occurs naturally in granitic rocks with an average global abundance of about 4.4 ppm although typically ranges from 1–10 ppm (Langmuir 1997). Pegmatites, on the other hand, can have uranium contents ranging from 40–90 ppm. Median values for Finnish rocks from the Olkiluoto site range from 4–6 ppm (Aaltonen et al. 2010). Similar ranges are reported for site specific rocks from the Forsmark and Laxemar investigation areas (Drake et al. 2006, Sandström and Stephens 2009). Granite from the Stripa mine is somewhat unusual in having a relatively high U content on the order of 44 ppm (Andrews et al. 1989a).

The U-content of granitic rock is not evenly distributed, however, and it tends to be enriched in matrix accessory minerals including zircon, apatite, and monazite (Eggeling et al. 2013). Uranium is also commonly present as uraninite or enriched in thorite and thorianite inclusions in biotite. In the Stripa granite, the highest concentrations have been found in opaque minerals associated with chlorite and biotite filled fractures where local concentrations of 10 000–25 000 ppm are not uncommon while concentrations ranging from 4 000–6 000 ppm are typical along grain boundaries and microfractures (Andrews et al. 1982, and references therein). The U-concentration in non-fractured quartz and feldspar mineral grains, on the other hand, was found to be negligible based on radiographic fission track analysis.

These observations appear to be typical for granitic rocks and pegmatites in general and not specific to the Stripa site. The U found within the microfractures of Stripa granite is predominantly thought to be uraninite, UO_2 (Andrews et al. 1989b), although more recent work using modern microprobe techniques (e.g., SEM-EDS) has also revealed the additional presence of (urano)thorite, haiweeite, uranophane, and coffinite hosted in microfractures of Forsmark rock samples (Krall et al. 2015). The Stripa granite, however, is likely to be an exception given that the high U-concentrations may be due to metasomatic processes that might be unusual relative to more common granitic rock types including metamorphic granites and gneiss found at Forsmark and Olkiluoto. Some typical U-rich inclusions are shown in Figure 2-1 (reproduced from Jelinek and Eliasson 2015) which also shows some typical examples of radiation damage (microfractures and alteration halos).

Radioactive disequilibrium in natural rocks and groundwater systems has been observed for many years. Typically, one finds higher $^{234}U/^{238}U$ activity ratios in groundwater that has permeated rock than that which would be predicted on the basis of secular equilibrium (i.e., $^{234}U/^{238}U \gg 1$). In Forsmark groundwater, for example, the $^{234}U/^{238}U$ activity ratio is roughly 3 ± 1 which, although higher than secular equilibrium, is not unusual. Indeed, many sampled groundwaters in Sweden and Finland have been found to have $^{234}U/^{238}U$ activity ratios in the range of 2–4 and values approaching 10 are not unknown (Suksi et al. 2006). The principal explanatory mechanism for this is the process known as alpha recoil involving daughter radionuclides of the naturally occurring decay chains, although it may be amplified by redox fractionation with larger ratios apparently associated with rapid transition of oxidising to strongly reducing groundwater conditions. Although the decay chain involving ^{238}U is the most well-studied owing to its importance for ^{222}Rn emanation from geological materials, the decay chains of ^{232}Th, and to a lesser extent ^{235}U have also been studied extensively as natural analogues.
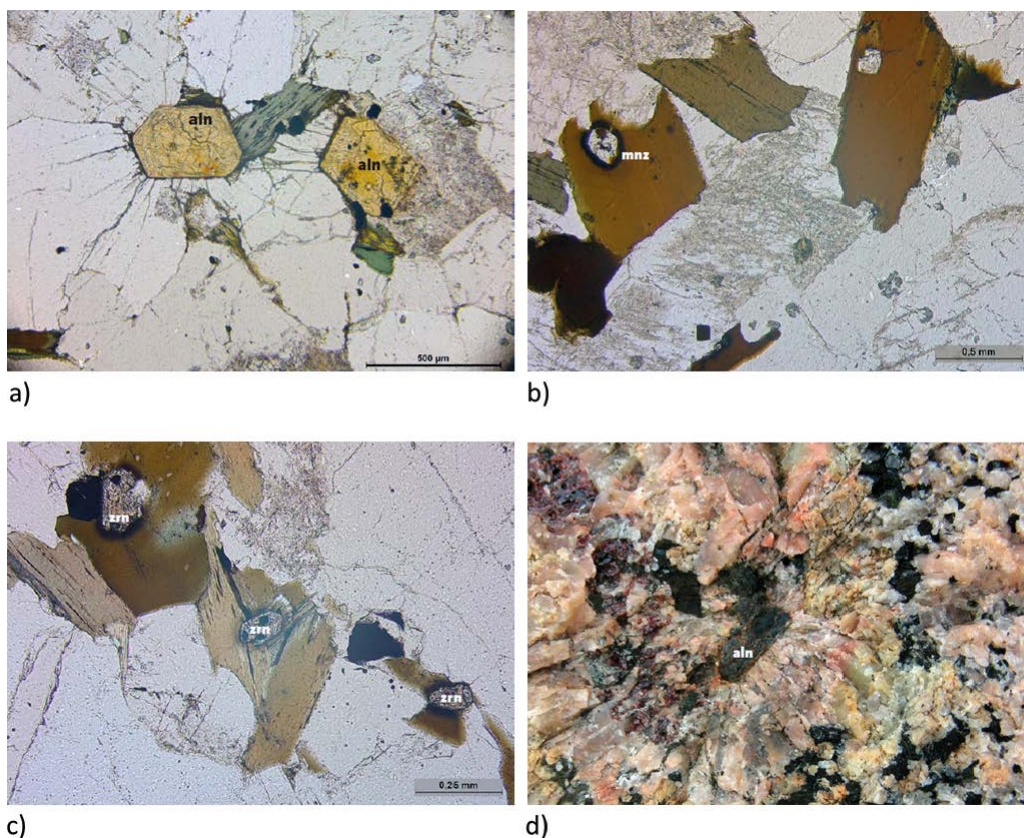
Figure 2-1. Thin section photographs of Bohus granite (a-c) and garnet-ilmenite-bearing Bohus pegmatite (d) showing crystal inclusions of U-enriched allanite (a, d) and monazite inclusions in biotite (b), and zircon inclusions in biotite (c). Note the radial microfractures surrounding allanite in response to expansion stress arising due to α-recoil damage and subsequent chemical alteration. Dark halos resulting from α-recoil damage are also visible in the biotite surrounding the monazite and zircon inclusions. Images are reproduced from Jelinek and Eliasson, 2015 (photography: Thomas Eliasson, SGU).

2.2 Porewater α-recoil capture processes

Generally, the α-decay energies of the ^{238}U and ^{232}Th chain lie in the interval 4–6 MeV. Upon decay, an equal momentum is imparted to both the α-particle itself and the daughter nucleus. Owing to the large difference in mass, however, the bulk of the decay energy is transmitted to the α-particle while only a small fraction (60–120 keV) is imparted to the daughter nuclide in the form of recoil energy (Sun and Semkow 1998). When travelling through a medium (such as a mineral crystal, water, or air) the energy of the recoiling nucleus is dissipated by elastic collisions with both nuclei of atoms in the medium as well as interactions with the electron clouds surrounding atoms. The distance over which a recoil nucleus can travel is characterised as the recoil- or stopping range. While the range of a typical α-particle in water is about 50 μm, for a recoil nucleus the range is only about 80 nm. Since the dissipation of kinetic energy in a medium is a stochastic process, there is a probability distribution associated with the recoil range. The standard deviation of the recoil range is referred to as longitudinal and lateral "straggling" for variation along the principal axes relative to the recoil trajectory.

For a radionuclide undergoing α-decay there are several different possible outcomes for the fate of the recoil nucleus depending on the location of the decaying atom in the material. If the decaying atom is close to the surface of a mineral grain, the daughter can recoil deeper into the mineral grain or be ejected into pore space surrounding the mineral grain. For the daughter nuclides that escape into the pore space, this is called "direct recoil" emanation (see arrow 1 depicted in Figure 2-2). There are, however, other possibilities. A recoil nucleus may travel sufficiently far to be implanted into an adjacent geological surface. This may cause the recoil nucleus to be effectively immobilized (arrow 2 in Figure 2-2) or, if deposited at a sufficiently shallow depth in the interface, it may be
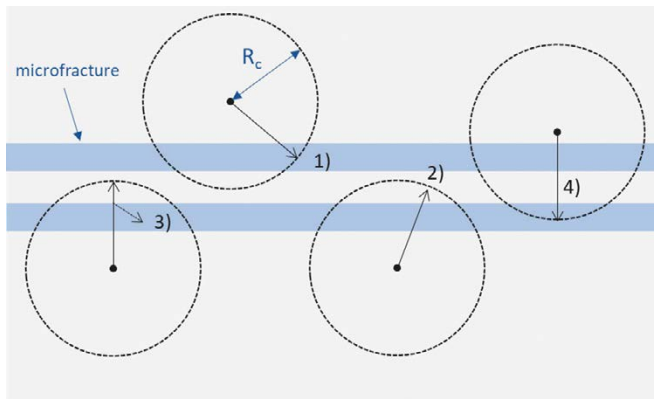
Figure 2-2. Stylised representation of recoil capture processes within a pore space (water filled microfractures) from α-decay of a radionuclide hosted in a mineral. Arrows denote: 1) direct recoil, 2) implantation, 3) indirect recoil (i.e., remobilisation of shallow implanted recoil nuclei), and 4) penetrating recoil capture. (Figure adapted from Semkow, 1991).

leached out again by diffusion through the zone of damage caused by the implantation process (arrow 3 in Figure 2-2). Atoms that are re-mobilized in this fashion are referred to as "indirect recoil" emanations. A final possibility if the medium is sufficiently fine grained relative to the stopping distance is a so-called penetrating recoil emanation (arrow 4 in Figure 2-2) where the recoil nucleus has sufficient energy to completely penetrate an adjacent mineral and be deposited in porewater adjoining its reverse side.

Recoiling atoms ejected from a mineral surface have a range of energies ranging from 0 keV up the original recoil energy of the nucleus (86.13 keV for ^{222}Rn) depending upon from how deep beneath the mineral surface the decay process occurred. For an indirect recoil process, the energy of the implanting nucleus must be less than about ~5 keV for the implanted atom to be sufficiently close to the surface to subsequently leach out into porewater (Kornelsen 1964).

It has been observed in a number of studies (e.g., Sakoda et al. 2011, Sun and Furbish 1995 and references therein) that the emanation of ^{222}Rn is frequently higher by up to a factor of 5 in water-saturated than dry samples. This is partly attributed to the greater stopping power of water since the recoil range in air is ~700 times that in water, and partly due to indirect recoil since water is thought to facilitate the out-diffusion of recoil atoms (see e.g., Fleischer 1983). When the pore space is air-filled, the ejected recoil nuclei can readily traverse the pore space and be embedded in adjacent mineral interfaces thereby giving a lower emanation fraction than what would be obtained if the pore space were fully water saturated. Semkow (1991) invokes penetrating recoil and fractal argumentation to explain higher than expected emanation rates as a function of grain size that cannot be explained adequately by the indirect recoil mechanism.

The emanation of ^{222}Rn is complicated by the fact that there are four α-decay events in the decay chain between ^{238}U and ^{222}Rn. Radionuclides preceding ^{222}Rn (i.e., ^{234}Th, ^{230}Th, ^{226}Ra) that are ejected by α-recoil from a solid may be re-adsorbed to surfaces, or form surface precipitates in the pore space surrounding U-enriched mineral grains. Furthermore, the daughter radionuclides following ^{238}U will be depleted in the surface zone of the U-enriched mineral grains due to each successive α-recoil, implying that the rate of ^{222}Rn emanation will be less than that predicted by assuming secular equilibrium throughout the mineral grain.

In principle, the main U-bearing mineral phases such as uraninite (referred to here as a "primary reservoir") can also dissolve in pore water up to their solubility limit and become a disseminated source of daughter radionuclides in the rock matrix (both sorbed and freely dissolved). For a typical granite, however, the rate of production by this mechanism is likely to be less than the rate of production from the primary reservoir.

Each successive α-decay event is associated with its own porewater α-recoil capture probability and implantation probability. In general, it is necessary to take these factors into account when estimating the net emanation rate of ^{222}Rn corresponding to the fourth α-recoil event (see, for example, Sun and Semkow 1998). If the rate of primary reservoir production (i.e., direct emanation of ^{222}Rn from ^{238}U

enriched mineral grains) can be shown to be much greater than the disseminated rate of production, then it might be reasonable to neglect multiple recoil fractionation. If calculations only consider the production of ^{222}Rn directly from the measured activity of ^{226}Ra in the rock, on the other hand, then only one α-recoil event needs to be considered. The distribution of ^{226}Ra in the rock then needs to be accounted for, however, since this may differ from the distribution of ^{238}U in the rock matrix.

2.3   Theoretical models of porewater α-recoil capture

There are many theoretical models for α-recoil capture in the literature. Some of these are summarised in Table 2-1. In principle, all assume a single α-recoil process from a parent radionuclide contained in a solid phase (primary reservoir). As noted above, however, if the rate of primary production is sufficiently high and surface layer daughter depletion can be presumed negligible, then they may be sufficiently accurate to estimate ^{222}Rn production directly from the bulk ^{238}U content if secular equilibrium is additionally assumed. Most of the equations given in Table 2-1 assume a uniform distribution of radionuclide in the primary reservoir. The equations from Key et al. (1979) and Semkow (1990), however, specifically consider the case of Ra-mineral coatings on spherical particles for the estimation of ^{222}Rn emanation. This might be more appropriate if measured Ra-activities are used as the basis of calculations instead of ^{238}U in which case assuming uniform Ra-activities in the primary mineral phases might underestimate the true emanation fraction of ^{222}Rn.

Since many of the equations given in Table 2-1 are for very specific geometric situations and particle shapes, they are less useful in the general case where there is very little information concerning morphology of the primary U-bearing minerals and their location in the rock matrix. The most general formula ("B84") given by Bossus (1984) makes no particular assumption about U-bearing mineral morphology apart from the underlying assumptions that 1) the characteristic particle dimension is greater than the recoil distance in the mineral, and 2) the scale of surface roughness incorporated in the specific surface area measurement is smaller than the recoil distance in the mineral. It can be noted that the B84 formula should give the maximum rate of ^{222}Rn emanation assuming no implantation in adjacent mineral interfaces. It can be interpreted as an upper limit for uniformly distributed parent radionuclides in a mineral grain. The formula ("S91") by Semkow (1991) is useful if additional information about the fractal nature of the primary U-bearing mineral surface is known, although in the limit of D = 2 (Euclidian case), the result simplifies to the same formula as B84.

The formula ("LN94") given by Liu and Neretnieks (1994) has similar underlying assumptions as the B84 formula although additionally assumes that the film of porewater with thickness, b surrounding individual mineral grains is much less than the recoil distance in water ($b \ll R_w$) and that the porewater film thickness is proportional to particle size. The formula, however, considers the reduction in ^{222}Rn emanation arising due to implantation effects. Provided the porosity in the immediate vicinity of the primary U-bearing mineral can be approximately estimated, this might be useful for setting more realistic bounds on the emanation fraction.

Another aspect of theoretical calculation of α-recoil capture that might be relevant is that the formulae given in Table 2-1 typically only consider single characteristic particle sizes. In general, smaller particles with higher surface to volume ratios will emanate ^{222}Rn more effectively than larger particle sizes. This might need to be considered explicitly in calculations since an average U-bearing grain size (and average porosity) may not be representative for the bulk ^{222}Rn emanation fraction.

Table 2-1. Some theoretical expressions used to estimate emanation coefficients, η for porewater α-recoil capture of radionuclides in geological materials.

Formula	Geometry	Reference
$$\eta = \frac{3}{4}\frac{R_c}{r_0} - \frac{1}{16}\left(\frac{R_c}{r_0}\right)^3$$ r_0 is the particle radius, R_c is recoil range in solid.	Sphere $2r_0 \geq R_c$ (unconfined)	Flügge and Zimens (1939), Kigoshi (1971)
$$\eta = \Lambda_i f_s + \left(\Lambda_r + \Lambda_0^2\right) f_u + \Lambda_0 f_h$$ $$\Lambda_i = \frac{3}{4}\frac{R_c}{r_0} - \frac{1}{16}\left(\frac{R_c}{r_0}\right)^3 \quad 2r_0 \geq R_c$$ $$\Lambda_r = \begin{cases} \dfrac{1}{8} + \dfrac{1}{24}\dfrac{R_c}{r_0} & R_c \leq r_0 \\[2ex] \dfrac{15}{24} - \dfrac{4}{24}\dfrac{r_0}{R_c} - \dfrac{7}{24}\dfrac{R_c}{r_0} & R_c > r_0 \end{cases}$$ $$\Lambda_0 = \frac{1}{2}\left(1 + \frac{R_c}{2r_0}\right)$$ f_s = fraction of supported ^{226}Ra (uniformly distributed in primary reservoir); f_u = fraction of surface sorbed ^{226}Ra derived from unsupported, surface sorbed ^{230}Th; f_h = fraction of surface sorbed unsupported ^{226}Ra of exogenous origin	Surface-coated sphere (unconfined)	Key et al. (1979)
$$\eta = \frac{1}{4} A_s \rho_c R_c$$ A_s is the specific surface area (m^2/kg) of the primary radionuclide-bearing phase, ρ_c is crystallographic density of the solid.	Euclidian solid $r_0 > R_c$ (unconfined)	Bossus (1984)
$$\eta = \frac{\left(2 - \dfrac{d}{R_c} + \dfrac{R_c}{r_0}\left(1-\dfrac{d}{R_c}\right)^2 - \dfrac{R_c d}{12 r_0^2}\left(1 + \left(1-\dfrac{d}{R_c}\right)\left(5 - 3\dfrac{d}{R_c}\right)\right)\right)}{4\left(1 - \dfrac{d}{r_0} + \dfrac{1}{3}\left(\dfrac{d}{R_c}\right)^2\right)}$$ d is the thickness of surface layer	surface-coated sphere $2r_0 \leq R_c$ $0 \leq d \leq 2r_0 - R_c$ (unconfined)	Semkow (1990)
$$\eta = \frac{\left(1 - \dfrac{d}{r_0} + \dfrac{1}{3}\left(\dfrac{d}{r_0}\right)^2 - \dfrac{r_0}{3d}\left(1 - \dfrac{3}{4}\dfrac{R_c}{r_0} + \dfrac{1}{16}\left(\dfrac{R_c}{r_0}\right)^3\right)\right)}{4\left(1 - \dfrac{d}{r_0} + \dfrac{1}{3}\left(\dfrac{d}{R_c}\right)^2\right)}$$	surface-coated sphere $2r_0 \leq R_c$ $2r_0 - R_c \leq d \leq R_c$ (unconfined)	Semkow (1990)
$$\eta = \frac{R_c\left(1 - \dfrac{1}{12}\left(\dfrac{R_c}{r_0}\right)^2\right)}{d\left(1 - \dfrac{d}{r_0} + \dfrac{1}{3}\left(\dfrac{d}{R_c}\right)^2\right)}$$	surface-coated sphere $2r_0 \leq R_c$ $R_c \leq d$ (unconfined)	Semkow (1990)
$$\eta = \frac{C}{4-D}\left(\frac{R_c}{2r_0}\right)^{3-D}$$ $$\frac{S}{V} = C r_0^{D-3} a^{D-3}$$ C is a shape coefficient (C = 1 for a plate); S/V is the surface to volume ratio; D is the fractal dimension	solid with fractal surface (unconfined)	Semkow (1991)

Formula	Geometry	Reference
$$\eta = \frac{1}{4}\left(\frac{2^{D-1}}{4-D}\left(\frac{a}{R_c}\right)^{D-2}\right)R_c A_s \rho_c$$ a is diameter of the adsorbate molecule used in the BET determination of specific surface area, A_s (3.5Å for N_2); D is the fractal dimension	Solid with fractal surface (unconfined)	Semkow (1991), Bourdon et al. (2009)
$$\eta = \frac{3}{8}\left(\frac{\varepsilon_p}{1-\varepsilon_p}\right)\frac{R_c}{R_w}$$ R_w is the recoil range in water, ε_p is the local porosity surrounding the U-enriched solid	Euhedral $r_0 > R_c$ [1] (confined pore space)	Liu and Neretnieks (1994)
$$\eta = \frac{1}{8}R_c\frac{K}{r_0}\lambda_r$$ K = 6 for sphere; λ_r = surface roughness factor; for shape factors of prolate spheroids and other forms see: Cartwright (1962)	Spheroidal (unconfined)	Lee et al. (2010)
$$\eta_S = \left(\frac{1}{2}-\frac{3\left(4r_0^2+3R_c^2-8r_0R_c\right)}{16\left(3r_0^2-3r_0R_c+R_c^2\right)}\right)\cdot\left(\frac{r_0^3-(r_0-R_c)^3}{r_0^3}\right)$$	Single sphere (unconfined)	Stajic and Nikezic (2014)
$$\eta_{PS} = \eta_S \cdot \frac{\int_0^{L_w}\varpi(\xi)d\xi}{R_w}$$ $$\varpi(\xi)=\frac{N}{8r_0R_w^2}\left(\left(1-\frac{t_2^2}{3r_0^2}\right)(t_1^3-t_2^3)-3t_2^2(t_1-t_2)+\frac{t_1^5-t_2^5}{5r_0^2}\right)-\frac{N-2}{2}$$ $$t_1 = r_0+R_w$$ $$t_2 = \sqrt{r_0^2+R_w^2}$$ Note: N is the coordination number for spherical packing, e.g. N = 6 (simple packing), 8 (BCC, body-centred cubic packing), 12 (FCC, face-centred cubic packing)	Packed spheres of constant size $r_0 \geq \frac{R_w}{\sqrt{3}-1}$ (confined pore space within packed volume)	Stajic and Nikezic (2014)

[1] See text for additional assumptions concerning the formula given by Liu and Neretnieks (1994).

2.4 Measurements of ^{222}Rn emanation fraction reported in the literature

There are many references in the literature reporting exhalation rates of ^{222}Rn (i.e., outgassing flux) in geological materials (see, e.g., Cameron 1987, Sakoda et al. 2011 and references therein). These are typically reported as mass (Bq/kg×h) or surface area normalised units (Bq/m^{2}h) at equilibrium. Although exhalation and emanation are synonymous terms, the amount of ^{222}Rn that out-gasses from a sample is typically referred to as the exhalation flux or rate in the literature, whereas emanation fraction is used to describe the fraction of out-gassing ^{222}Rn relative to the total production in the sample. The emanation fraction for a bulk sample is, at least in principle, always less than the recoil capture fraction since the former includes the additional effect of delayed transport and decay in the porosity of the sample during out-gassing. If the total ^{226}Ra activity in the rock is known, it is possible to simply estimate the emanation fraction (or, emanation coefficient) as the ratio of Rn exhalation to total Rn production in the rock. The total Rn production in the rock can be taken to be equal to the ^{226}Ra activity). Care needs to be taken, however, since if the ^{226}Ra or ^{238}U content is measured with γ-spectroscopy using the γ-lines of the ^{214}Pb/^{214}Bi radon descendants, the activity will be underestimated. This is because one is only measuring the ingrowth of descendants from trapped ^{222}Rn and the fraction lost by exhalation then needs to be explicitly considered in the estimate (Al-Jarallah et al. 2005).

In a great many cases for the data reported in the literature, samples are crushed and sieved to small size fractions to reduce equilibration time, or otherwise simplify interpretation. Measurements are mostly made on dry, or nominally unsaturated samples as they would be used in construction materials, although some are reported for saturated, or partially water saturated states (see e.g., Sakoda et al. 2011). Some literature data are reproduced in Figure 2-3, Figure 2-4, and Figure 2-5 for different granitic rock types. In general, there is a significant spread of emanation coefficients reported, although the data mostly fall in the range 1–30 %. Figure 2-3 shows emanation coefficients from some crushed samples (< 0.5 mm) of porphyritic biotite granite taken from Pereira et al. (2017)[1] for porphyritic biotite granite from Almeida, in central Portugal (henceforth, PLM17). Here, it is important to consider that the emanation fraction on the level of individual porespace-adjacent grains in the rock is less than the bulk emanation fraction which additionally includes transport attenuation due to diffusive transport delay through the pore space (i.e., decay of ^{222}Rn during diffusive transport in pores).

This data set is interesting in that the water saturation porosity of the rock was measured as well as the ^{226}Ra content. The ^{226}Ra activity was estimated from the ^{214}Bi peak (1 764.5 keV) using γ-spectroscopy assuming secular equilibrium. It is not clear, however, whether the reported ^{226}Ra measurements are corrected for the ^{226}Rn emanation loss. Some of the core samples taken from the deep borehole at Almeida and are hydrothermally altered, while others are sampled from surface outcrops of the same rock type. The emanation coefficient measured by Pereira et al. (2017) appears to be positively correlated with water saturation porosity in Figure 2-3 (measured prior to crushing), and negatively correlated with Ra-content in Figure 2-4. The negative correlation of the PLM17 data with Ra-content is much weaker than the correlation with porosity. The authors speculate that the negative correlation may be partly due to the data representing two distinct sub-populations and that surface samples with low Ra-content may be more strongly weathered and thus depleted of uranium content. While a clear proportionality between ^{226}Ra content and ^{222}Rn exhalation rate is expected, the correlation between ^{226}Ra content and the ^{222}Rn emanation coefficient may or may not be mechanistic and related to alteration status and increased porosity with greater weathering.

The data shown in Figure 2-5, on the other hand, appear to show a weak positive correlation with Ra-content. The data in this figure are from various sources including: Al-Jarallah et al. (2005) who studied granite tablets used as construction materials (AJRM05); Baretto (1971) studied crushed samples of various US granites from different geographical locations (B71); and data compiled by Jelinek and Eliasson (2015) for macadam derived from Swedish granite, veined gneiss, and gneiss granite (JE15). The remaining data (blue symbols in Figure 2-5) are an assortment including: Polish granite and gneiss granite (Przylibski 2000); core samples of porphyritic biotite granite from Pereira et al. (2017); granite, granodiorite, quartz monzonite gneiss, and diorite from Sakoda et al. (2011); granite and other non-specified igneous rock from Hassan et al. (2009); granite samples from various countries as studied by Nicolas et al. (2014). Most of the data sets are based on measurements of finely crushed rock except those reported by Al-Jarallah et al. (2005) and Nicolas et al. (2014) which are based on intact tablets or core samples. The data reported by Jelinek and Eliasson (2015) are for comminuted macadam samples (cm-size) although otherwise relatively intact. There appears to be a relatively good correlation between ^{226}Ra content and emanation coefficient for the Swedish rocks as can be seen from the best fit correlation in Figure 2-5, although the number of samples is quite small.

---

[1] The data were digitised from a screen capture of the original figures in the pdf version of the article using a desktop version of the WebPlotDigitizer tool (https://automeris.io/WebPlotDigitizer/).
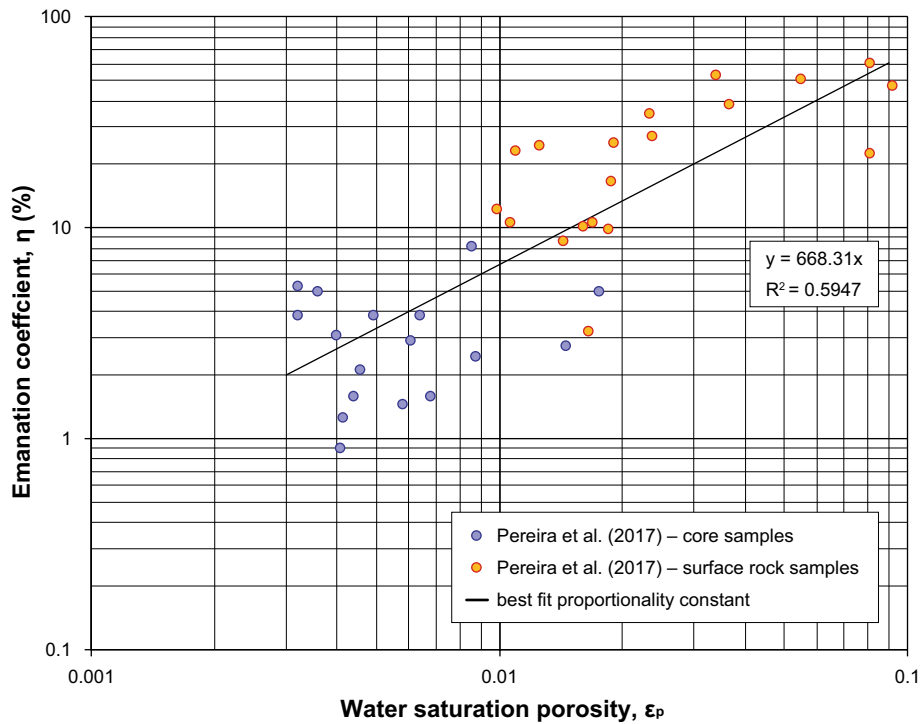
Figure 2-3. *Co-variation of estimated emanation coefficient relative to water saturation porosity for porphyritic biotite granite (Pereira et al. 2017). The high porosities of the surface rock samples appear to be associated with higher degrees of alteration, although this is not stated unambiguously in the reference. Note: data are scanned from the original reference.*
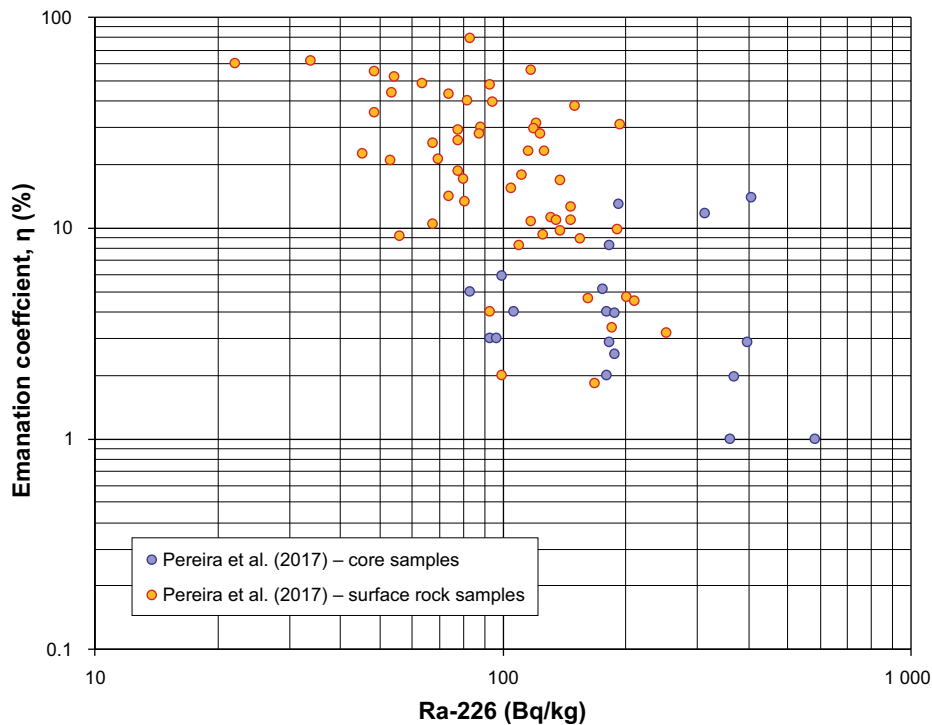
Figure 2-4. *Co-variation of estimated emanation coefficient relative to ^{226}Ra content for porphyritic biotite granite (Pereira et al. 2017). Note: data are scanned from original reference.*
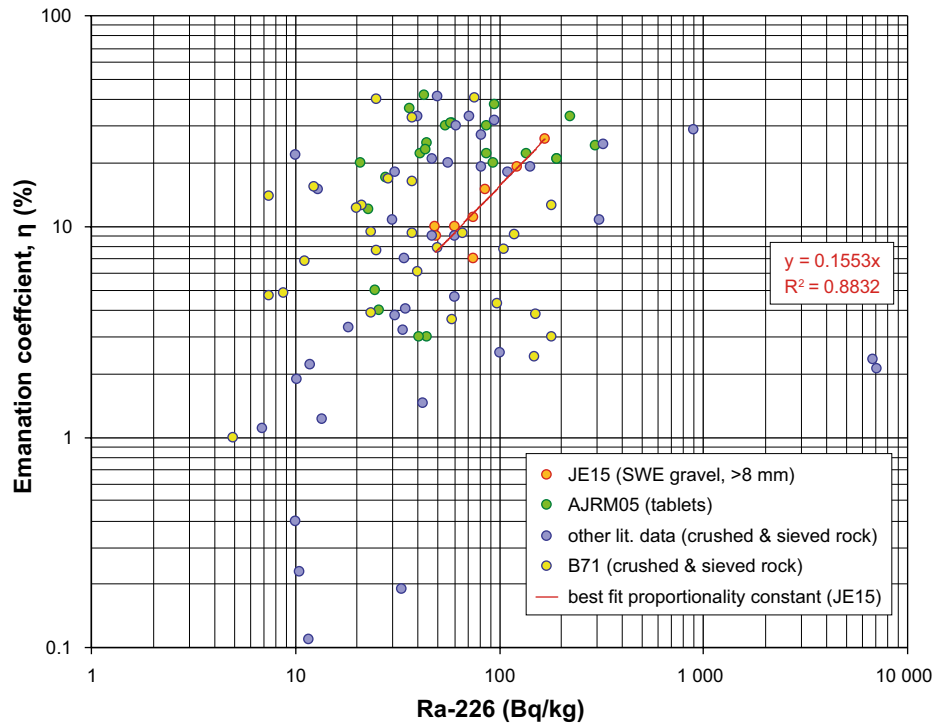
Figure 2-5. *Co-variation of estimated emanation coefficient for ^{222}Rn relative to the ^{226}Ra content reported by various authors (see text for additional details) as well as samples of Swedish granite and gneiss-granite macadam, labelled JE15 (Jelinek and Eliasson 2015). A fit is also shown for the JE15 data set showing an apparent proportionality of the emanation coefficient with Ra-content.*

3 Predictive modelling

3.1 Modelling by KTH

3.1.1 Summary

The radium and radon activities in the borehole sections in the REPRO Through-Diffusion Experiment (TDE) in ONKALO in Finland have been predicted by modelling the out-diffusion of the nuclides from the rock matrix. There are two main uncertainties, namely the emanation factor, i.e. what fraction of the activity in the rock matrix that resides in the pore water and the surface sorption coefficient of radium on the recently created surfaces on the borehole. The emanation factor is probably somewhere between 0.01 and nearly 1. The surface sorption coefficient is estimated from measurements on intact granite cores from Sweden. In addition, there are uncertainties in the diffusion and sorption coefficients. It cannot be ruled out that the total uncertainty may span more than two orders of magnitude. Nevertheless, the predicted activities lie within the wide range of observation in waters from connected fractures from two Swedish sites at Forsmark and Laxemar.

3.1.2 Introduction

In the REPRO TDE experiment a series of holes were drilled into the rock from a niche. Some boreholes were supplied with a 1 m long section with a dummy forming a concentric slot in which water was circulated. It was possible to monitor radionuclide concentrations in the circulating water. In two boreholes radium and radon activities were monitored over about 2 years. The rock that is very old contains about 7 ppm uranium-238. Over time the radionuclides in the decay chain have built up a steady state concentration of among other ^{226}Ra and ^{222}Rn. Their activities in the rock are estimated to be around 90 Bq/kg. The rock porosity is around 0.5–1 %. Emanation coefficients η, the fraction residing in the porewater, usually range from about 1 % to nearly 100 %. If all the nuclides were to have collected in the pore water the activity would be between 2 and 4×10^7 Bq/m^3 porewater.

When boreholes are drilled in the rock and water is circulated in them the nuclides diffuse from the porewater to the circulating water. Radium that enters the closed off borehole section with the dummy will partly remain in the water and partly sorb on the borehole wall with a surface retardation factor R$_s$.

Radon from the porewater also diffuses from the matrix to the circulating water and accumulates there. In addition, radon is also produced by the radium in the circulating water and by the radium sorbed on the borehole surface.

For each species the concentration of these species in the circulating water is denoted by $c_w(t)$. A concentration profile $c_p(t, x)$ in the porewater develops in the rock matrix with low concentration at the borehole surface and increasing concentration further into the rock.

3.1.3 Equations

The concentration $c_w(t)$ that builds up by the nuclides diffusing out from the matrix partly decays. The sorbing species will also reversibly sorb to the walls of the borehole. Borehole surfaces are assumed to be created from the broken crystals during the drilling process and they have not been exposed to any radionuclides from the pore water. For the *pore water* a mass balance results in the following equation for the nuclides. It will be explored if it is a reasonably fair approximation to use linear diffusion although it is cylindrically radial around a borehole because during the short time of the experiment the penetration depth is not very large compared to the borehole radius. This will facilitate to develop analytical solutions.

For both nuclides, radium and radon, in the rock matrix the same equation applies although with different material properties

$$R_d \frac{\partial c_p}{\partial t} = D_p \frac{1}{r^\alpha} \frac{\partial \left(r^\alpha \frac{\partial c_p}{\partial r} \right)}{\partial r} - \lambda R_d c_p + q_{mother}\, \eta \qquad (3\text{-}1)$$

c_p is the concentration of the nuclide in the pore water, D_p the pore diffusion coefficient, λ the decay constant and R_d the retardation factor in the rock matrix, which is the ratio of the total amount of the nuclide residing in the rock matrix compared to that in the pore water. η is the emanation factor, which denotes the fraction of atoms that have settled in the water film surrounding the crystals. q_{mother} is the production rate of radium and radon respectively. It is the activity of each nuclide in the [238]U decay chain and is the same for all of them because secular equilibrium has long been established.

For $\alpha=0$ the diffusion in the matrix is linear and for $\alpha=1$ diffusion is radially symmetric. For short penetration depths compared to the radius of the cylindrical hole the diffusion can be simplified to be linear. This has some advantages when wanting to devise analytical solutions, which are simpler and more easily show how different parameters influence results. We will use both formulations.

The first term in (3-1) accounts for the rate of accumulation of the nuclide in the rock matrix. The second term gives the rate of change due to diffusion in the pore water. The third term gives the rate of depletion by radioactive decay and the last term the rate of production of the nuclide by the decay of the mother nuclide.

The initial condition is

IC1: $c_p(t = 0,\mathrm{r}) = c_{p,o}$ (3-2)

$c_{p,o}$ is the concentration in the pore water at secular equilibrium.

The boundary conditions are

BC1: $c_p(t, r = r_{in}) = c_w(t)$ (3-3)

BC2: $c_p(t, r \to \infty) = c_{p,o}$ (3-4)

It is the same as the initial concentration in the rock given in Equation (3-2).

The mass balance equation for the circulating water, assumed to circulate so rapidly that it is essentially fully mixed.

For the sorbing nuclide, radium

$$VR_{s,Ra}\frac{\partial c_{w,Ra}}{\partial t} = N_{Ra} - VR_{s,Ra}\lambda c_{w,Ra}$$ (3-5)

where N is the rate of inflow from the rock matrix to the circulating water and R_s is the surface retardation factor. V is the volume of circulating water. The subscripts Ra and Rn stand for [226]Ra and the [222]Rn respectively

$$N_{Ra} = -AD_{p,Ra}\varepsilon \frac{\partial c_{p,Ra}}{\partial r}\bigg|_{r=r_{in}}$$ (3-6)

r_{in} is the radius of the borehole. A is the area of the interface of the borehole section. ε is the porosity of the rock.

For the non-sorbing radon $R_{s,Rn} = 1$

$$V\frac{\partial c_{w,Rn}}{\partial t} = N_{Rn} - V\lambda c_{w,Rn} + VR_{s,Ra}\lambda c_{w,Ra} = N_{Rn} - V\lambda c_{w,Rn} + Vq_{w,Ra}$$ (3-7)

$q_{w,Ra}$ is the rate of production of radon by decay of radium in the water in the slot and sorbed on the slot surface.

$$N_{Rn} = -AD_{p,Rn}\varepsilon \frac{\partial c_{p,Rn}}{\partial r}\bigg|_{r=r_{in}}$$ (3-8)

We note that of the nuclides in the decay chain uranium and thorium have extremely low solubilities in the reducing waters in the crystalline rock and only radium and radon are mobile by molecular diffusion in the pore waters. Only these nuclides will therefore be treated.

3.1.4 Data used in the simulations

The data used in the simulations are shown in Table 3-1 and Table 3-2.

Table 3-1. Half-lives and decay constants of the last three nuclides in the ^{238}U decay chain.

Nuclide	Half-life yr	Decay constant yr^{-1}
^{230}Th	75 000	9.2×10^{-6}
^{226}Ra	1 600	4.3×10^{-4}
^{222}Rn	0.0125 (3.82 days)	55.5

Table 3-2. Other data used in the examples.

| Entity	Value	Comment
a_R	21	Specific surface of rock matrix, m^2/kg (André et al. 2008, 2009)
A	0.178	Surface area borehole section m^2
a_{Rock}	90.8	Activity at steady state of nuclides in the rock Bq/kg
$a_{p,o}$	$\eta\, \rho\, a_{Rock}/\varepsilon = \eta \times 3.5 \times 10^7$	Activity at steady state of nuclides that have escaped to the pore water Bq/m^3 water. They reside in water and as sorbed
b	$\frac{V}{A} = 0.00176$	Volume to surface ratio of slot in which water circulates m
c_U	7.3×10^{-6}	Uranium concentration in rock kg/kg
$D_{p\ Radium}$	2.9×10^{-11}	Diffusion coefficient m^2/s
$D_{p\ Radon}$	6.1×10^{-11}	Diffusion coefficient m^2/s
$K_{a,\ Radium} = K_{d,\ Radium}/a_R$	3.33×10^{-3}	Surface sorption coefficient m
$K_{d,\ Radium}$	0.07	Mass sorption coefficient m^3/kg
r_{in}	0.0285	Borehole radius m
$R_s = 1 + K_{d,\ Radium}/a_R/b$	3.2	Surface retardation factor
$R_d = 1 + K_{d,\ Radium}\frac{\rho}{\varepsilon}$	27 000	Retardation factor radium in rock matrix
V	0.313×10^{-3}	Volume of circulating water m^3
ε	0.007	Porosity of rock
η	0.01 to 1	Emanation factor
ρ	2 700	Rock density kg/m^3

3.1.5 Some simplifying assumptions and solution techniques

The four differential equations, one Equation (3-1) for Ra, one Equation (3-1) for Rn and Equations (3-5) and (3-7) together with the appropriate initial and boundary conditions are solved simultaneously. Two methods are used. One uses Comsol Multiphysics®. The other uses Laplace transform and a numerical inversion technique. This is done to ensure that that the two solution methods give the same results. The equations are also solved fully analytically for steady state conditions, i.e. for very long times. This gives an additional test to see that the other methods converge to steady state.

In addition, tests are made to explore how sensitive the results are to uncertainties in some parameters that have a natural variability and also where they have had to be estimated from data from other sites and information sources. The surface retardation factor is estimated to be 3.2 from measurements of whole rock pieces (André et al. 2008, 2009). It should be noted that this is from Swedish granite, which may be different compared to rock at the REPRO site.

3.1.6 Solving by Comsol Multiphysics

Circulating water and the porewater in the rock around the slot were modelled using Comsol Multiphysics. The system is composed of a cylindrical shell and a cylindrical rock volume around the slot. Therefore, the system is modelled using axis symmetrical geometry as shown in Figure 3-1. The slot volume is taken as the volume of the circulating water in the drillhole PP327, which has a volume of circulating water of 3.13×10^{-4} m^3. An extremely fine mesh is used (more than 200 000 nodes) with a run time less than 1 minute.
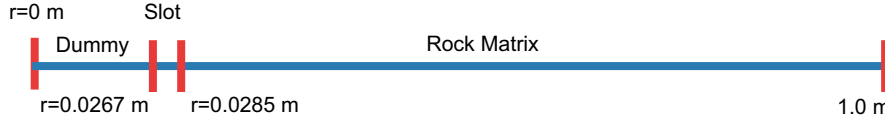
Figure 3-1. *The axis symmetric system is formed by rotation of the blue line around r=0 m.*

3.1.7　Solving by Laplace transformation

We solve the equations using Laplace transformation, which reduces the partial differential equations (PDE) for nuclide migration in the matrix pore water in time, t, and space, r, to ordinary differential equations (ODE) in only the space variable, x. These ODE's have analytical solutions, which are then transformed back to t-space by numerical inversion of the Laplace transformed solutions. In the equations below the transformed variables for pore water $\widetilde{c}_p$ and for slotwater $\widetilde{c}_w$ denote either radium or radon concentrations. We show only the equations for the linear approximation case and denote the distance from the surface of the hole by x.

Laplace transformation of (3-1) gives, because the system after long time has reached steady state and that the source term q_m, the production by the mother, is constant.

$$R_d(s\widetilde{c}_p - c_p(t=0)) = D_p\frac{\partial^2 \widetilde{c}_p}{\partial x^2} - \lambda R_d\widetilde{c}_p + \frac{q_m}{s} \tag{3-9}$$

With $c_{po} = c_p(t=0)$ the solution to this ODE is

$$\widetilde{c}_p(x) = \frac{q_m + c_{po}R_d s}{sR_d(s+\lambda)} + C1\,e^{+x\sqrt{(R_d(s+\lambda)/D_p)}} + C2\,e^{-x\sqrt{(R_d(s+\lambda)/D_p)}} \tag{3-10}$$

From boundary condition (3-4) at $x \to \infty$, $C1 \equiv 0$ and (10) reduces to (3-11)

$$\widetilde{c}_p(x) = \frac{q_m + c_{po}R_d s}{sR_d(s+\lambda)} + C2\,e^{-x\sqrt{(R_d(s+\lambda)/D_p)}} \tag{3-11}$$

Equations (3-5) and (3-7) are Laplace transformed and rewritten to one equation valid for both nuclides

$$\widetilde{c}_w s - c_w(t=0) = \frac{AD_p\varepsilon}{VR_s}\frac{\partial \widetilde{c}_p}{\partial x}\Big]_{x=0} - \lambda\widetilde{c}_w + \widetilde{qw_m} \tag{3-12}$$

The subscript m in qw_m stands for mother nuclide. For brevity we omit subscripts Ra and Rn on the concentrations.

$c_w(t=0) = 0$ as the slot is filled with pure water initially.

where the production in the water in the slot by the mother, $\widetilde{qw_m}$ is

$$\widetilde{qw_m} = R_{s,m}\lambda_m\widetilde{c_{w,m}}$$

By introducing $G = \frac{AD_p\varepsilon}{VR_s}$

$$\tag{3-13}$$

the concentration in the slot water can be written

$$\widetilde{c_w} = \frac{G}{(s+\lambda)} + \frac{\widetilde{qw_m}}{(s+\lambda)} \tag{3-14}$$

The gradient at the borehole wall, x=0 is obtained by differentiating (3-11)

$$\frac{\partial \widetilde{c}_p}{\partial x}\Big]_{x=0} = -\sqrt{\frac{R_d}{D_p}(s+\lambda)}\,C2 \tag{3-15}$$

Introducing (3-15) in (3-14) gives

$$\widetilde{c_w} = -\frac{G}{(s+\lambda)}\sqrt{\frac{R_d}{D_p}(s+\lambda)}\,C2 + \frac{\widetilde{qw_m}}{(s+\lambda)} \tag{3-16}$$

Noting that the concentration in the slot $\widetilde{c_w}$ is equal to that on the porewater at x=0, $\widetilde{c}_p(0)$ and introducing (3-11) in (3-16) gives

$$-\frac{G}{(s+\lambda)}\sqrt{\frac{R_d(s+\lambda)}{D_p}}\,C2 + \frac{\widetilde{qw_m}}{(s+\lambda)} = \frac{q_m + c_{po}R_d s}{sR_d(s+\lambda)} + C2 \tag{3-17}$$

This gives the integration constant $C2$.

$$C2 = \frac{\frac{\widetilde{qw_m}}{(s+\lambda)} - \frac{q_m + c_{po}R_d s}{sR_d(s+\lambda)}}{\left(1 + \frac{G}{(s+\lambda)}\sqrt{\frac{R_d(s+\lambda)}{D_p}}\right)} \tag{3-18}$$

We have then one Equation (3-16) for radium and one for radon for the slot water each with an integration constant $C2_{Ra}$ and $C2_{Rn}$.

The solubility of the thorium mother of radium is extremely low and $\widetilde{qw}_{Th} = 0$. This gives the Ra concentration and thus also $\widetilde{qw}_{Ra}$ which is needed to determine $C2_{Rn}$.

A similar solution was derived for the radial case. In place of Equation (10) which contains exponential functions, the radial case gives Bessel functions. This solution was found to be sensitive to the choice the distance to the far away boundary.

3.1.8 Results

Using Comsol

Activity in the circulating water

Figure 3-2 shows the activities in the circulating water. Radon activity approaches the equilibrium in about one month. For radium the equilibrium is practically reached after a few decades.

The activities in the matrix far away from the slot are also checked, and the same values as those used as initial value (secular equilibrium) are found. Figure 3-2 shows how the activities of Ra and Rn in the circulating water in the slot evolve over time.

Activity profiles

The slot and rock matrix activity profiles for radium and radon are shown in Figure 3-3. The horizontal axis shows the distance from the left covering the slot where the concentration is constant, extending to the right into the rock matrix, where the concentration increases to that for the secular equilibrium. The activity for radium in the rock matrix changes in the first few mm, since a large reservoir of radium is sorbed in the crystal surfaces in the matrix due to its very large retardation factor. Radon activity changes over a distance of about 3 cm, since radon is only present in the pore water and is not retarded by sorption.
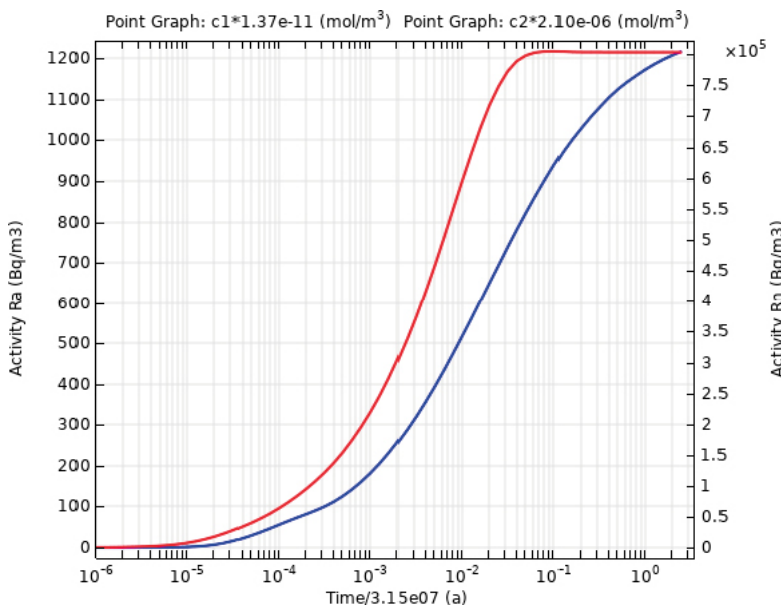
Figure 3-2. *Activity in the circulating water. Blue line for radium and red line for radon.*
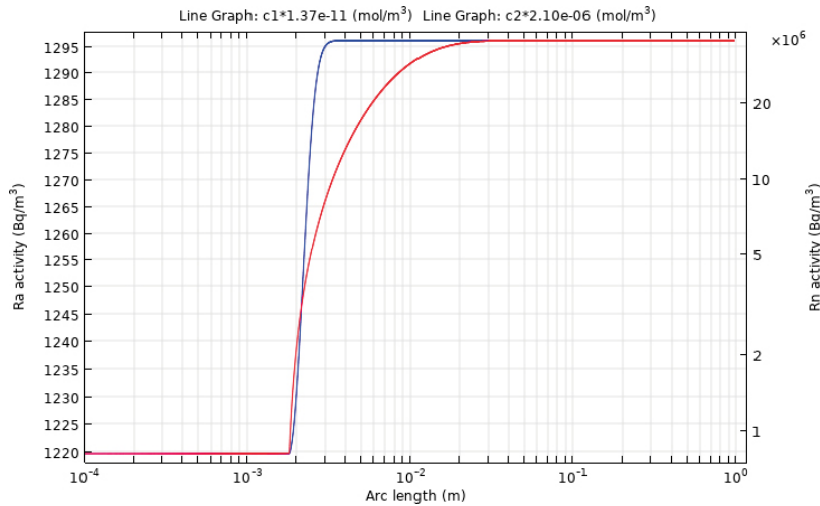
Figure 3-3. Activity profiles. Blue line for radium profile and red line for radon profile. Arc length means distance from the dummy in the hole, first through the water in the slot and then further into the rock matrix. See Figure 3-1.

### *Using Laplace transformation*

Radium

Figure 3-4 shows how the radon activity builds up over time in the circulating water in the slot. The results are directly proportional to the emanation factor η, which is not known and is somewhere between 1 and 100 %, in the simulations a value of the emanation factor of 1.0 is used. Although the emanation factor could be estimated it is very sensitivity to the local porosity of the of the mineral grains that contain the uranium (Liu and Neretnieks 1996, Neretnieks 2013). The results are quite sensitive to the value of the surface retardation factor. Figure 3-4 also shows the sensitivity to surface sorption retardation on the borehole walls.

The activity in the slot as well as the concentration profiles in the rock matrix are sensitive to the pore diffusion coefficient and matrix retardation coefficient. This is seen in Figure 3-5 where D_p and R_d have been varied by a factor of 10 down and up respectively.

Figure 3-6 shows a comparison of Ra activity in the circulating water from numerical Comsol solution and Laplace solution as well as steady state analytical solution for very long times. The difference between the results is less than 1 % at most.
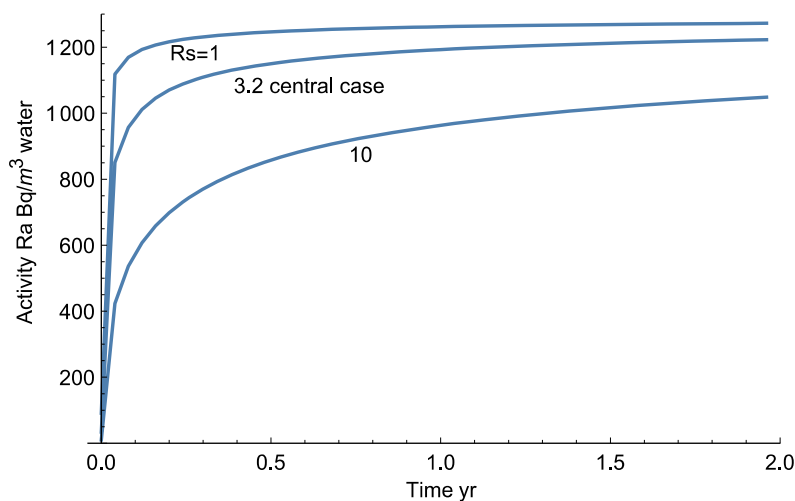
Figure 3-4. Sensitivity of radium activity in the circulating water to Rs for an emanation factor $\eta=1$. Linear diffusion case.
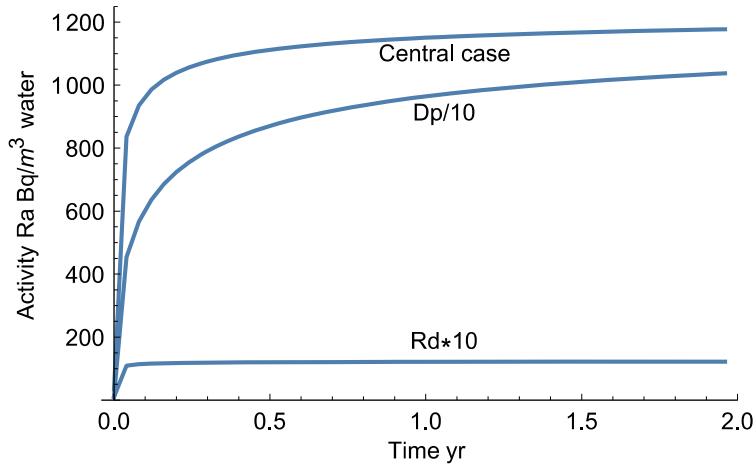
Figure 3-5. *Sensitivity of radium activity in the circulating water to Rd and Dp for an emanation factor η=1. Linear diffusion case.*
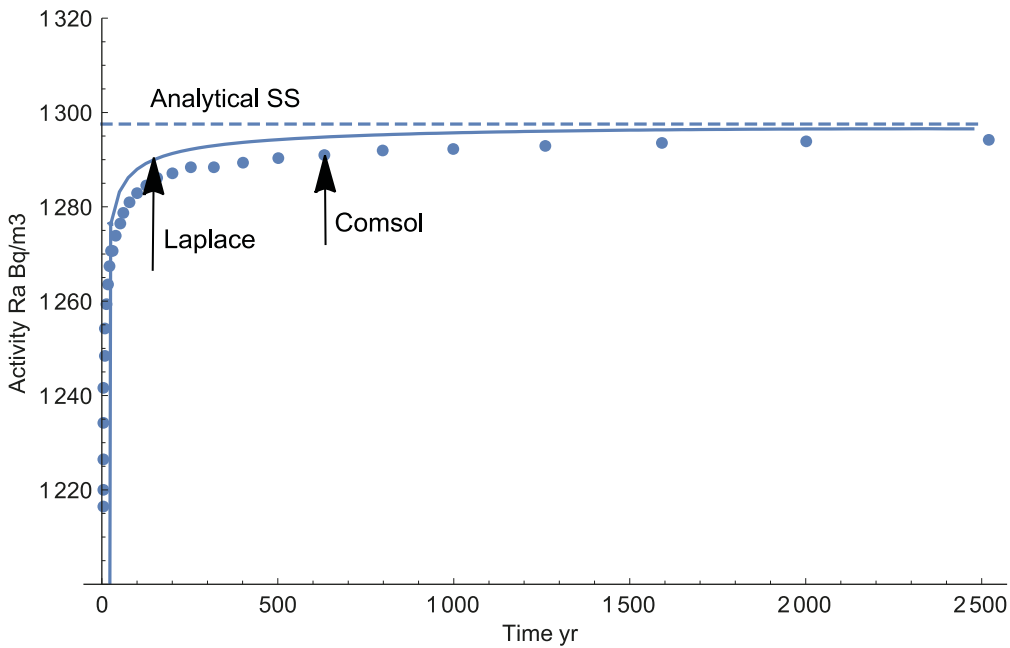
Figure 3-6. *Comparison of Ra activity in the circulating water from numerical Comsol solution and Laplace solution as well as steady state analytical solution. Linear diffusion.*

Radon

Figure 3-7 shows the sensitivity of the build-up of Rn activity in the circulating water to the pore diffusion coefficient.

Figure 3-8 shows a comparison of radon activity in the circulating water in the slot between Comsol for the radial diffusion case and Laplace results for the linear diffusion case. It also shows the difference between the "correct" radial diffusion case and that obtained for the linear diffusion approximation at steady state.
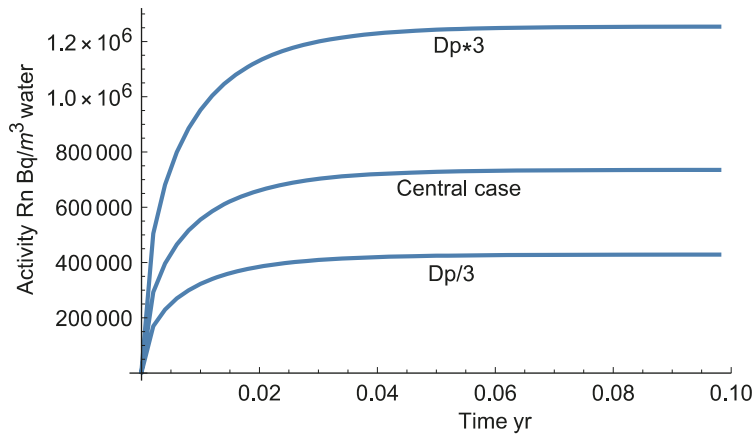
Figure 3-7. *Sensitivity of radon activity in the circulating water to Dp for an emanation factor η=1. Linear diffusion case.*

Figure 3-8. *Comparison of Rn concentration in the circulating water from numerical Comsol solutions and Laplace solution as well as steady state analytical solution.*

3.1.9   Discussion and conclusions

The two different methods to solve the equations give very small differences for the same diffusion geometry, confirming that both techniques solve the equations with sufficient accuracy.

The linear diffusion approximation underestimates steady state radon build-up in the slot by about 10 %. For radium the linear approximation overestimates the steady-state build-up by about 4 %. Radial symmetry should be used for the present problem.

The finite element method used in Comsol handles both linear and radial diffusion with the same ease. The use of radial symmetry in the Laplace formulation involves Bessel functions and the results were found to be sensitive to the choice of the distance to the outer boundary for diffusion beyond which pore water concentration is not affected.

Although the emanation factor could be estimated it is very sensitivity to the local porosity of the of the mineral grains that contain the uranium (Liu and Neretnieks 1996, Neretnieks 2013). It is expected to lie between 0.01 and 1. It is by far the largest uncertainty in the presented results.

The results can be compared to data from two Swedish sites, Laxemar and Forsmark. At both Laxemar and Forsmark, at repository depth, radium concentration in the groundwater vary between about 3 and 20 000 Bq/m^3. Radon activities vary between 10 000 Bq/m^3 and 3 MBq/m^3 (Neretnieks 2013). The activities in waters sampled from fractures in the field are likely to represent steady state conditions.

3.2 Modelling by Amphos 21

3.2.1 Introduction

Background

Task 9 of SKB Task Force GWFTS focuses on the realistic modelling of coupled matrix diffusion and sorption in heterogeneous crystalline rock matrix at depth. This is done in the context of inverse and predictive modelling of tracer concentrations of the in-situ experiments performed within LTDE-SD at the Äspö Hard Rock Laboratory in Sweden, as well as within the REPRO project at the ONKALO underground rock characterisation facility in Finland, focusing on sorption and diffusion. The ultimate aim is to develop models that in a more realistic way represent retardation in the natural rock matrix at depth (Andersson et al. 2020).

A natural process, which is also dependent on the diffusivity in rock, is the radon and radium production and transport in natural groundwater. Radon and radium are produced by radioactive decay mainly in the rock matrix and thereafter transported by diffusion out to the groundwater in the fractures. The concentration of these elements in the fracture porewater are therefore favoured by 1) high rock matrix diffusivity 2) long life-time (i.e., half-life) of the radionuclide and 3) high concentration of the parental radionuclides (i.e., the uranium or thorium concentrations). It is therefore obvious that diffusion characteristics applied in the model setup for the TDE diffusion experiment could also be used for the prediction of the radon and radium concentrations in the fracture groundwater.

The present experimental setup in the REPRO TDE experiment (boreholes with a dummy giving a thin and well determined annulus water volume) offers good possibilities of estimating radon and radium fluxes in a rock matrix environment. Showing the capability of predicting and understanding the process of the natural tracers radon and radium in relation to the TDE Experiment with added synthetic tracers will give further justification to the diffusion models applied. The model will, in such case, show its applicability both for through-diffusion processes as well as for the case of production of safety-relevant radionuclides inside the matrix, followed by an out-diffusion.

Objectives and scope

The main objective of this work is to use the models developed for Task 9C to simulate the out-diffusion of two naturally occurring radionuclides (^{226}Ra and ^{222}Rn) into the boreholes of the REPRO TDE experiment. For this objective, the Task 9C models have been slightly modified to incorporate both the decay reaction of ^{226}Ra and ^{222}Rn and a homogeneous sorption model based on k_d for ^{226}Ra.

The report is structured in the following way. In Section 3.2.2, a brief overview of the naturally occurring radionuclides is given. Section 3.2.3 focuses on the modifications carried out to set-up the Task 9C-Extension model. Section 3.2.5 shows the obtained results and Section 3.2.6 summarizes the main conclusions of the work.

3.2.2 Naturally occurring radionuclides

There are two main sources of natural radiation: cosmic radiation (i.e., gamma rays that constantly bombard the atmosphere) and the radiation arising from the decay of naturally occurring radionuclides. These naturally occurring radionuclides come from the primordial radioactive elements in the earth's crust. The primordial radionuclides have extremely long half-lives, comparable with the age of the earth, and they are in secular equilibrium with the other radionuclides of their decay chain. One of these primordial radionuclides is Uranium-238, and its decay chain will be studied in this work.

Figure 3-9 shows a sketch of the decay chain of ^{238}U. As shown, the decay-chain of ^{238}U is relatively long. Each alpha decay step releases a ^{4}He ion until the stable ^{206}Pb nuclide is formed. Due to the extremely long half-life of ^{238}U (4.47×10^9 years), it reaches secular equilibrium with its daughter radionuclides (it is proven numerically in the next sub-section), which means that the activities of the child radionuclides of the decay chain remain constant over time.

^{226}Ra and ^{222}Rn are part of the ^{238}U decay chain. This set of radionuclides are responsible of a major fraction of the internal dose received by humans from the naturally occurring radionuclides. ^{226}Ra decays emitting an alpha particle (i.e., a ^{4}He nucleus), with a half-life of 1 600 years into ^{222}Rn. The latter has a short half-life compared to its parent ($\tau_{Rn-222} = 3.82$ days) and after six more decay steps the stable ^{206}Pb nuclide is formed. Over these six decay steps, multiple short-lived alpha-particle and beta-particle emitting progeny are produced. Thus, even though ^{226}Ra itself adds little to the radioactive activity of the environment, its decay products do have a noticeable effect.
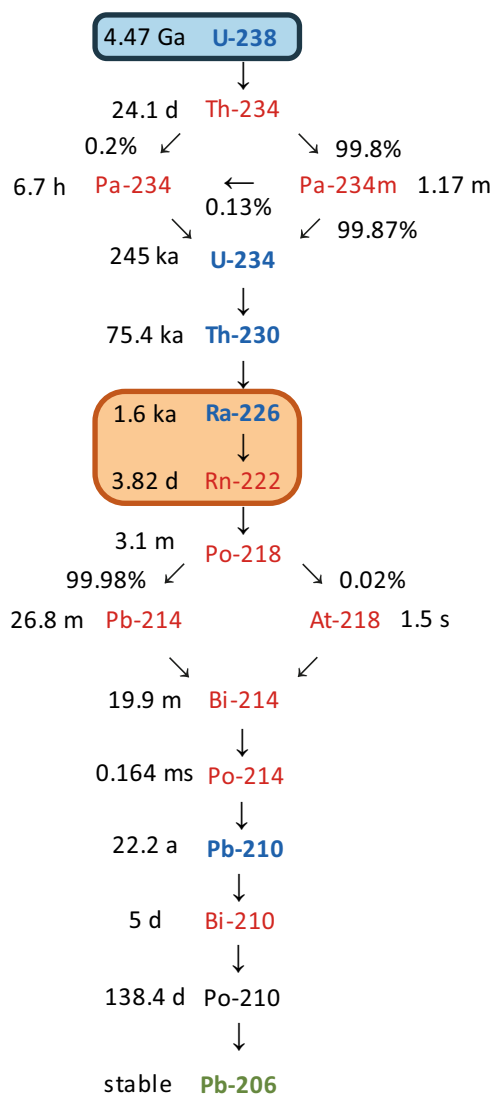
Figure 3-9. *Decay chain of the primordial radionuclide ^{238}U (with a half-life of $4.47 \cdot 10^9$ years). The numbers at the left side indicate the half-life of each child radionuclide. The ^{226}Ra / ^{222}Ra decay couple is pointed out with a brown square. The decay chain reaches the stable ^{206}Pb radionuclide at the end.*

3.2.3   Model set-up

In this work, the ^{226}Ra $\rightarrow$ ^{222}Rn decay couple will be studied. The objective is to use the best performing model developed for Task 9C to model the concentrations of these two radionuclides at both the injection and observation boreholes for the duration of the experiment.

It is assumed that, initially, there is a constant concentration of both radionuclides in the rock matrix. These concentrations will be estimated numerically based on the decay chain of ^{238}U and the age of the studied rock sample. The drilled boreholes have a zero concentration of both radionuclides and, in consequence, radionuclide transport will be assumed to be driven by molecular diffusion due to the concentration gradient between the boreholes and the rock matrix. Moreover, the Ra^{2+} ions are known to be strongly sorbing in the considered rock, and thus, a homogeneous isotherm sorption model based on distribution coefficients (k_d based sorption model) will also be implemented for the mentioned radionuclide. The model will then be simulated for 10 years, which is the temporal extension of the REPRO TDE experiment. Based on the obtained results, breakthrough curves (BTD) at the three boreholes of the experiment for the different radionuclides will be computed. These steps are summarized in Figure 3-10.

Parameterisation of the disintegration model

Decay chain of ^{238}U

The initial concentrations of ^{226}Ra and ^{222}Rn in the rock matrix have been computed using the ^{238}U decay chain (Figure 3-9). To solve the full ^{238}U decay chain (i.e., to get the time evolution of the child radionuclides) one needs to obtain the initial concentration of ^{238}U. This concentration can be found by using the measured concentration of ^{238}U, the disintegration rate of ^{238}U (λ_{U-238}) and the rock age. These parameters are summarized in Table 3-3.

Table 3-3. Parameters to compute the initial concentration of ^{238}U at the considered rock sample of the REPRO TDE experiment.

Parameter	Value
^{238}U measured [mol/m_T^3]	0.0852
Rock age [y] (Neretnieks et al. 2013)	1.85×10^9
Disintegration rate of ^{238}U [y^{-1}]	1.55×10^{-10}
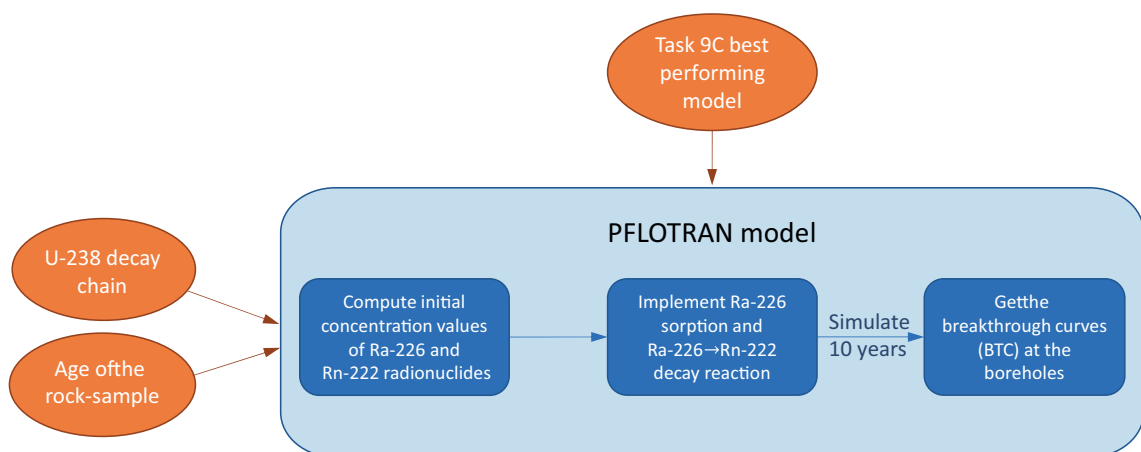
Figure 3-10. *Sketch summarizing the main conceptual steps to build the Task 9C-extension model. External information on which the model is built upon is shown in orange. The main tasks carried out with the model are shown in dark blue.*

The initial concentration of ^{238}U in the rock matrix can be computed using Equation (3-19).

$$C^{U238}(0) = C^{U238}(t_{rock})e^{\lambda_{U238}t_{rock}}$$
3-19

Where $C^{U238}(t_{rock})$ is the current measured concentration of ^{238}U, λ_{U238} is the disintegration rate of ^{238}U, t_{rock} is the age of the rock and $C^{U238}(0)$ is the initial concentration of ^{238}U when the rock was formed. Using the parameters of Table 3-3 an initial concentration of $C^{U238}(0) = 0.113\ mol/m^3_{rock}$ is obtained for ^{238}U.

Once the initial concentration of the primordial radionuclide ^{238}U is known, a system of Ordinary Differential Equations (ODE) can be solved to get the numerical evolution of each child radionuclides. The generic form of this system of ODEs is shown in Equation (3-20). This equation describes the time evolution of the activities of a radionuclide chain having one parent and n radionuclide children.

ODE system for a radionuclide chain:
$$\begin{cases} \dfrac{dA_p(t)}{dt} = -\lambda_p A_p(t) \\ \dfrac{dA_1(t)}{dt} = -\lambda_1 A_1(t) + \lambda_p A_p(t) \\ \vdots \\ \dfrac{dA_n(t)}{dt} = -\lambda_n A_n(t) + \lambda_{n-1}A_{n-1}(t) \end{cases}$$
(3-20)

Here, A_p denotes the activity of the parent radionuclide and A_i with $i \in [1, n]$ represents the activities of each child radionuclide. The same notation is used to represent the decay rate (λ) of each radionuclide (i.e., λ_p for the parent decay rate and λ_i for the children decay rates).

Equation (3-20) has been applied to the ^{238}U decay chain. For this case, the parent radionuclide is ^{238}U and the radionuclides described in Table 3-4 have been used to represent the whole decay chain. Notice that there is a direct link between the decay rates and the half-lives of the radionuclides displayed in Figure 3-9, which is shown in Equation (3-21).

$$t_{1/2} = \frac{\ln 2}{\lambda}$$
(3-21)

Where λ is the decay rate and $t_{1/2}$ represents the half-life of the radionuclide.

Table 3-4. Parameters used to model the decay chain of ^{238}U.

Radionuclides	Half-life (y)	Decay rate (y^{-1})	Type [-]
^{238}U	4.47×10^9	1.55×10^{-10}	Parent
^{234}U	2.45×10^5	2.83×10^{-6}	Child
^{230}Th	7.70×10^4	9.00×10^{-6}	Child
^{226}Ra	1.60×10^3	4.33×10^{-4}	Child
^{222}Rn	1.04×10^{-2}	6.66×10^1	Child

Estimation of the ^{226}Ra and ^{222}Rn concentrations

In order to estimate the concentrations of ^{226}Ra and ^{222}Rn in the bulk rock matrix a Python script has been developed. This script solves the generic decay chain equation shown in Equation (3-20) in a user-friendly way. The script needs to know the details of the decay chain, as the different radionuclides that are part of it, their decay rates and the role they play on the decay chain (i.e., whether they are a *parent* or a *child* radionuclide). The script automatically implements and solves Equation (3-20) and plots the evolution of the radionuclide concentrations. The results that have been obtained for the ^{238}U chain are shown in Figure 3-11. As expected, all the child radionuclides reach a secular equilibrium state after approximately 10^5 years. This could be directly observed due to the extremely high half-life of ^{238}U compared to its child radionuclides. However, this way, a numerically robust and accurate model has been developed that can be applied to other non-trivial scenarios. The resulting equilibrium concentrations of the members of the ^{238}U decay chain nowadays (i.e., after 1.85×10^9 years after the rock formation) are shown in Table 3-5.
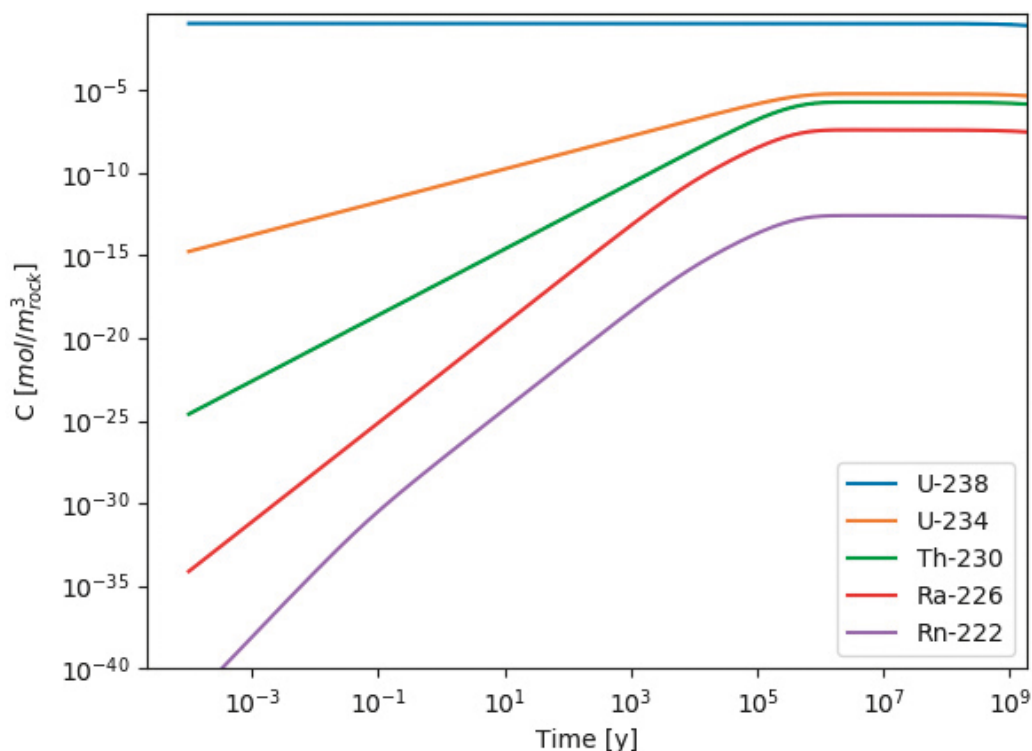
Figure 3-11. *Plot showing the concentrations over time of the considered radionuclides of the ^{238}U decay chain. Notice that due to the very long half-life, the concentration of ^{238}U barely changes. In consequence, all the other radionuclides reach a secular equilibrium state among each other after ~ 10^5 years.*

Table 3-5. Estimated total bulk concentrations of ^{226}Ra and ^{222}Rn at present time (1.85 × 10^9 years after rock formation).
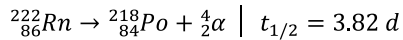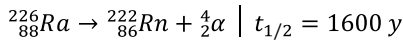
Radionuclides	Estimated bulk concentration [mol/m^3_{rock}]
^{226}Ra	3.05×10^{-8}
^{222}Rn	1.98×10^{-13}

However, since the ^{226}Ra is a strongly sorbing radionuclide, the value computed in Table 3-5 cannot be used directly in PFLOTRAN, since it represents the total concentration of ^{226}Ra, not the aqueous part. Based on the k_d-based linear sorption model that has been implemented, this total concentration can be easily distributed into the aqueous and sorbed parts. A distribution coefficient of 0.02 m^3/kg (Carbol and Engkvist 1997) has been used for ^{226}Ra and the computed final aqueous concentrations are shown in Table 3-6.

Table 3-6. Estimated aqueous concentrations of ^{226}Ra (aqueous part) and ^{222}Rn at present time (1.85 × 10^9 years after rock formation). A porosity of 0.006 has been considered to obtain the aqueous concentrations.

Radionuclides	Estimated aqueous concentration [mol/L]
^{226}Ra	5.60×10^{-13}
^{222}Rn	3.30×10^{-14}

Summarizing, two decay reactions have been considered in this work:

$$^{226}_{88}Ra \rightarrow {}^{222}_{86}Rn + {}^{4}_{2}\alpha \mid t_{1/2} = 1600\ y$$

$$^{222}_{86}Rn \rightarrow {}^{218}_{84}Po + {}^{4}_{2}\alpha \mid t_{1/2} = 3.82\ d$$

The initial aqueous concentrations of ^{226}Ra and ^{222}Rn have been computed based on the ^{238}U decay chain and taking into account the linear sorption distribution for ^{226}Ra.

Description of the best-performing Task 9C model

Geometry and mesh

The geometry and mesh of the Task 9C-extension model is equal to the model developed for Task 9C. This model features a Borehole Deformation Zone (BDZ) surrounding each of the boreholes. These perturbated zones are often generated when the boreholes of the experimental set-up are drilled and can significantly alter the material properties at the first few millimetres surrounding the borehole. Details of the geometry of the Task 9C-extension model are sketched in Figure 3-12. As shown there, the geometry of the model is divided in three main regions: the boreholes (in blue) represent the void space of the drillholes in which water is in circulation and they are used to compute the breakthrough curves of the considered radionuclides after the simulation is done. The rock matrix (in orange) represents the intact core of the rock, and it is conceptualized by two parameters (i.e. porosity and tortuosity) that can be tuned to fit the experimental data. Finally, the BDZ is represented by the yellow ring that surrounds each of the boreholes. This is the zone that have been altered due to the drilling of the cores and it is parameterized by a certain width and a given porosity and tortuosity values. The width of the BDZ has been chosen to be 21.75 mm while the rest of the dimensions have been kept equal to the blind prediction stage model. The material properties will be discussed next, however, as shown in Figure 3-12, constant and homogeneous properties have been applied to each region of the model. It is worthwhile mentioning that anisotropic diffusion has not been considered in this model. Thus, isotropic diffusion will be the driving force for radionuclide transport.
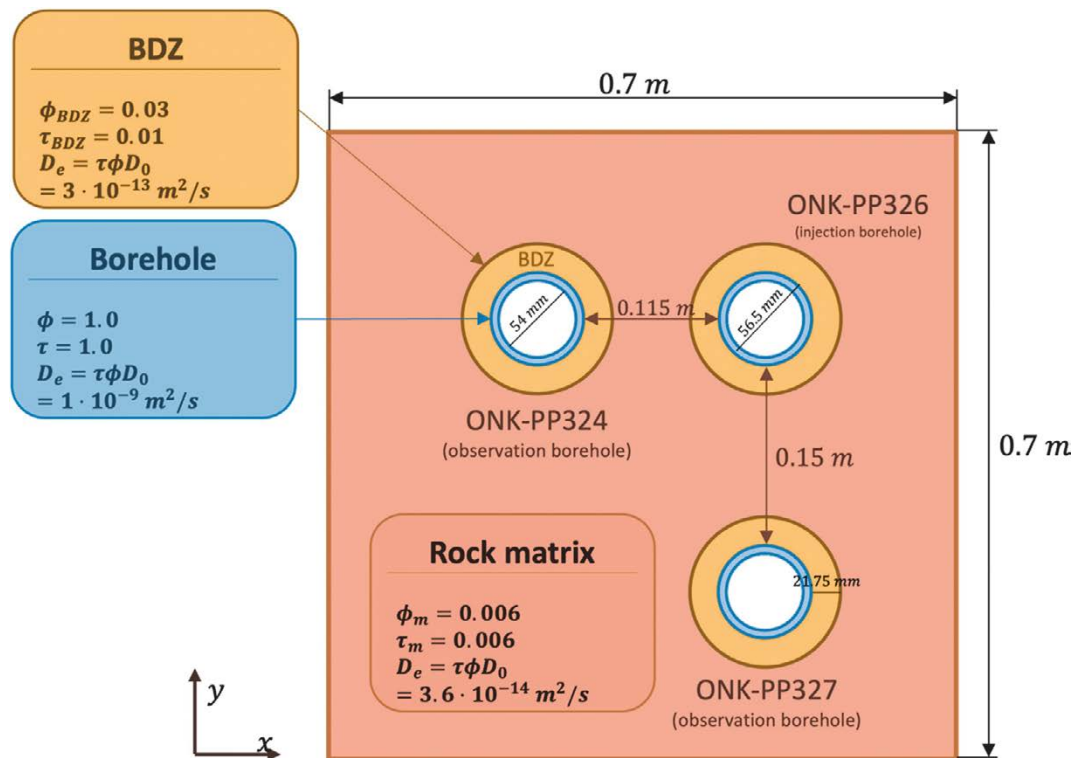
Figure 3-12. *Model set-up of the back-analysis stage model. The key material properties of the considered three zones (i.e. the rock matrix, the boreholes and the Borehole Deformation Zone (BDZ)) are shown. Symbols are consistent with the notation used in Table 3-7.*

The mesh of the model is a semi-structured prismatic mesh, and it contains $527\,000$ elements (Figure 3-13).

Different mesh sizes have been assigned to the geometrical regions defined in Figure 3-12. The annular region that represents the borehole (the blue region in Figure 3-12) is the most refined region and has an average mesh size of 5×10^{-4} m. The BDZ region (the yellow region in Figure 3-12) has a mean mesh size of 7.5×10^{-4} m, and in the rock matrix (the orange region in Figure 3-12), the mesh size has been regularly increased to a mean value of 1.5×10^{-3} m. This fine refinement close to the interfaces between the boreholes and the BDZ allows to effectively capture the diffusion patterns of the different tracers, specially the out-diffusion from the injection borehole of the sorbing radionuclides.

Initial and boundary conditions

The initial and boundary conditions of the Task 9C-extension model are summarised in Figure 3-14. As shown, the rock matrix is initially filled with a water containing the ^{226}Ra and ^{222}Rn concentrations computed previously. At the three borehole regions (i.e., both the injection and observation boreholes) a water with zero-concentration of ^{226}Ra and ^{222}Rn is applied initially. A zero-gradient boundary condition is set at the outer boundaries of the model. These initial and boundary conditions coupled with the ^{226}Ra and ^{222}Rn decay reactions and the linear sorption of ^{226}Ra are expected to model the out-diffusion of the mentioned radionuclides from the rock matrix into the drilled boreholes.
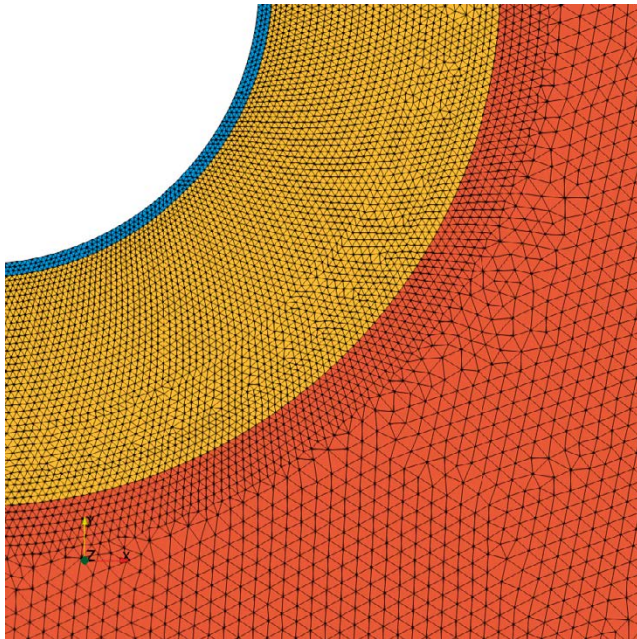
Figure 3-13. *Top view of the back-analysis stage model mesh. Notice the dynamic refinement among the different regions: the mesh is highly refined at the borehole region (in blue), it gradually gets coarser as the region changes to the BDZ (in yellow) and it reaches it maximum size at the rock matrix (in orange).*
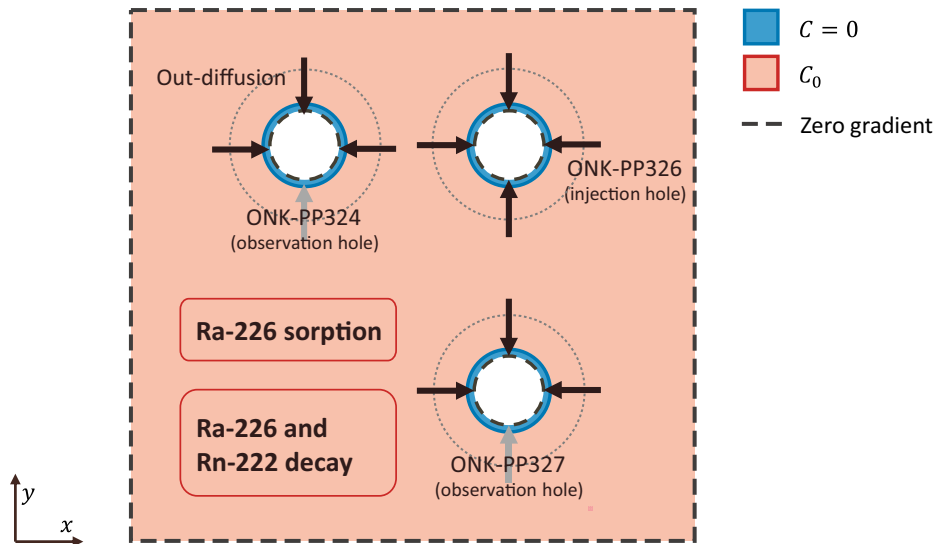
Figure 3-14. *Initial and boundary conditions of the Task 9C-extension model. The ^{226}Ra and ^{222}Rn concentrations are set to zero inside the three boreholes. At the rock matrix, the initial concentration computed in section 0 is set. At the outer boundaries of the domain, a zero-gradient boundary condition is applied.*

Transport and material parameterization

The material and transport properties of the model are summarised in Figure 3-12 and in Table 3-7. These values come from the best performing out-analysis model that was developed for Task 9C. As shown, the rock matrix is the region with the lowest porosity and effective diffusivity. The BDZ region represents the region altered by the drilling of the boreholes and thus, a higher porosity and effective diffusivities have been assigned, compared to the rock matrix. The borehole region has a porosity and tortuosity of 1.0 which represents free diffusion in water ($D_{eff} = 1 \times 10^9\,\text{m}^2/\text{s}$).

Table 3-7. Material and transport parameters used at the Task 9C-extension model.

	Parameter	Back-analysis stage model	Units
Diffusion related parameters	Matrix porosity ϕ_m	0.006	–
	Matrix tortuosity τ_m	0.006	–
	Matrix effective diffusivity $D_{eff} = \phi_m \tau_m$	3.6×10^{-14}	m²/s
	BDZ porosity ϕ_m	0.03	m²/s
	BDZ tortuosity τ_m	0.01	–
	BDZ effective diffusivity $D_{eff} = \phi_m \tau_m$	3.0×10^{-13}	m²/s
Sorption related parameters	k_d^{Ra-226}	0.02	m³/kg

3.2.4   Using ^{4}He to estimate the rock age

Besides modelling the out-diffusion of ^{226}Ra and ^{222}Rn as proposed in the Task Description (see Appendix A), an extra modelling activity has been carried out. In this activity, the out-diffusion of ^{4}He has been studied and modelled. This additional calculation is deemed to be illustrative of the potential use of ^{4}He data in future studies, since ^{4}He is a good marker for the underlying flow and transport processes (e.g., Trinchero et al. 2019).

^{4}He is produced by the alpha decay of natural uranium and thorium-bearing minerals within the aquifer solids and, since it is a stable nuclide, it gets accumulated into the intact rock matrix over time. Thus, in theory, one could use the measured BTC of ^{4}He in the boreholes to infer data of the underlying diffusion processes. In this work, an illustrative example of out-diffusion of ^{4}He has been developed, with the objective to model the BTC that would be observed at the boreholes.

Estimation of the initial concentration of ⁴He

The same workflow used to model the out-diffusion of ^{226}Ra and ^{222}Rn has been applied for ^{4}He. Thus, first, the initial concentration of aqueous ^{4}He at the rock matrix has been estimated. This calculation is slightly more complex than for the ^{226}Ra and ^{222}Rn case, mainly because ^{4}He is not in secular equilibrium with its parent radionuclides. In fact, the production rate of ^{4}He is linked to all the alpha decays that happen in the ^{238}U and ^{232}Th decay chains. As shown in Figure 3-15, the disintegration chains of ^{238}U and ^{232}Th are governed by alpha decay, and thus, a ^{4}He ion (i.e., an alpha particle) is generated on each step. The hypothesis of this work is that these alpha particles are accumulated over time at the rock matrix. Thus, the production rate of ^{4}He can be approximated by summing up the decay rates of each of the children of the decay chain. This can be done because the decay rates of the child radionuclides are much quicker than the parent's decay rates, so the ^{4}He production will be controlled by the parent's decay rates. In other words, we assume secular equilibrium between the parent radionuclides (^{238}U and ^{232}Th) and the child radionuclides. The ODE describing the generation of ^{4}He can be represented as shown in Equation (3-22).

$$\frac{dC^{He-4}}{dt} = 8\lambda_{U-238}\frac{dC^{U-238}}{dt} + 6\lambda_{Th-232}\frac{dC^{Th-232}}{dt} \tag{3-22}$$

Assuming that at the formation of the rock ($t_{rock} = 1.85 \times 10^9$ years (Neretnieks et al. 2013) there was zero concentration of ^{4}He, Equation (3-22) has been solved using the Python script that was developed for the previous task. Figure 3-16 shows the plot showing the generation of ^{4}He over time. The ODE has been integrated for $t_{rock} = 1.85 \times 10^9$ years and an estimated concentration of $0.252 \frac{mol}{m_{rock}^3}$ of ^{4}He has been computed. This value can be converted to aqueous concentration by means of Equation (3-23), which results in a value of $C_{aq}^{He-4}\left[\frac{mol}{L}\right] = 0.04M$. This value has been used as an estimation of the initial concentration of ^{4}He at the rock matrix.

$$C_{aq}^{He-4}\left[\frac{mol}{L}\right] = \frac{C_{bulk}^{He-4}\left[\frac{mol}{m_{rock}^3}\right]}{1\,000 \cdot \phi_m} \tag{3-23}$$

Where ϕ_m is the porosity of the rock matrix, C_{aq}^{He-4} is the aqueous concentration and C_{bulk}^{He-4} is the bulk concentration.
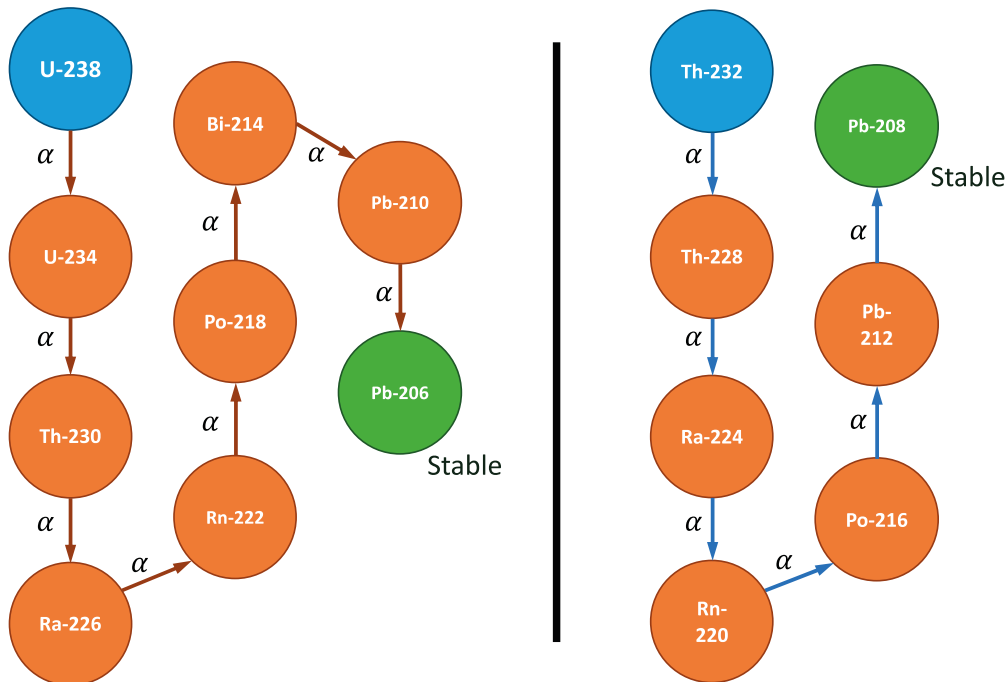
Figure 3 15. *Schematic view of the decay chain of 238U and 232Th. The main disintegration channel of both radionuclides is alpha decay. Thus, a 4He nucleus is generated on each of the disintegration steps before reaching the stable nuclide.*
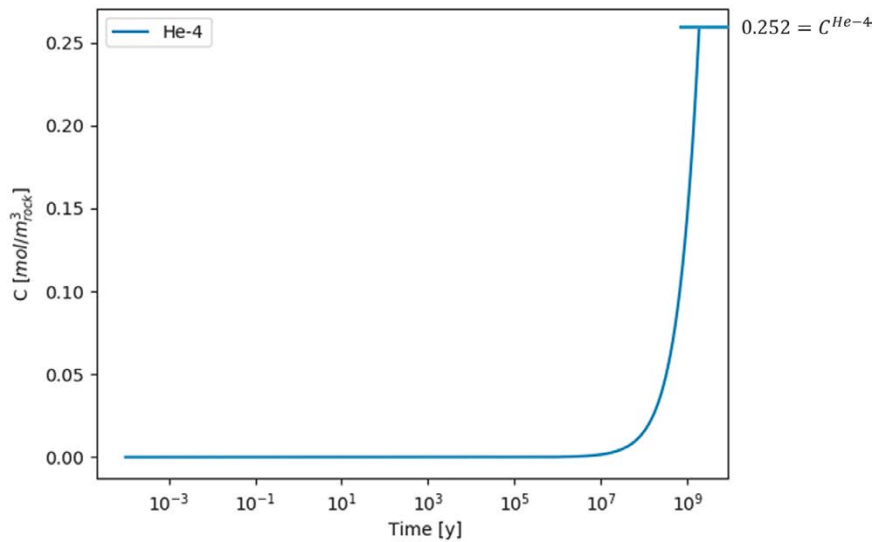
***Figure 3-16.** Plot of the ⁴He concentration over time computed solving the ⁴He production ODE shown in Equation (3-4). A zero-concentration of ⁴He is assumed initially and the alpha decay contributions of all the elements of the ²³⁸U and ²³²Th decay chains are considered.*

3.2.5 Results

The model set-up in Section 3.2.3 has been simulated using PFLOTRAN, which is an open source, state-of-the-art, massively parallel, flow and reactive transport solver. A total time frame of 10 years has been simulated using a 128 cores AMD computing cluster. The numerical simulation run smoothly, and it took around 1 h to finish. The results are presented by means of a set of snapshots taken at different times and breakthrough curves (BTCs) measured at the three boreholes.

Evolution of ²²⁶Ra and ²²²Rn at the different boreholes

²²⁶Ra

Figure 3-17 displays the BTCs computed at the boreholes for ²²⁶Ra. From the BTCs it can be clearly seen that the ²²⁶Ra concentration at the three boreholes equilibrates very quickly (< 0.5 y) with the concentration at the rock matrix. This behaviour is equal regardless of the considered borehole.
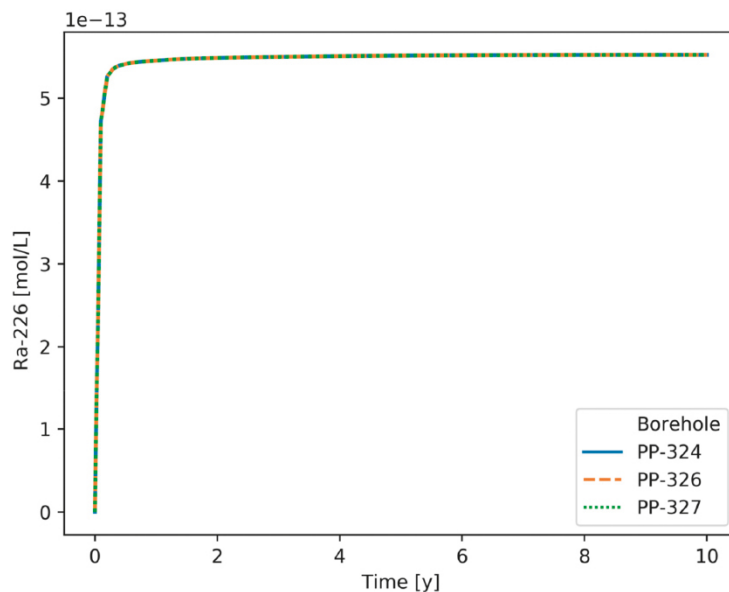
***Figure 3-17.** Plot of the BTCs of ²²⁶Ra measured at the annular region of the three considered boreholes. The BTCs obtained for the three boreholes overlap completely.*

²²²Rn

Figure 3-18 shows 4 snapshots of the model at different times and Figure 3-19 displays the BTCs computed at the boreholes for ²²²Rn. The qualitative behaviour of ²²²Rn is similar to the ²²⁶Ra if one takes a look to the BTCs. The initial very low value increases quickly (< 0.1 years) to reach a plateau at $3.5 \times 10^{-16} M$. However, this value is two orders of magnitude lower than the initial value at the rock matrix. This difference comes from the fact that ²²²Rn has a very small half-life compared to ²²⁶Ra ($t_{1/2}^{Rn-222} = 3.8$ days vs $t_{1/2}^{Ra-226} = 1\,600$ years). Due to this small half-life, the diffusive flux of ²²²Rn is not able to counter the decay rate of itself, and an equilibrium between these two processes is reached. Notice that in the BDZ region, where diffusion is smaller than in the borehole region but higher than in the rock matrix, a higher plateau is reached with an approximate concentration value of $1 \times 10^{-14} M$.
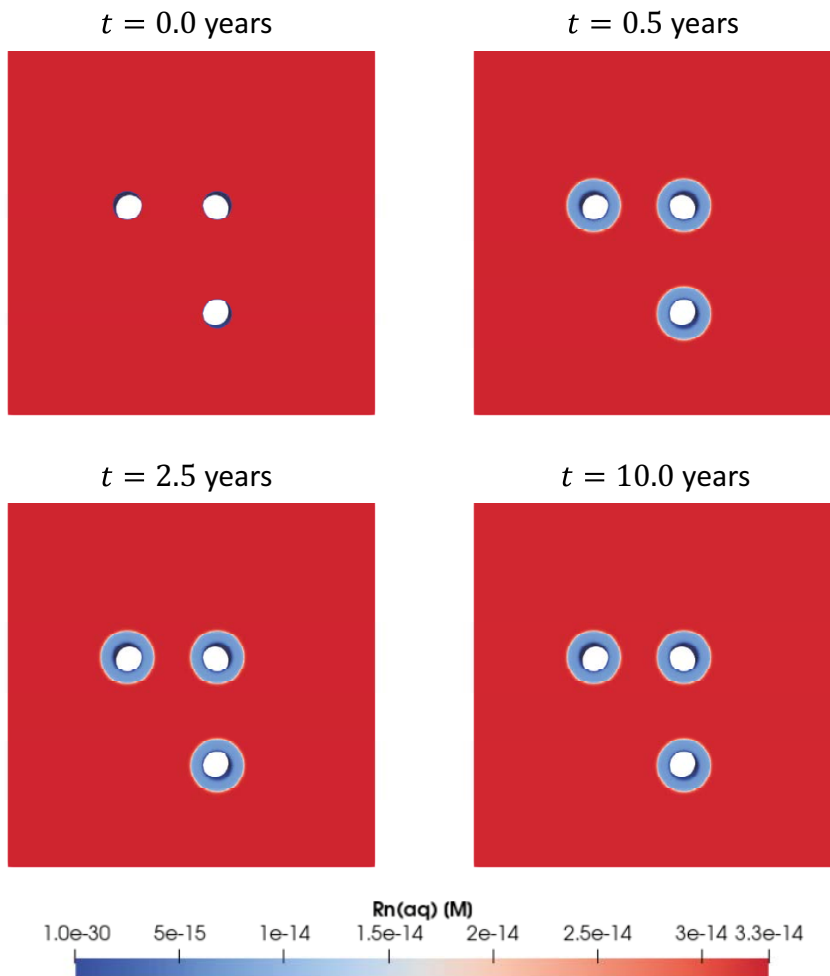
Figure 3-18. *Plot of four timestamps of the out-diffusion model displaying the aqueous concentration of ²²⁴Rn. Even though it is not easy to appreciate, the borehole concentration equilibrates with the concentration of the rock matrix very quickly.*
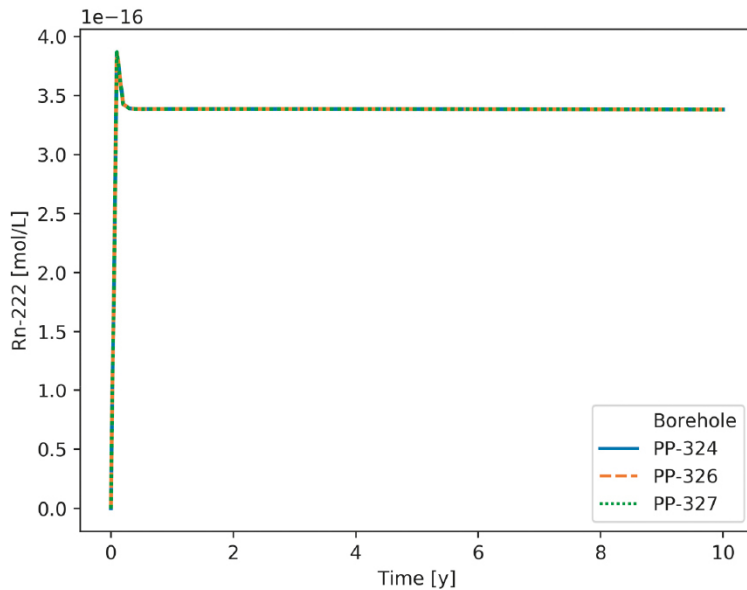
Figure 3-19. *Plot of the BTCs of ^{222}Rn measured at the annular region of the three considered boreholes. The BTCs obtained for the three boreholes overlap completely.*

Evolution of ^{4}He at the different boreholes

Figure 3-20 shows 4 snapshots of the model at different times and Figure 3-21 displays the BTCs computed at the boreholes for ^{4}He. The snapshots show a qualitatively different behaviour for ^{4}He compared to ^{226}Ra and ^{222}Rn. In this case, a typical diffusion pattern can be observed which is governed by the diffusivities found in each region. Thus, it can be clearly seen the effect of the BDZ, which has a higher diffusion coefficient than the rock matrix. The presence of the BDZ is possibly affecting the behaviour of the BTCs too, delaying them to reach to a plateau due to the lower concentration gradients between the borehole and its surroundings. On this respect, if one looks to the computed BTCs, the considered 10 years of simulation time are not enough to reach a plateau as opposed to the ^{226}Ra and ^{222}Rn cases.

Due to the parameterisation of the considered rock, one would have to wait more than 10 years in order for the ^{4}He to reach a plateau concentration. However, in a more practical case, one could measure the concentration of ^{4}He at the borehole for a given time, and then fit this model's parameters to reproduce the measured breakthrough curve.

3.2.6 Conclusions and remarks

The main objective of Task 9C-extension was to set-up a model to do a blind prediction of the breakthrough curves of ^{226}Ra and ^{222}Rn at the three boreholes of the REPRO TDE experiment. On this regard, and as suggested in the task description, the model presented here is based on the best-performing back-analysis model that was developed for Task 9C earlier this year.

Even though the child radionuclides of the ^{238}U decay chain are in secular equilibrium with its parent, a general purpose decay chain solver has been implemented in Python to compute the initial concentrations of the considered radionuclides as well as to numerically verify that, indeed, ^{226}Ra and ^{222}Rn are in secular equilibrium with ^{238}U.

Regarding the model results, two different models have been simulated: the one modelling the out-diffusion of the ^{226}Ra and ^{222}Rn radionuclide couple, and the one that solves the out-diffusion of ^{4}He into the boreholes.
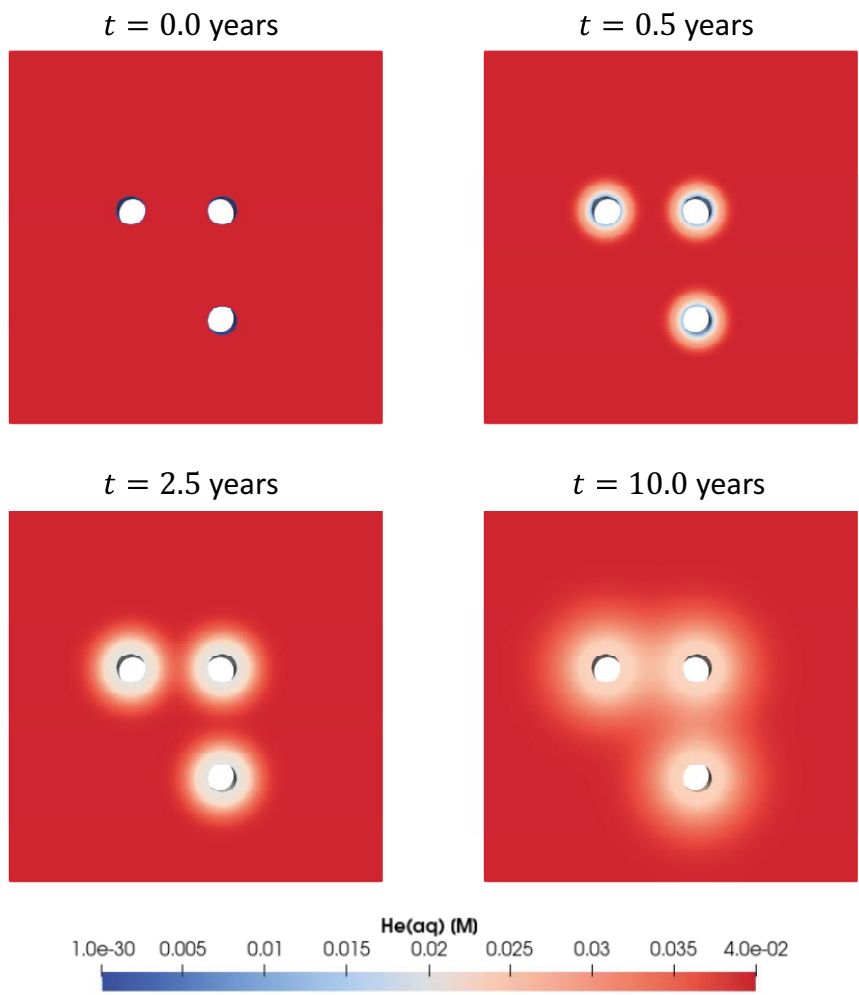
Figure 3-20. *Plot of four timestamps of the out-diffusion model displaying the aqueous concentration of ^{4}He.*
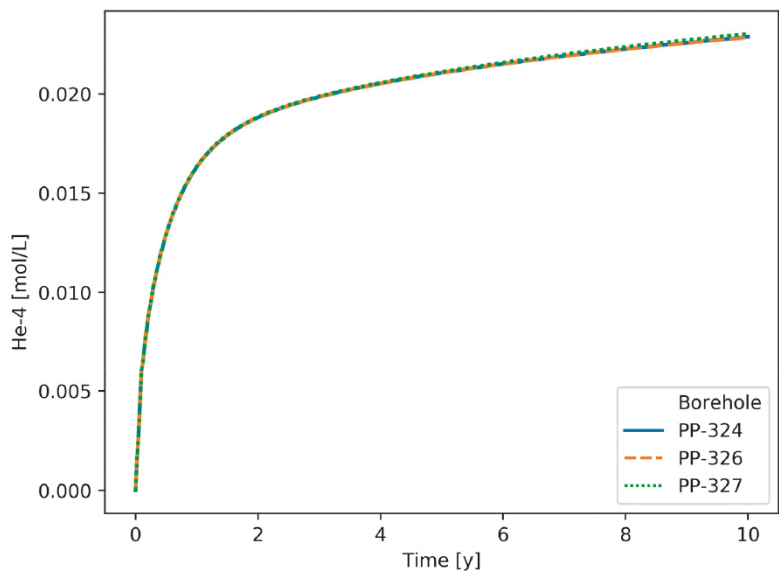
Figure 3-21. *Plot of the BTCs of ^{4}He measured at the annular region of the three considered boreholes. The BTCs obtained for the three boreholes overlap completely.*

A clear conclusion of both cases is that, due to the homogeneous and isotropic nature of the implemented material properties, the behaviour of the three boreholes (i.e., ONK-PP324, ONK-PP326, ONK-PP327) is indistinguishable. Locally, this conclusion is straightforward, since all the boreholes are identical. However, it also shows that the separation distance is high enough to avoid any interaction between the boreholes.

Regarding the evolution of ^{226}Ra, the computed BTCs show that it would quickly diffuse from the rock matrix into the boreholes reaching a plateau value at the same aqueous concentration as in the rock matrix.

The ^{222}Rn shows a slightly different behaviour. Since the half-life of ^{222}Rn is significantly smaller than the half-life of ^{226}Ra, the decay rate and the diffusion process interact with each other, making the ^{222}Rn reach a smaller plateau value than the initial matrix concentration. This effect is also seen inside the BDZ, which shows an intermediate plateau value due to the smaller diffusivity compared to the borehole region.

Finally, the out-diffusion of ^{4}He has also been simulated. The results show that the timeframe of the simulation (10 years) is not enough to allow the ^{4}He to reach a plateau at the boreholes, and thus, the initial concentration of ^{4}He at the rock matrix could not be estimated by just measuring the values at the boreholes. However, the measured BTCs of ^{4}He could be used to fit the out-diffusion model to the measured data and infer the initial concentration at the rock matrix.

4 Migration of Rn and Ra, experimental concentration measurement of the tracers in the aqueous phase

Laboratory measurements by University of Helsinki, Radiochemistry.

4.1 Rn/Ra analyses

Radon-222 is a noble, odourless colourless radioactive gas with a half-life of 3.82146 ± 0.00020 days. In the uranium-238 radioactive decay chain, radon-222 is produced by the alpha-decay of the radioactive alkaline earth metal radium-226, which has a half-life of $1\,600 \pm 7$ years (Girault et al. 2018). The $^{226}Ra/^{222}Rn$ couple can be a useful tool for the characterization of water and the identification of water source rocks, shedding light on the various water–rock interaction processes taking place in the environment. Dissolved radium activity concentration in liquid samples (Jia and Jia 2012) is generally measured using liquid scintillation spectrometry like it is done in this work. The two other routinely used analytical techniques for Ra isotope determination in biological and environmental samples are low-background γ-spectrometry and alpha spectrometry. According to Jia and Jia (2012), the Minimum Detectable Activity (MDA) of α-spectrometry technique (needs chemical separation) is 0.1mBq/l which is about two orders of magnitude lower than that of low-background HPGe γ-spectrometry from the 186keV energy peak and low-background device and LSC techniques. The maximum sensitivity could be best with the α-spectrometry technique.

^{222}Rn is a pure alpha emitter with no gamma radiation which makes its measurements somewhat tedious. Anyhow, since the short-lived daughters of ^{222}Rn have half-lives of a maximum of 27.06 min, the decay chain from ^{222}Rn to ^{214}Po is in secular equilibrium within a few hours. If the radon gas is well contained, and the activity is to be measured high enough, its activity can be easily determined from its gamma-emitting daughters ^{214}Pb and ^{214}Bi. Therefore, the mixing of the ^{222}Rn activity in the experimental section, as well as the activity concentration after mixing was observed by measuring the 609 keV gamma line of ^{214}Bi with an HPGe gamma detector (Ortec, USA) placed in contact with the tubing of the experimental section. A similar measurement method was used for the sample sent for measurements in a laboratory: the 10 ml sample was moved from the sampling loop to a 22 ml liquid low-diffusion scintillation vial filled with Milli-Q water to avoid empty gas volume where radon could gather. The vial was then measured with an HPGe gamma detector (Canberra, USA) using ^{214}Bi 609 keV gamma line.

4.2 Water samplings

Radon and radium measurements were done on five fracture water samples from ONKALO and water samples from the TDE experiment. The different waters analysed in the study have been collected from five water-conducting fractures ONK-KR15 75.0–75.2 m, OL-KR13 405.5–414.5 m, OL-KR11 411–430 m, OL-KR45 606–610 m and OL-KR44 766–780 m and packed-off sections of drill holes ONK-PP324 and ONK-PP327. The fracture waters represent the Olkiluoto groundwater at various depths with different salinities. In addition, the radon and radium concentrations in groundwaters at Olkiluoto area were measured in the late 90s, and the results are listed here for comparison (Voutilainen 1998, Saarinen and Suksi 1992). The elemental compositions of the groundwaters from the five fracture waters and the waters from the 90s are presented and the content of radium is presented as a function of the main elements in these waters.

In the sampling for the LSC technique, 5 ml of groundwater was collected directly to a weighed 22 ml liquid scintillation vial ready filled with 17 ml of liquid Ultima Gold AB scintillation cocktail (PerkinElmer, USA). The vial was closed tightly and shaken to mix the water and the scintillation cocktail. Low-diffusion PTFE coated vials with aluminium foil-lined sealing caps were utilized to avoid the leak of radon gas from the vial. The sampling technique is used for measuring ^{238}U-series radionuclides concentrations in groundwaters (Salonen 1993, Vesterbacka 2005).

For gamma counting, the water samples were taken from the ONK PP324 and ONK PP 327 after the experiment was closed (March 2020). The observation bore hole tubing were emptied and 200 ml samples were evaporated and dissolved into a 10 ml volume of dilute hydrochloric acid (0.1 M HCl). These samples were measured with high-resolution gamma device.

4.3 Rn/Ra measurements by liquid scintillation counting

The samples were delivered from sampling site to laboratory as fast as possible to minimize the ^{222}Rn decay. In general, the prepared source was measured twice in a low-background scintillation spectrometer (Quantulus, PerkinElmer) using its alpha-beta separation feature based on pulse shape analysis (PSA). The first measurement was done just after the sample preparation (immediate measurement) and the second one, after about a month when the radon and shorter-lived daughter nuclides are in secular equilibrium with ^{226}Ra (delayed measurement).

After weighing the vials, the immediate measurement of 120 minutes was started. Due to practical limitations and transport distance, the time from sampling to start of first measurement was about 24 hours after the sampling. In this measurement it was assumed that most of the signals in resulting spectrum come from ^{222}Rn and its short-lived daughters and the amount of ^{226}Ra compared to ^{222}Rn was insignificant. The resolution of the liquid scintillation counting is low and it is not possible to separate different alpha energies from each other. Therefore, the activity concentration of radon was calculated from the energy window which covers the alpha peak of radon and its two short-lived daughters (^{222}Rn – ^{218}Po – ^{214}Po). The alpha counting efficiency in the selected alpha window was 266 % ± 3 % and the detection limit was 0.3 Bq/l for a 120 minutes counting time. ^{226}Ra was determined from the delayed measurement. In this measurement, the energy window of the measurement covered the peaks of ^{226}Ra, ^{222}Rn, ^{218}Po and ^{214}Po, and the measurement efficiency was 366 ± 5 %. The detection limit for the delayed measurement for ONK-PP324 was 0.35 Bq/l and for ONK327 0.5 Bq/l in 240 minutes counting. The water sample from ONK PP324 was measured also for 24 hours when the detection limit was 0.03 Bq/l.

The calibration of the spectrometer was performed using a ^{226}Ra standard solution (Eckert & Ziegler, Germany) mixed with Ultima Gold AB and equilibrated for three weeks to get the decay chain in secular equilibrium. Since the alpha-beta separation function of the spectrometer was utilized, the calibration was started by optimizing the alpha-beta separation parameter (PSA for Quantulus™ 1220 Wallac spectrometer) for the utilized scintillation cocktail and sample concentration. After that, the measurement efficiencies for ^{222}Rn and ^{226}Ra were determined. In Figure 4-1, the alpha – beta separation technique that was used in the measurement is presented.
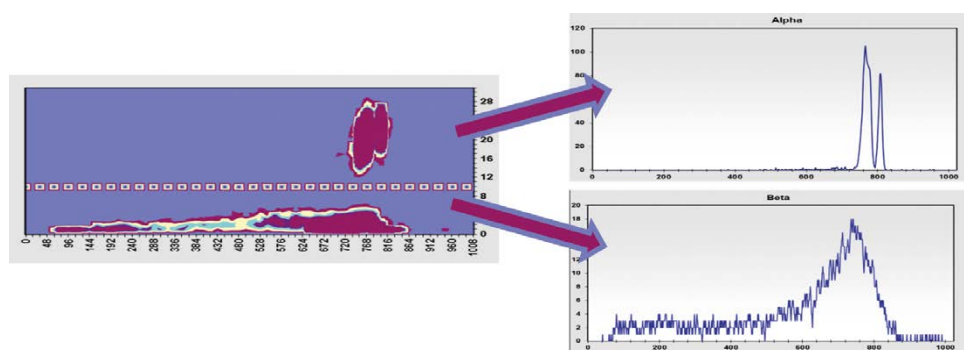
Figure 4-1 . *Separation of alpha – beta energies in the LSC device.*

4.4 Rn/Ra measurements by gamma counting

Two basic approaches, direct and indirect measurements, can be used for the gamma-ray spectrometric determination of [226]Ra in environmental samples (Girault et al. 2018, Jia and Jia 2012). The direct method is based on the gamma energy of 186.1 keV emitted by [226]Ra, but this line is not resolvable from the [235]U line of 185.74 keV by spectrum deconvolution. The interfering [235]U could be determined from the spectrum using other peaks of either [235]U itself, e.g. line at 143.8 keV with a probability of 11.0 %, or of the [238]U daughters [234]Th and [234m]Pa if the natural [238]U/[235]U activity ratio of 21.74 is given. However, in most practical cases the resulting counting statistical uncertainties are too large for this approach to be very useful.

The indirect approach, a more sensitive one, involves time- consuming equilibration between [226]Ra and its [214]Pb and [214]Bi progeny. After radon-tight sealing of the sample and waiting for about 3 weeks (the half-life of [222]Rn: 3.82 d) for secular equilibrium, [226]Ra is determined applying the gamma-rays of its daughter nuclides [214]Pb with line 295 and 352 keV, and [214]Bi with 609 and 1 120 keV. Figure 4-2 shows the gamma spectra of the background and 10 ml water sample ONK PP 324 (1.6.2016) of the Canberra XtRa (Extended Range Coaxial Ge Detector).

Conventional gamma-spectrometry at ground level, consisting of a Ge detector and passive shielding, cannot measure the low-level environmental radioactivity and achieve certain mandated detection limits for many sample types, because its integrated background of 0.4 cps per 100 cm^3 of Ge volume is often high. Therefore, low-background and high-purity germanium gamma-spectrometry should be used. The background in spectra is the contribution from cosmic rays and associated processes, radioactive impurities in the Ge detector end-cup, cryostat, electronics and microphonics noise, radioactive impurities in the shielding, gamma-rays from external natural radioactivity and radon and daughters in the air.

The [228]Ra determination could be provided by gamma spectroscopic measurement of [228]Ac, the daughter of [228]Ra. Although [228]Ac emits several gamma rays, some of them cannot be used for the [228]Ra determination due to interfering with other nuclides. The accurate [228]Ra determination must be based on the 911.16 keV peak with an intensity of 29 % or the sum of the 911.16 and 968.97 keV peaks with a combined intensity of 46.4 %.

The Gamma measurements were carried out using a Canberra XtRa (Extended Range Coaxial Ge Detector) detector which has a resolution of 2.1 keV. The spectra obtained were analyzed with Genie 2000 Gamma Acquisition & Analysis software. The effect of the measurement geometry was determined using multi-nuclide standard solution obtained from Eckert & Ziegler.

MDA in gamma counting for 186 keV energy peak is 0.28 ± 0.06 Bq, which is 0.056 ± 0.012 Bq/ml. It is emphasized that the high background count rate is due to the equipment and the surroundings in the measurement room. Conventional gamma spectrometry at ground level, consisting of a Ge detector and passive shielding, cannot measure the low-level environmental radioactivity and achieve certain detection limits low enough for many sample types, because its integrated background is often too high.
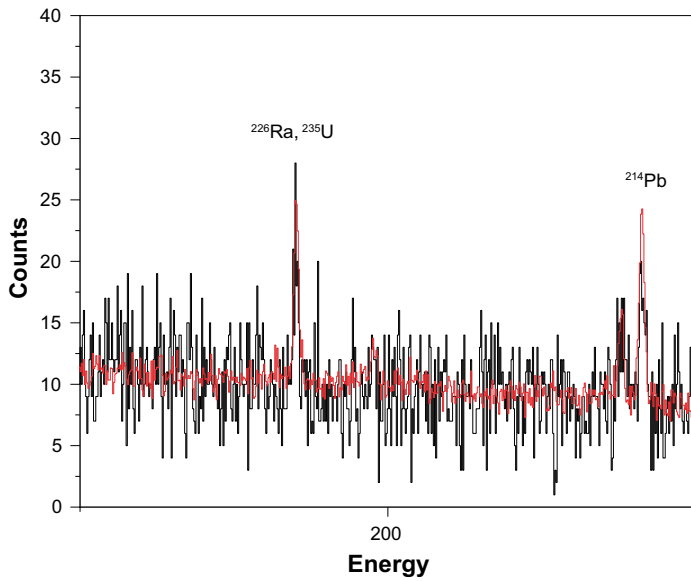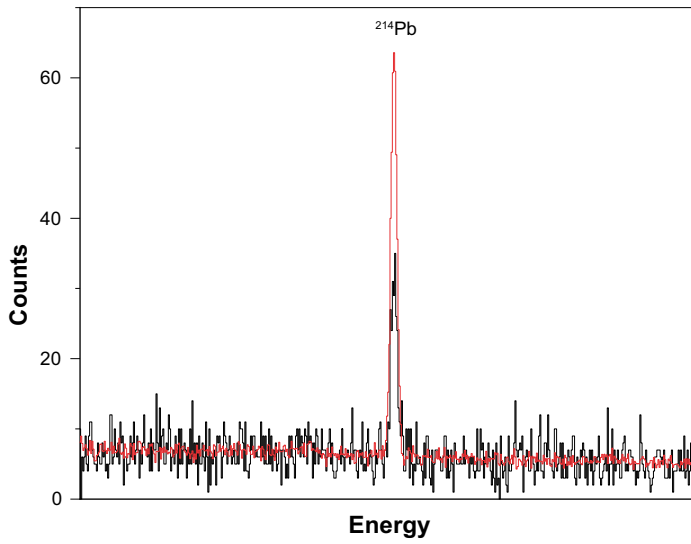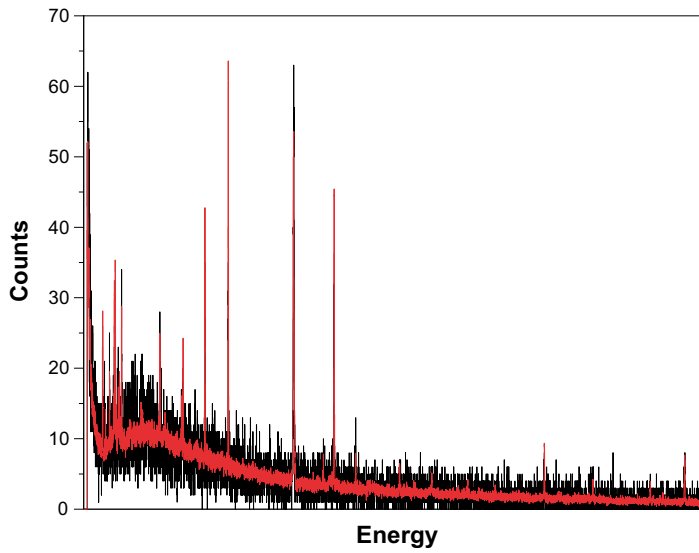
Figure 4-2. *The gamma spectra of the background (black) and 10 ml water sample ONK PP 324 (1.6.2016; red) of the Canberra XtRa (Extended Range Coaxial Ge Detector).*

4.5 Results

4.5.1 Radon and radium concentrations by the liquid scintillation counting method

Sampling from TDE observation holes was done twice from ONK-PP324 and three times from ONK-PP327. The results of [222]Rn and [226]Ra activity concentrations in Bq/l are shown in Table 4-1. The [222]Rn activities are decay corrected to the sampling time. Figure 4-3 shows the [222]Rn and [226]Ra spectra of ONK PP324 by liquid scintillation counting, the sample was taken on the 3rd of March 2020. Altogether five fracture water samples were taken in duplicate or triplicate during spring 2018, the results of [222]Rn and [226]Ra activity concentrations in Bq/l are presented in Table 4-2 as well as the results of the late 90s. The [222]Rn/[226]Ra ratios are given also in Table 4-2. In fracture water samples the values are calculated as weighed averages of the activities from the parallel samples. For the TDE observation hole samples, parallel results are shown separately. The groundwater in the TDE observation holes was simulated granitic groundwater with chemical composition listed in Table 4-3. The sample codes with the sampling depths and the chemical composition of the fracture waters at different sampling sites are shown in Table 4-3 too. Higher salinity and concentrations of Sr and Ba correlates to higher [226]Ra levels in groundwaters as seen in Figure 4-4 where [226]Ra activity concentration is presented as a function of chloride concentration in the fracture waters.

Table 4-1. Concentrations of [222]Rn and [226]Ra in REPRO TDE. Two values are given for two parallel samples taken. N.d. means that no activity above the background level was detected. The value with < sign means that the value is below a determined minimum.

Sampling site	Sampling date	[222]Rn Activity (Bq/l)	[226]Ra Activity (Bq/l)
ONK-PP324	21.1.2019	0.7 ± 0.3/n.d.	< 0.35/< 0.35
ONK-PP324	3.3.2020	2.9 ± 0.3/3.7 ± 0.3	0.120 ± 0.013 / 0.082 ± 0.011
ONK-PP327	21.1.2019	1.1 ± 0.4/n.d.	< 0.50/< 0.50
ONK-PP327	3.3.2020	3.0 ± 0.3/n.d.	0.104 ± 0.011 / n.d.
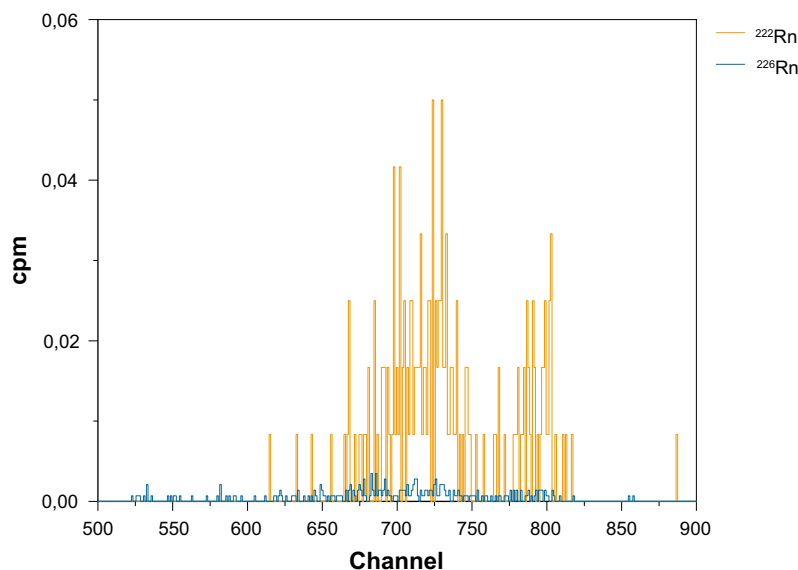
Figure 4-3. *An example of [222]Rn and [226]Ra spectra from liquid scintillation counting. (Water sample ONK PP324 3.3.2020).*

Table 4-2. Concentrations of ^{222}Rn and ^{226}Ra, and ^{222}Rn/^{226}Ra concentration ratio in different fracture waters of Olkiluoto.

Sampling site	^{222}Rn Activity (Bq/l)	^{226}Ra Activity (Bq/l)	^{222}Rn/^{226}Ra ratio
ONK-KR15 75.0−75.2 m	396 ± 3	3.8 ± 0.3	116 ± 6
OL-KR13 405.5−414.5 m	74 ± 3	2.5 ± 0.3	30 ± 3
OL-KR11 411−430 m	87 ± 3	0.6 ± 0.2	137 ± 14
OL-KR45 606−610 m	83 ± 3	10.4 ± 0.4	8 ± 3
OL-KR44 766−780 m	144 ± 3	113.1 ± 1.0	1.19 ± 0.04
ONK-PP324/3.3.2020 1	2.9 ± 0.3	0.120 ± 0.013	24 ± 2
ONK-PP324/3.3.2020 2	3.7 ± 0.3	0.082 ± 0.011	45 ± 4
ONK-PP327	3.0 ± 0.3	0.104 ± 0.011	29 ± 3

* Old data from Olkiluoto area; from late 90s.

Table 4-3. Concentrations of Cl, Na, Ca, Mg, Sr and Ba in the analysed fracture waters and in the synthetic granitic groundwater used in TDE experiment.

Sampling site	Cl (mg/l)	Na (mg/l)	Ca (mg/l)	Mg (mg/l)	Sr (mg/l)	Ba (µg/l)
ONK-KR15 75.0−75.2 m	5260	2180	1030	28	8.4	-
OL-KR13 405.5−414.5 m	4680	2020	850	34	7.7	-
OL-KR11 411−430 m	2340	1240	280	75	2.9	-
OL-KR45 606−610 m	10600	3770	2710	2.5	21	170
OL-KR44 766−780 m	27600	7420	9190	24	79	1900
REPRO TDE synthetic granitic groundwater	4793 ± 122	2519 ± 49	433 ± 31	30.6 ± 0.4	5.1 ± 0.1	-
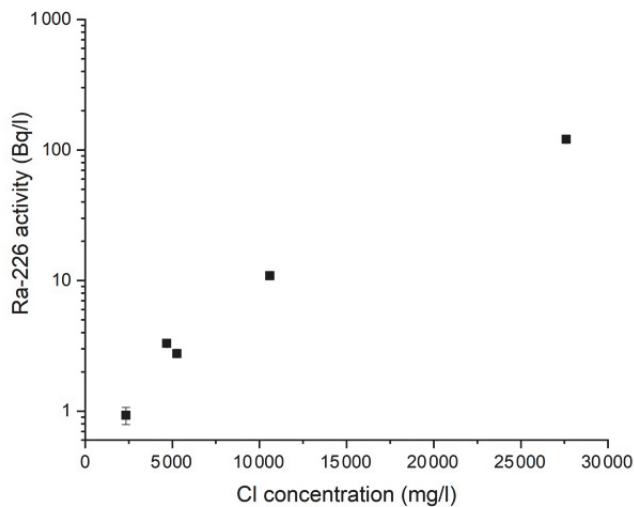
Figure 4-4. *^{226}Ra activity concentration as a function of chloride concentration in five analysed fracture waters.*
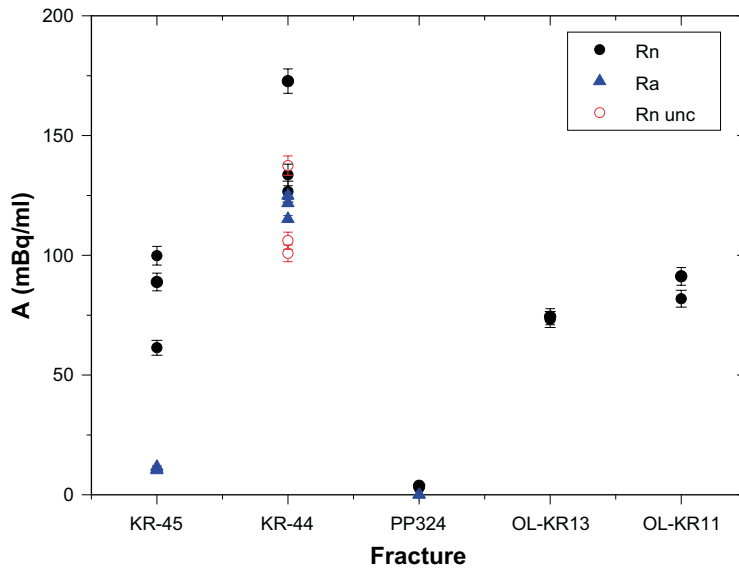
Figure 4-5. *Measured activities of ^{222}Rn and ^{226}Ra in the fracture water samples and ONK PP 324 samples.*

4.5.2 Radium concentrations by HPGe gamma detector

Table 4-4 presents the average net counting rate values from eight background measurements for main gamma peaks of naturally occurring radionuclides ^{235}U, ^{226}Ra, ^{214}Pb, ^{214}Bi and ^{228}Ac during 2020 by the HPGe gamma detector used in the measurements. These background gross counting rates (in counts per second, cps) are compared with the counting rates from the measured gamma spectra of ONK PP324 and ONK PP327 waters. The 10 ml water samples were concentrated from 200 ml of water taken from the boreholes ONK PP324 and ONK PP327 while emptying them for dismantling the equipment in March 2020.

Table 4-4. The average background cps values for nuclides $^{226}Ra+^{235}U$, ^{214}Pb, ^{214}Bi and ^{228}Ac by HPGe gamma detector.

Nuclide	Gamma energy (keV)	Background (cps)	ONK PP324 (cps)	ONK PP327 (cps)
$^{226}Ra+^{235}U$	186	0.0180 ± 0.0012	0.0185 ± 0.0017	0.0161 ± 0.0020
^{214}Pb	352	0.0227 ± 0.0053	0.0225 ± 0.0014	0.0229 ± 0.0012
^{214}Bi	608	0.0206 ± 0.0004	0.0213 ± 0.0008	0.0215 ± 0.0008
^{228}Ac	911	0.0035 ± 0.0002	0.0038 ± 0.0005	0.0038 ± 0.0005

The data in Table 4-4 shows that it was not possible to detect any increase of counting rate above the background level in any of the gamma peaks under observation. Therefore, the possible activities in the samples were below the detection limit of this method which is 0.056 ± 0.012 Bq/ml from the 186 keV gamma peak.

Minimum detectable activities (MDA) in the HPGe measurements has been estimated using the variation of the background in the detectors at the different gamma energies for radium daughters by applying Currie formulas (Currie 1968). The obtained MDA for the different isotopes is presented in Table 4-5 and are based on the measurements done when 200 ml sampled groundwater has been have evaporated to a 5 ml volume and put in the detector.

Table 4-5. The detection limits for the radium isotopes in the PP324 and PP327 final sampling of groundwater, measured using gamma spectrometry. The measurements were performed applying an evaporation of a 200 ml sampled groundwater to a 5 ml volume.

Nuclide	Proxy for activity of radium isotope	Gamma energy (keV)	MDA (Bq/l)
^{226}Ra	^{226}Ra	186	22
^{214}Pb	^{226}Ra	352	0.05
^{214}Bi	^{226}Ra	608	0.05
^{228}Ac	^{228}Ra	911	0.25

5 Inverse modelling by Kemakta: Modelling of Ra and Rn activities measured in Task 9C Extension

5.1 Introduction

The final measurement results obtained in the Task 9C Extension and presented at the virtual GWTFS meeting 39 were decidedly unexpected with ^{226}Ra and ^{222}Rn activities about 1–2 orders of magnitude lower than expected for the 4.92 y equilibration time under relatively undisturbed conditions. Although not part of the main Task 9C Extension modelling work as requested in the Task Description (see Appendix A), the measured activities were sufficiently unusual compared to typical groundwater measurement data for the ONKALO site that additional exploratory calculations were made.

This work was intended as both a test case for a new model of natural decay chain transport developed by Mahmoudzadeh and Crawford[2], and also a feasibility study of Bayesian parameter estimation for transport models using an approach based on a Markov Chain Monte Carlo (MCMC) technique (see e.g., Speagle 2020). The new model for decay chain transport is an extension of the model developed previously by Mahmoudzadeh et al. (2014) which includes source terms for natural radionuclides in the rock matrix and fracture coatings as well as an arbitrarily defined boundary condition at the start of a transport flowpath. Although the extended transport model is formulated for an advective flow system, the code can be simply modified to obtain a solution for the problem describing 1-dimensional diffusive transport to and from a stationary volume of water representing the packed borehole section monitored in the REPRO TDE experiment.

5.1.1 Overview of transport model

The extended model for the 1D borehole diffusion problem is simplified by considering a rectilinear diffusive domain rather than the radially symmetric diffusion problem in cylindrical coordinates. From penetration depth theory (see Crawford and Löfgren 2019; also, Neretnieks 2013), the average depth from which release of a decaying radioelement will have an impact on the diffusive flux into the borehole section is given by the relation:

$$\delta_p = \sqrt{\frac{D_p}{R_p \lambda}} \tag{5-1}$$

For a ^{222}Rn atom produced by decay of ^{226}Ra, the average release depth is estimated to be on the order of 3-7 mm based on the prior data estimates given in Table 5-2 and Table 5-3 and their uncertainties. For production of ^{226}Ra from decay of ^{230}Th, on the other hand, the average release depth is probably about 0.5–2 cm based on the same data. Since the outer diameter of the borehole section is roughly 5.7 cm the assumption of rectilinear coordinates should have only a minor impact on the results, although we leave testing this assumption to later work.

As outlined in the Task Description, nuclides belonging to the ^{238}U decay chain exist naturally in the rock matrix in the form of small formation mineral inclusions (e.g., allanite, monazite, zircon) typically found in biotite as well as more recently formed uranium-containing micro-precipitates hosted in matrix microfractures and grain boundary porosity. Typical uranium-containing phases here might include uraninite, (urano)thorite, haiweeite, uranophane, and coffinite (Krall et al. 2015). When ^{238}U or any of its descendent nuclides undergo α-decay, the resultant α-particle and decay nucleus recoil in opposite directions. The stopping distance for the recoiling nucleus is typically on the order of a few tens of nm, while that for α-particles can be 700 times further. In granitic rocks, the fraction of recoiling nuclei that end up in the water filled transport porosity can be very low depending on the location of the uranium minerals in relation to the water filled porosity as well as the aperture of the pore spaces into which the recoiling atoms are ejected. The fraction of decay recoils captured by the porewater is simultaneously one of the most important as well as most uncertain parameters governing the emanation of mobile ^{226}Ra and ^{222}Rn from the rock matrix due to α-recoil processes.

---

[2] Manuscript in preparation.

In the present work, we prefer to use the term "recoil capture fraction" to describe the primary capture of recoil atoms in the porewater adjacent to U-enriched source minerals in the rock matrix. This is because the term "emanation fraction" as it is frequently used in the literature concerns effective emanation from a bulk sample which implicitly includes the additional impact of diffusive transport and decay in the porosity of the sample before it can be measured in the headspace of a sampling vessel. In most cases the emanation fraction measured on bulk materials will be less than the true recoil capture fraction owing to diffusive transport resistance in the material depending on how the measurements have been performed and whether the samples are dry, or water-saturated.

Although it is possible to theoretically calculate the recoil capture fraction for very specific porespace representations with well-defined pore aperture and grain size for primary U-containing minerals, it is a parameter that realistically can only be estimated by measurement of Rn out-gassing rates from monolithic or crushed rock samples in the laboratory combined with modelling interpretation (as the empirically determined emanation factor including transport effects is not conceptually the same as the recoil capture fraction used for defining source terms in a model). Furthermore, when descendent nuclides in the ^{238}U decay chain prior to ^{226}Ra are ejected into the porespace, they migrate diffusively in the porewater and additionally contribute to the production of ^{226}Ra and ^{222}Rn due to the ongoing decay process. The description is complicated, however, since radionuclides undergoing α-decay may implant their progeny into aluminosilicate minerals lining the matrix porespace by the same process by which the progenitor radionuclides are released to the porewater. For even very mildly sorbing radioelements in the ^{238}U decay chain the fraction of progeny "lost" by this process is typically equal to or greater than 50 %, although a fraction of the descendants of implanted nuclides can return to the porewater by subsequent α-decay processes. This loss mechanism is typically ignored in safety assessment since it has a limited impact on radiological safety given other uncertainties, although it may be important for estimation of the natural radionuclide production rate in the rock matrix.

In this work, the primary recoil capture process is considered together with decay of mobilised nuclides in the porewater, although the additional impact of implantation has been neglected. Although implantation and subsequent return of descendants to the pore-water may turn out to be a significant mechanistic feature, inclusion of this would require non-trivial modifications to the mass balance and possibly the inclusion of additional adjustable parameters depending upon simplifications made in underlying modelling assumptions. It is also not clear whether the dynamics of this process can be included in a transient model in a simple fashion without introducing assumptions that are only strictly valid for steady-state conditions. For the present analysis, however, we test several different assumptions concerning the production rate of ^{226}Ra and ^{222}Rn to see if a simplified description of α-recoil can capture the main aspects of the emanation process as reflected in measured activities in the monitored borehole section.

The diffusion problem is formulated analytically in the frequency domain (Laplace) and the time domain solution is then obtained by numerical inversion of the frequency domain solution using the algorithm described by de Hoog et al. (1982) using the Matlab implementation by Hollenbeck (1998). Since the underlying transport model is basically a standard Fickian diffusion model for a stirred vessel of limited volume, we focus mainly on a description of the underlying assumptions for the ^{238}U decay chain here. The details of the underlying model Laplace model, however, is described in Mahmoudzadeh and Crawford[3]. In this work, three different model variants M1-M3 are explored:

M1) Full decay chain starting from ^{238}U with coupled mass balances for production of descendent nuclides;

M2) An abbreviated decay chain with coupled production of ^{226}Ra and ^{222}Rn;

M3) A simplified decay chain with non-coupled production of ^{226}Ra and ^{222}Rn.

Although it is possible to define separate, "effective" recoil capture fractions for each nuclide in the decay chain to account for differences arising due to implantation and other non-accounted for mechanisms, in the present calculations we assume an average recoil capture fraction, η_p that is the same for each nuclide in the modelled decay chain. Theoretically, the true recoil capture fraction
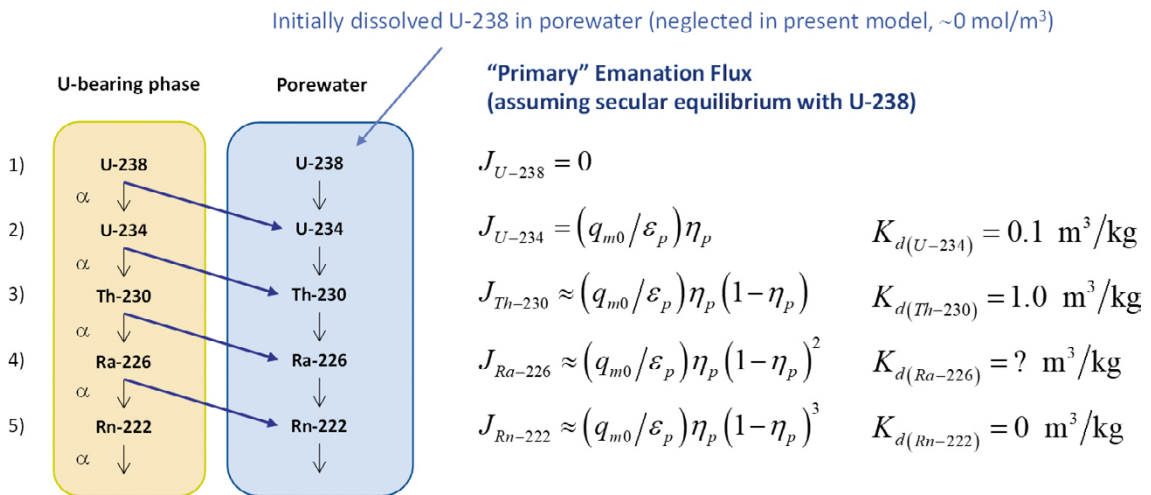
---

[3] Manuscript in preparation.

might differ by as much as 13 % between the different ^{238}U chain nuclides due to their differing decay energies. The difference is sufficiently small, however, that a single average value is deemed sufficiently accurate for the present analysis.

The coupling between nuclides in the decay chain is achieved by consideration of depletion of descendant atoms in the first ~ 15 nm, or so near the surface of the source mineral grains due to recoil loss. In this conceptualisation, a descendant atom that is ejected in one decay step is subsequently unavailable to contribute towards the emanation of nuclides in subsequent decay steps, although it may contribute by decay within the mobile porewater. This coupling between the source terms for different nuclides is important to avoid "double-counting" the rate of activity production in the rock matrix when more than one member of the decay chain is considered. This is a broadly similar approach to that described by Sun and Semkow (1998). The main assumptions implicit in model variant 1 are shown in Figure 5-1.

The primary flux of each ^{238}U descendent is formulated in terms of the total activity, q_0 (Bq/m^3) of ^{238}U in the rock and the average recoil capture fraction, η_p as indicated in Table 5-1. This also assumes that the primary U-bearing mineral phases are sufficiently old that isotopic equilibrium has been attained and descendent nuclides are present at roughly the same activity level as ^{238}U. The activity of ^{238}U can be estimated from the geochemical mass fraction of U (ppm) using the formula:

$$q_0 \approx m_U \left(\frac{10^3}{238} \right) \rho_b N_{av} \lambda_{U-238} \tag{5-2}$$

In principle, the U-content of the rock, m_U can be assigned from the average U-content of the site-specific rock type comprising the borehole section being studied. For the veined gneiss (VGN) at ONKALO the average U-content is 7.7 ± 3 ppm (Table 3-1 in Task Description), although this may differ locally from that in the rock comprising the PP327 borehole section being studied. The primary flux of recoil nuclides entering the matrix porewater for each of the model variants is shown in Table 5-1. The choice of flux model has a strong impact on the absolute level of porewater activity. The contribution of porewater ingrowth in the full chain description, for example, can give as much as four times the ^{222}Rn activity as that calculated by the simple model for a given η_p.

Initially dissolved U-238 in porewater (neglected in present model, ~0 mol/m^3)

"Primary" Emanation Flux
(assuming secular equilibrium with U-238)

U-bearing phase	Porewater
1) U-238	U-238
2) U-234	U-234
3) Th-230	Th-230
4) Ra-226	Ra-226
5) Rn-222	Rn-222

$J_{U-238} = 0$

$J_{U-234} = \left(q_{m0} / \varepsilon_p \right) \eta_p$ $K_{d(U-234)} = 0.1$ m^3/kg

$J_{Th-230} \approx \left(q_{m0} / \varepsilon_p \right) \eta_p \left(1 - \eta_p \right)$ $K_{d(Th-230)} = 1.0$ m^3/kg

$J_{Ra-226} \approx \left(q_{m0} / \varepsilon_p \right) \eta_p \left(1 - \eta_p \right)^2$ $K_{d(Ra-226)} = ?$ m^3/kg

$J_{Rn-222} \approx \left(q_{m0} / \varepsilon_p \right) \eta_p \left(1 - \eta_p \right)^3$ $K_{d(Rn-222)} = 0$ m^3/kg

Figure 5-1. Schematic representation of primary radionuclide fluxes from U-bearing mineral phases in the rock matrix (diagonal blue arrows), as well as in-situ production (vertical downward arrows) due to decay in the mineral phase and pore water. The net primary flux, J_k of each nuclide, k in the decay chain considers the α-recoil depletion of preceding progenitors to avoid double counting of activity production in the porewater. U and Th are assigned arbitrarily high K_d-values, while Rn is considered non-sorbing and that for Ra is treated as an unknown parameter to be fitted.

Table 5-1. Primary recoil fluxes for each of the three model variants considered in this study. Although the same symbol for recoil capture fraction, η_p appears in the flux terms for each of the models, it has different contextual meanings as an effective parameter and therefore might be expected to have different best estimate values in each model with optimised parameters.

Nuclide	M1 (full chain)	M2 (abbr. chain)	M3 (simple)
^{234}U	$q_0\eta_p/\varepsilon_p$	n/a	n/a
^{230}Th	$q_0\eta_p(1-\eta_p)/\varepsilon_p$	n/a	n/a
^{226}Ra	$q_0\eta_p(1-\eta_p)^2/\varepsilon_p$	$q_0\eta_p/\varepsilon_p$	$q_0\eta_p/\varepsilon_p$
^{222}Rn	$q_0\eta_p(1-\eta_p)^3/\varepsilon_p$	$q_0\eta_p(1-\eta_p)/\varepsilon_p$	$q_0\eta_p/\varepsilon_p$

Depletion of descendent nuclides in the surface layer of U-containing grains together with ingrowth of descendants from previously ejected progenitors puts a relatively strong restriction on the feasible envelope of relative concentration/activity ratios at equilibrium for ^{226}Ra and ^{222}Rn. The variation of the Rn/Ra ratio (total sorbed plus dissolved activity) is shown in Figure 5-2 as a function of η_p for the M1 and M2 model variants considered in this work and assuming a range of porewater losses (0–100 %) due to α-recoil in the porewater. The M3 model is not shown in Figure 5-2 since the total activity of the ^{222}Rn is trivially equal to twice that of ^{226}Ra owing to the primary recoil flux plus porewater ingrowth from the decay of Ra (which are of equal magnitude).
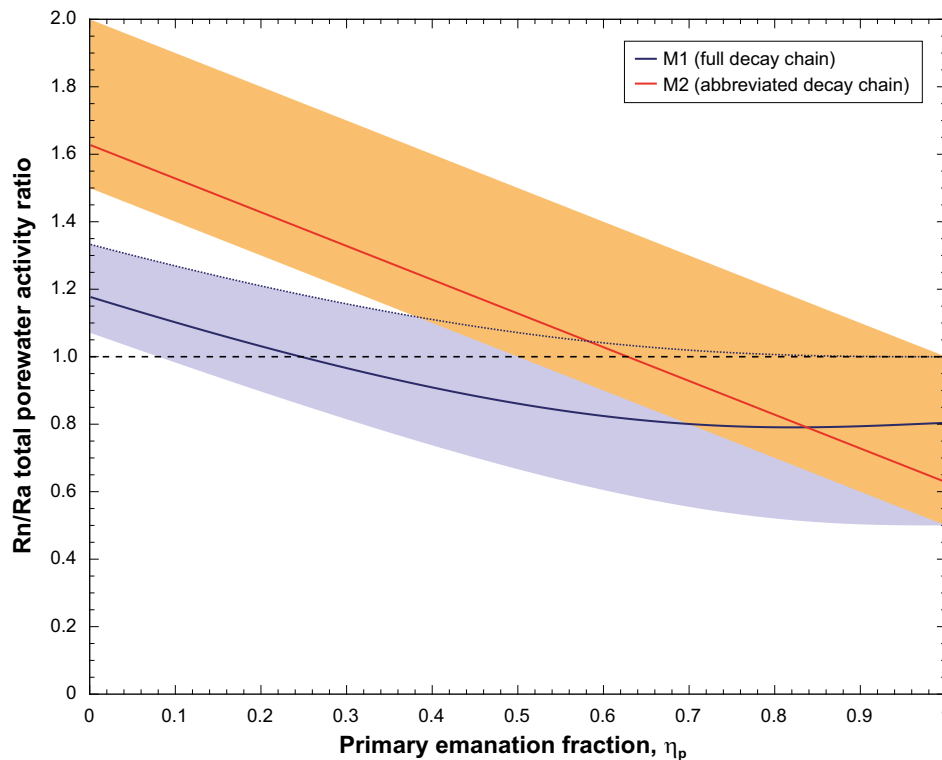
Figure 5-2. *Variation of the total (sorbed plus mobile) porewater activity ratio for ^{222}Rn and ^{226}Ra as a function of the recoil capture fraction in the M1 and M2 model variants considered in this work. Shading indicates the range of uncertainty arising due to not considering the additional recoil capture processes (i.e., retention in matrix minerals and secondary recoil fluxes) involving α-decaying nuclides in the porewater. The solid curves assume a recoil loss of 50 % from porewater to matrix minerals flanking the porespace in each step of the decay chain, while the shaded regions cover the range of 0 %–100 % recoil losses for porewater α-decays.*

It is interesting to note that for both the full chain model (M1), and abbreviated chain model (M2), the total porewater activity ratio approaches a limiting value of unity for a primary recoil capture fraction of 100 % corresponding to secular equilibrium (thus indicating preservation of the radio-nuclide mass balance) if porewater losses are neglected. The simplified model (M3), where depletion of the primary phase is not considered, clearly results in a double counting of activity production which is obviously incorrect for recoil capture fractions above 50 % since more activity is emanated than what can be produced in the primary mineral phase. The simplified model may still be useful at lower recoil capture fractions, however, if it is understood as an effective average value. In previous work, the simplified model (M3) has been assumed although only for low recoil capture fractions in the range of 1 %–10 % (Crawford 2010). Calculations of natural radionuclide emanation incorporating full decay chains or even abbreviated decay chains with additional consideration given to the total activity mass balance appear to be uncommon in the literature, although with some notable exceptions (e.g., Sun and Semkow 1998, Diego-Feliu et al. 2021).

As noted previously, the value of 50 % loss is a maximum value for large average pore apertures (> 80 nm) and assumes negligible return of activity due to subsequent α-recoils of descendent nuclides. If full mass balance accounting of implantation and porewater return fluxes is made, the Rn/Ra ratio curve would most likely reside somewhere in the shaded envelope of variability for the M1 and M2 models as shown in Figure 5-2. For very narrow average pore apertures, on the other hand, the Rn/Ra ratio curve would most likely reside closer to unity as most of the porewater ingrowth would likely be lost by implantation. Although the full decay chain description neglects implantation loss, the inclusion of this mechanism seems to only have a minor impact on the relative Rn/Ra ratio at equilibrium. Neglection of implantation loss may have a larger impact on absolute equilibrium activity by up to a factor of four (or more for very narrow pores) in model M1, although this might be at least partially compensated for by adjustment of the effective q_0 value (i.e., accessible U-content of the rock). For this reason, we regard the accessible uranium content of the rock as an uncertain parameter that might be less than the estimated bulk geochemical abundance.

5.1.2 Overview of the MCMC modelling approach

Although an exhaustive overview of the Markov Chain Monte Carlo (MCMC) modelling technique is beyond the scope of this work, we provide a short description here to aid understanding what has been done in the present exploratory modelling work. There is an enormous pool of literature that has grown over the last several decades concerning MCMC and it has found applications in an extremely diverse landscape of scientific endeavour spanning topic areas such as astrophysics, biostatistics, climatology, epidemiology, and ecology to name just a few. Unfortunately, many of the foundational articles (e.g., Metropolis et al. 1953, Hastings 1970) and canonical texts (e.g., Gelman et al. 2003) are theoretically dense and difficult to parse for non-statisticians. Very good general summaries of the technique, however, are given in e.g., Speagle (2020), Geyer (2011) and van Ravenzwaaij et al. (2018). In many respects, it can also be added that the basic concepts of MCMC are frequently easier to understand intuitively if approached from a computational or coding perspective rather than abstract theoretical reasoning (e.g., Davidson-Pilon 2015).

A particular strength of MCMC is that it allows one to infer properties of probability distributions which may not be representable in closed form or even explicitly computable. In the context of parameter estimation where it is frequently invoked, MCMC is also closely associated with Bayes theorem where we are primarily concerned with estimation of conditional probabilities:

$$p\left(\theta|D,M\right) = \frac{p\left(D|\theta,M\right)\cdot p\left(\theta|M\right)}{p\left(D|M\right)} = \frac{prior \times likelihood}{evidence} \tag{5-3}$$

Here, we are attempting to estimate the conditional probability, $p(\theta|D, M)$ of parameter values, θ given the observed data, D (i.e., measurements) and a model, M. This is also termed the "posterior" conditional probability distribution of θ. Assuming the utility of the model, M as given, Equation 5-3 can be written more compactly as (Speagle 2020):

$$\pi\left(\theta|D\right) = \frac{\pi_0\left(D|\theta\right)\cdot \mathsf{L}\left(\theta\right)}{\int \pi_0\left(D|\theta\right)\cdot \mathsf{L}\left(\theta\right)d\theta} \propto \pi_0\left(D|\theta\right)\cdot \mathsf{L}\left(\theta\right) \tag{5-4}$$

Typically, in the natural sciences there is more than one model hypothesis which can be conceived to explain phenomena. The denominator in equation is termed the "evidence" for the model and is a normalising constant obtained by integrating over all feasible θ (Equation 5-4). Unfortunately, calculating the normalising constant is quite tedious for high-dimensional problems (i.e., more than about three θ-parameters). Unless one is attempting to select between different candidate models, however, it is not necessary to calculate the normalising constant since it does not affect the statistical properties of the posterior distribution.

The first term, $p_0(\theta)$ in the numerator on the right-hand side of equation is the "prior" belief or estimated uncertainty distribution for θ based on existing knowledge. The prior can be assessed from independent information, expert elicitation, or even just a ballpark guess if little information is available. In some cases, we might have good prior information and can assign a well-bounded uncertainty distribution (e.g., normal or log-normal). In other cases, we might not have very good prior knowledge and then need to use a very broad uncertainty distribution.

The formation factor, for example, can be assessed relatively accurately from independent experiments, so a normal or log-normal distribution might be a good choice for a prior. On the other hand, the effective recoil capture fraction, η_p is not well known for intact site-specific rock. In such cases, one may invoke a uniform prior where equal probability is assigned to any value in the range. The use of "improper" priors such as a uniform distribution, however, is often frowned upon by statisticians since it does not make full use of existing information. In the case of the η_p parameter, both extremes of the feasible range may be considered unlikely on physical grounds and therefore should not have the same probability as values close to the centre of the range. In such cases, a symmetric β-distribution centred at 50 % (e.g., b(2, 2)) might be a better choice for a variable that can take on any value in the range 0–100 %. Another possibility is to make a logit transformation of the parameter and assume a normal distribution with large variance for the transformed parameter.

The second term on the right-hand side of equation is the "likelihood" function. The likelihood, $\Lambda(\theta)$ is the probability of the parameter, θ for the model, M. It is typically formulated in terms of a sum-of-squares function since it is closely related to the maximum log-likelihood function for a model fitting process. In this respect, the formulation of an MCMC problem bears many similarities to a standard non-linear least squares (NLS) optimisation problem. The main difference, of course, is that in NLS one attempts to quickly find an optimal θ that minimises the cost function (or maximises the log-likelihood function), but very little information is obtained concerning the uncertainty of the optimised parameter combination. MCMC, on the other hand, seeks to find the optimum θ after a "burn-in" period of down-gradient random walks and then continues to probe the neighbourhood of the optimum to estimate the uncertainty of θ.

NLS is always much faster to find a solution, although typically does not have much to say about parameter uncertainty. MCMC will continue to sample the posterior distribution for as long as one cares to run the simulation. After discarding the burn-in values of the θ-chain, and assuming that the chain has converged to a "well-mixed" ergodic state, then inferences can be made about θ from the stochastic values comprising the chain. Assessing chain convergence is more of an art than a science although there are some general convergence criteria and rules of thumb that can be applied, as well as some useful numerical tools (see e.g., Roy 2020). Convergence can often, but not always, be assessed visually by plotting the sum-of-squares error against iteration number.

There are a number of different algorithms for simulating Markov chains for MCMC, including the ubiquitous Metropolis-Hastings algorithm (Hastings 1970) and the Gibbs sampler (e.g., Gelfand 2000). It is hard to overestimate the impact that the Metropolis-Hastings algorithm has had on science and engineering and it is widely regarded as probably the most influential algorithm of the 20th century (Dongarra and Sullivan 2000). The main innovations since the original implementation have typically been more efficient means of sampling the parameter space as well as special techniques to avoid slow convergence of chains for problems with unusually shaped response surfaces for the sum-of-squares error, multimodal optima, etc. In the present work, we use the Delayed Rejection Adaptive Metropolis (DRAM) method as described by Haario et al. (2001, 2006) and implemented in the open source Matlab toolbox **mcmcstat** (Laine 2018).

5.1.3 Model parameterisation and prior uncertainty distributions

The central parameters for the present problem are:

1) Effective recoil capture fraction, η_p.

2) Accessible U-content of the rock matrix, m_U.

3) Sorption partitioning coefficient for ^{226}Ra sorption, $K_{dm(Ra)}$.

4) Formation factor, F_f.

There are, of course, additional parameters which must be specified such as free solute diffusivities, transport porosity, rock density, and K_d values for the more strongly sorbing radioelements U and Th. In the present exploratory modelling work, these are thought to have only a very minor impact on the results so are assumed as fixed values (or conservative "guesstimates" in the case of K_d for U and Th).

Each of the central parameters have varying degrees of uncertainty. The recoil capture fraction is not well known for the intact site-specific rock and could vary, in principle, from close to 0 % to 100 %. This is obviously a highly uncertain parameter that has a large impact on the result. The U-content of the VGN rock-type, on the other hand, is known from geochemical statistics to be 7.7 ± 3 ppm and might be considered a well-bounded stochastic variable. Since the model simplifies the description of recoil capture in the porewater and the value of η_p puts a constraint on the relative production rate of Ra and Rn (see Figure 5-2), it is possible that the "effective" porewater accessible U-content required to model the correct radionuclide flux might differ from the total U-content as it is known from geochemical statistical data.

The K_d value for Ra sorption has been estimated to be 0.06 ± 0.02 m³/kg from laboratory measurements on crushed samples of typical VGN rock in contact with synthetic groundwater of similar composition to that in the diffusion experiment. Making some allowance for bias related to crushing of rock and a limited statistical sample size, would allow for a reasonably well-bounded range of uncertainty. Rn was assumed to be non-sorbing and therefore assigned a K_d value of zero. We have a priori specified relatively high K_d values of 0.1 m³/kg for U and 1.0 m³/kg for Th which gives a relatively low mobility in the rock matrix. It is thought that this assumption has a relatively small impact on the results, although this will likely need to be tested by sensitivity analysis in follow-up work. Sorption of radionuclides on the inner surface of the borehole section was described using an equivalent "retardation factor" based on a rescaled K_d value. It is analogous to the equilibrium retardation parameter used in advective-dispersive models of transport and defined as:

$$R_f = 1 + \frac{K_{dm}}{A_{rock}} \cdot \left(\frac{A_x}{V_w} \right) \tag{5-5}$$

Where K_{dm} (m³/kg) is the rock matrix K_d value, A_{rock} (m²/kg) is the specific surface area of the rock matrix, A_x (m²) is the diffusive surface area of rock in the borehole section, and V_w (m³) is the volume of water circulating in the borehole section. The A_{rock} parameter is not well-known for site specific rock and a value of ~20 m²/kg (André et al. 2008, 2009) has been assumed based on measurements of intact samples of Swedish granitic rock from site investigation areas (the same assumption was made by the KTH-ChemE modelling group from which the surface area value has been taken (Table 3-2)). For K_d values below about 0.01 m³/kg, the R_f value is approximately unity and has very little impact on results.

The geometric formation factor of $4 ± 2 \times 10^{-4}$ is derived from independent experiments and is considered relatively well-bounded, deviations from ideal behaviour notwithstanding. Free diffusivities of radionuclides are calculated using the Stokes-Einstein equation (CRC 2000) assuming infinite dilution together with an approximate correction for temperature and salinity based on the viscosity of water calculated at the in-situ temperature (12 °C) and salinity (9.161 g/kg$_{solution}$) relative to the reference condition of pure water at 25 °C. The viscosity correction is only approximate and based on a model for thermophysical properties of seawater by Sharqawy et al. (2010) and Nayar et al. (2016). The molar conductivity for Ra^{2+} was taken from CRC (2000), U(VI) as UO$_2$(CO$_3$)$_3^{4-}$ from Yamaguchi and Nakayama (1998), and Th^{4+} from Mauerhofer et al. (2004). The free diffusivity of Rn in water was taken from Rona (1917) as 1.13×10^{-9} m²/s without correction for temperature or salinity (after 100 y this interestingly remains the most authoritative work on Rn diffusivity in the

aqueous phase). The density of the rock was assumed to be the same as that of the average VGN rock (2 714 kg/m^3), while the transport porosity was assumed to be fixed at 0.5 % in line with values given in the Task Description. A summary of the fixed parameters used in the modelling work is given in Table 5-2.

Table 5-2. Parameter values considered fixed in the MCMC calculations carried out for this work.

Parameter	Value	Description
A_{rock}	20 m^2/g	BET surface area of rock matrix (André 2008, 2009)
ε_{pm}	0.5 %	Transport porosity of rock (Task 9C TD*)
ρ_b	2 741 kg/m^3	Bulk density of VGN rock type (Task 9C TD*)
A_x	0.178 m^2	Surface area for mass transport (Task 9C TD*)
V_w	3.13×10^{-4} m^3	Total recirculating water volume in test section (Task 9C TD*)
K_{dU}	1.3 m^3/kg	Assumed value
K_{dTh}	10 m^3/kg	Assumed value
D_{wU}	8.14×10^{-11} m^2/s	Free diffusivity of U (viscosity-corrected Stokes-Einstein relation)
D_{wTh}	3.16×10^{-10} m^2/s	Free diffusivity of Th (viscosity-corrected Stokes-Einstein relation)
D_{wRa}	6.03×10^{-10} m^2/s	Free diffusivity of Ra (viscosity-corrected Stokes-Einstein relation)
D_{wRn}	1.13×10^{-9} m^2/s	Free diffusivity of Rn (Rona 1917)

(*) Task 9C Task Description (Andersson et al. 2020).

For the central stochastic parameters in the MCMC simulations, we introduce variable transformations since the DRAM algorithm implemented in the **mcmcstat** modelling tool assumes a multivariate Gaussian proposal distribution. Since the effective recoil capture fraction, η_p is bounded on the interval [0.1] and the Laplace solution is undefined for $\eta_p = 0$, a logit transform was used when passing this variable:

$$\left.\begin{aligned} \theta_\eta &= \log\left(\frac{\eta_p}{1-\eta_p}\right) \\ \eta_p &= \frac{1}{1+\exp\left(-\theta_\eta\right)} \end{aligned}\right\} \tag{5-6}$$

For the other variables, lognormal variable transformations are used since they are non-zero, positively bounded variables with relatively broad uncertainty distributions ranging over several orders of magnitude. Since there is only a single measurement point of paired ^{226}Ra and ^{222}Rn activities, the diffusion problem is poorly constrained. Ideally, two or more paired activity measurements made at shorter times would be required to better constrain the model variables for the transient solution. Since the effective recoil capture fraction is very poorly known for this type of rock, a non-informative flat prior was assumed for θ_η (i.e., bounded uniform in log-space with infinite variance). The central calculation case assumes a Gaussian prior for θ_U, θ_K, and θ_F since these seem to be reasonably well-quantified (even if subject to some bias).

Table 5-3. Summary of stochastic variables in the MCMC problem. LB and UB signify the lower and upper bounds assumed for transformed variables. A bounded uniform prior was assumed for θ$_\eta$ while Gaussian priors were assumed for θ$_U$, θ$_K$, and θ$_F$ based on independent data given in the Task Description.

Variable	Transform	LB	UB	Prior mean	Prior std.
θ$_\eta$	logit(η_p)	−10	10	N/A	∞
θ$_U$	log$_{10}$(m$_U$)	−6	6	0.86	0.16
θ$_K$	log$_{10}$(K$_{dRa}$)	−9	3	−1.25	0.14
θ$_F$	log$_{10}$(F$_f$)	−9	0	−3.45	0.21

In all simulations, an initial optimum parameter combination was estimated on the bounded intervals using Nelder-Mead optimisation based on a modified version of the built-in Matlab function **fminsearch**. The results of the initial parameter optimisation were then used as an initial condition for the main MCMC simulations. In all cases, a burn-in of 3×10^4 iterations was used and only the final 5×10^4 iterations were kept as a result.

5.2 Results and Discussion

In the following sections, the modelling results are presented for the full decay chain (M1) and abbreviated decay chain (M2) models. For unknown reasons, it was not possible to obtain an acceptably accurate solution for the simple decay chain model (M3) using a Gaussian prior for θ_U. Since the M3 model is a trivial case that is known to be not physically correct (owing to "double counting" of activity), it is not discussed further in this section.

5.2.1 Full chain model (M1)

For the central calculation case, a bounded uniform prior was assumed for θ_η and Gaussian priors for θ_U, θ_K, and θ_F. As can be seen from Figure 5-3, a good match (light blue "+" markers) with the measurement data (red circular marker) could be obtained. The posterior parameter estimates for this simulation are given in Table 5-4. There is also a small offset between the values calculated at 4.95 y (light blue "+" markers) and the equilibrium steady state (red "+" markers in Figure 5-3).

The posterior K_d and F_f values are lower than their prior uncertainty estimates which is in line with expectations for intact rock under at least partial formation stress. The best estimate K_d value is about five times less than the laboratory derived value estimated from experiments involving crushed rock. This is anticipated on account of the known bias introduced by the crushing of rock samples which results in increased sorptive surface area. The best estimate formation factor is about 20 times less than the laboratory measured value. This might also be a consequence of increased stress in-situ relative to laboratory samples, although it is not clear whether this argument extends to the first few mm, or so of rock matrix near the borehole surface which presumably dominate the diffusive transport resistance.

A much more interesting result, however, is that the posterior estimate for the accessible U-content ~ 0.19 ppm is 40 times less than the estimated mineralogical average for the VGN rock type (7.7 ppm). The best estimate recoil capture fraction, η_p is also relatively high at ~ 36 %. Very similar posterior estimates were also obtained using non-informative, uniform priors for all parameters (results not shown) which suggests that the result is representative for the borehole section under study and not biased by the choice of prior. To test this hypothesis further, the sum-of-squares function was calculated for m_U and η_p varied systematically over a wide range of possible values while holding the K_d and F_f values fixed at their central estimate posterior values. The results of this analysis are shown in Figure 5-8 and clearly indicate the presence of one or more optimal m_U and η_p combinations corresponding to the posterior estimate given in Table 5-4.

Table 5-4. Summary of posterior estimates for model parameters from MCMC simulations (5×10^4 realisations) assuming the full decay chain model variant (M1). Results are shown as θ-values directly estimated by the simulation tool, as well as inverted back to their arithmetic form.

θ-Variable (MCMC)		Inverted variable	
θ_η (logit)	-5.76 ± 0.43	η_p (%)	36.4 ± 0.1
θ_U ($\log_{10}$)	-0.76 ± 0.22	m_U (ppm)	0.19 ± 0.07
θ_K ($\log_{10}$)	-1.93 ± 0.15	K_d (m³/kg)	$(1.23 \pm 0.31) \times 10^{-2}$
θ_F ($\log_{10}$)	-4.96 ± 0.38	F_f (−)	$(1.84 \pm 2.5) \times 10^{-5}$
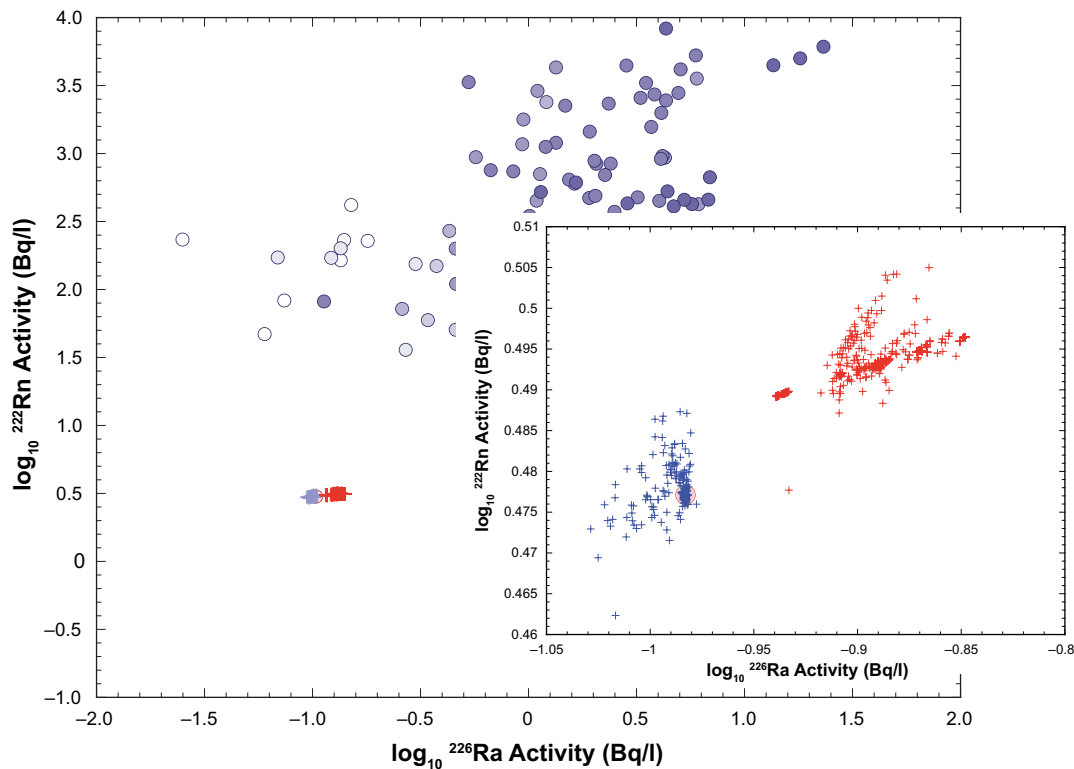
Figure 5-3. *Cross-plot showing measured activities of ^{222}Rn and ^{226}Ra for the REPRO-LTD experiment (red circle marker) with corresponding groundwater measurements made at the Forsmark site for context (blue circular markers). The Forsmark data are shaded proportionally with respect to the $\log_{10}$ of groundwater Ca^{2+} concentration with darker shading indicating higher Ca^{2+} concentrations. The light blue "+" symbols indicate 2000 randomly selected simulation results from the MCMC calculations for the full chain model (M1) exactly overlaying the measurement values calculated at 4.95 y. Red "+" symbols indicate the corresponding results calculated for steady-state conditions. A zoomed-in version of the figure (inset) shows the difference between the non-steady state and equilibrium results more clearly.*

It is difficult to ascertain an appropriate burn in length in the calculated MCMC chain (Figure 5-4), presumably because the starting condition for the calculation is already close to the optimal combination and because there is only a single measurement data point used as a basis for the calculation. It is also difficult to identify a clear burn-in or indeed chain convergence when examining trace plots for each of the sampled model parameters (Figure 5-5). The calculated MCMC chain does not appear to be well-mixed even after a few tens of thousands of iterations, although this might be an artefact of optimising against a single measurement point. The impact of measurement error was not considered in the MCMC calculations, although this could improve the smoothness of the sampled posterior distributions given that the sum-of-squares cost function is very tightly pegged to the single measurement point in the present scoping calculations.
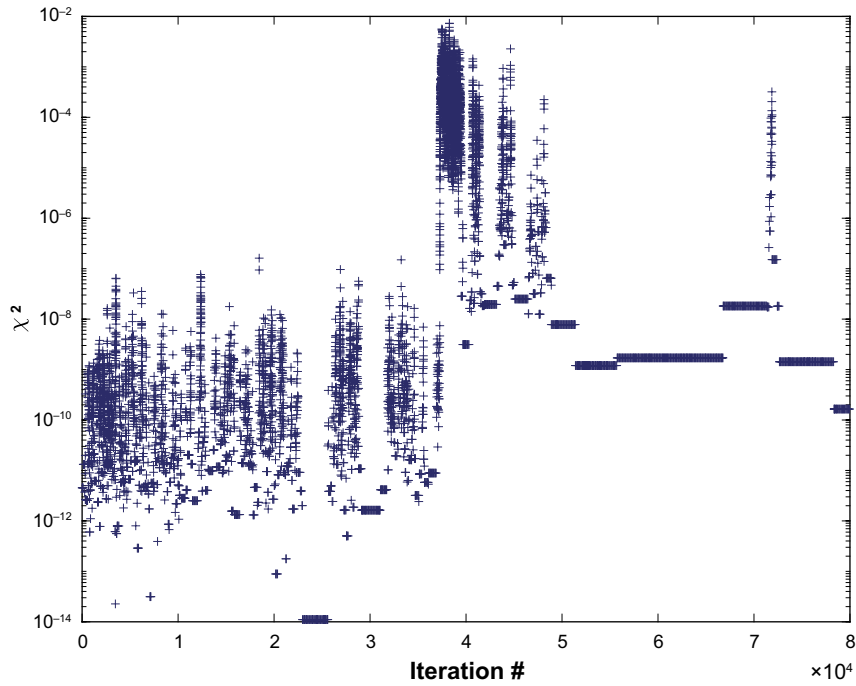
Figure 5-4. *Trace plot showing the calculated sum of squares as a function of iteration number. Although there is no clear burn-in for the sum of squares error, the first 3×10^4 realisations were discarded anyway leaving 5×10^4 realisations from which the posterior uncertainty distributions were calculated.*
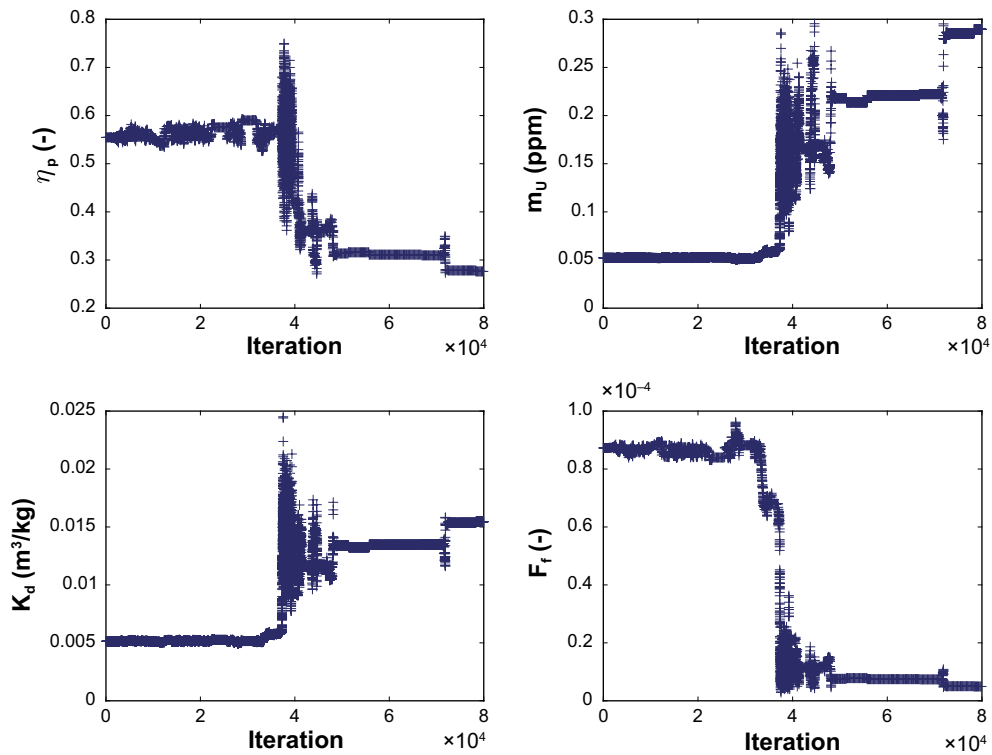
Figure 5-5. *Trace plot showing sampled parameter values as a function of iteration number. The first 3×10^4 realisations were discarded from the calculated chain leaving 5×10^4 realisations from which the posterior uncertainty distributions were calculated.*
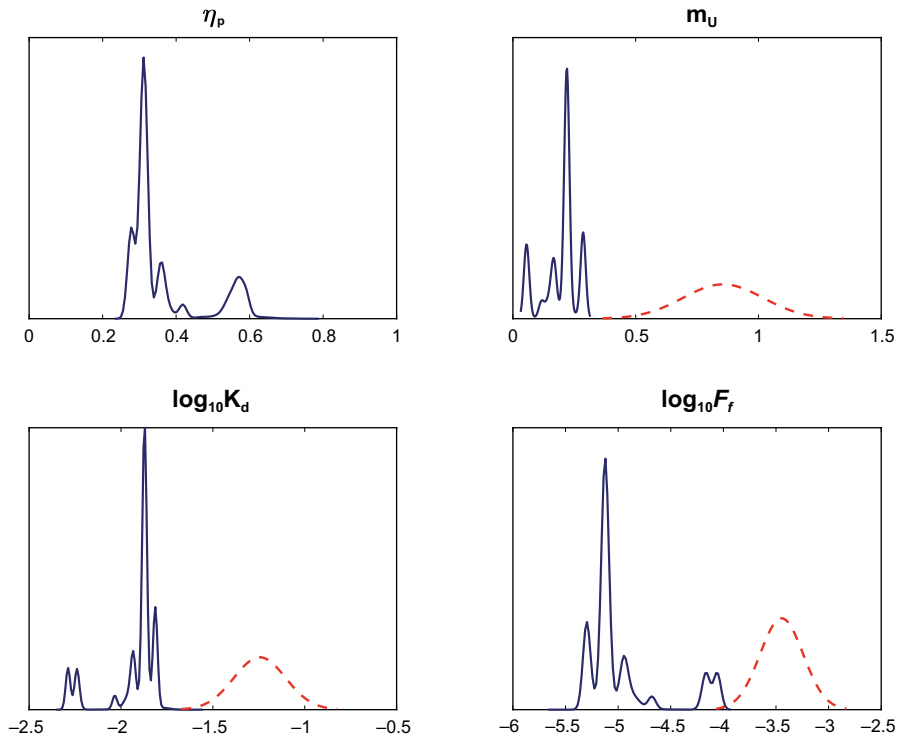
Figure 5-6. *Plot showing posterior probability densities (blue curves) calculated for 5×10^4 MCMC realisations of η_p, m_U, $\log_{10}K_d$, and $\log_{10}F_f$ after discarding the first 3×10^4 realisations as burn in. Results are smoothed using a Gaussian filter with a bandwidth of 2. To aid interpretation, the η_p and m_U parameters have been inverted from their transformed values used in the MCMC calculation and correspond to their arithmetic values. For m_U, $\log_{10}K_d$, and $\log_{10}F_f$ the prior Gaussian uncertainty distribution is also plotted (red broken curves).*
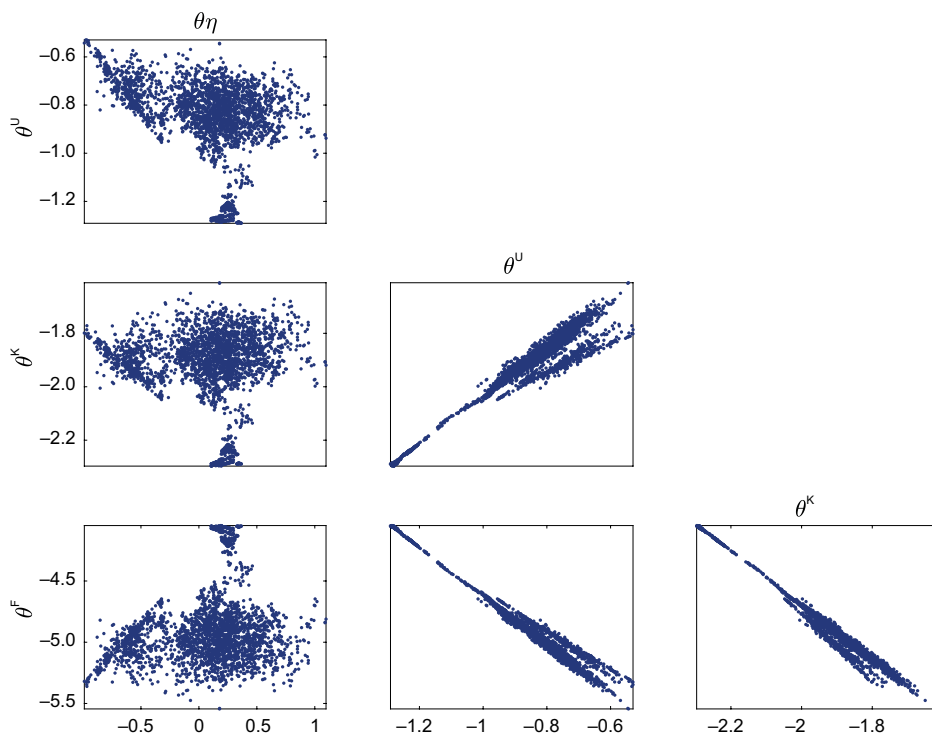
Figure 5-7. *Plot showing pairwise covariance of posterior model parameter estimates. While θ_U, θ_K, and θ_F exhibit relatively strong mutual correlations, there is no apparent mutual correlation between θ_η and θ_U, or θ_η and the other fitted parameters.*
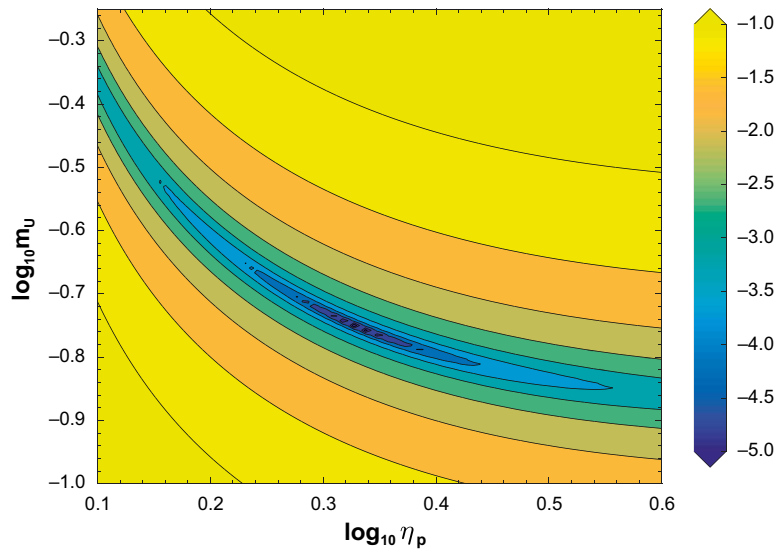
Figure 5-8. *Plot showing the sum-of-squares cost function (χ2) for systematically varied m_U (ppm) and η_p assuming $log_{10}K_d$ and $log_{10}F_f$ set to their best estimate values (θ_K and θ_F) from Table 5-4. There appears to be at least one, or more optimal parameter combinations for the full decay chain model (M1) in the immediate vicinity of $\eta_p >> 0.36$ and $m_U >> 0.06$ ppm as identified by the MCMC calculation tool.*

The posterior uncertainty distributions for each parameter are shown in Figure 5-6. These are calculated from the final 5×10^4 realisations of the MCMC chain and are presented as kernel density plots, smoothed using a Gaussian filter with a bandwidth of 2. It appears that there may be several very closely spaced minima (Figure 5-8) that the MCMC sampler hops between periodically. This might give rise to the long runs of nearly identical parameter samples punctuated by excursions to different stable regions in the chain (Figure 5-5). Figure 5-7 shows the pairwise covariance of the model parameters.

5.2.2   Abbreviated chain model (M2)

The abbreviated decay chain model (M2) only explicitly considers [226]Ra and [222]Rn, although their primary recoil fluxes are still coupled non-linearly by way of the correction for inventory depletion in U-containing mineral grains. [222]Rn is also generated by ingrowth in the porewater from [226]Ra decay. The calculated activities are shown Figure 5-9 and, as in the previous case, a good match (light blue "+" markers) with the measurement data (red circular marker) could be obtained using the posterior parameter estimates given in Table 5-5. Equilibrium is close, although not fully attained for the best estimate parameter combination after a contact time of 4.95 y and a small deviation is apparent for the steady-state solution (red "+" markers).

In this case the estimated effective recoil capture fraction, η_p is close to 100 % and is significantly larger than that calculated for the full decay chain model (~60 %). The estimated accessible U-content, however, is very similar in both the full chain and abbreviated chain models as is the posterior uncertainty distribution for both K_d and F_f. The two models exhibit a high degree of mutual consistency, and both suggest a lower accessible U-content than that estimated from whole rock geochemical analysis.

To check the potential existence of multiple optima, the sum-of-squares function was calculated for m_U and η_p varied systematically over a wide range of possible values while holding the K_d and F_f values fixed at their central estimate posterior values. The results of this analysis are shown in Figure 5-14 and clearly indicate the presence of a global optimum m_U and η_p corresponding to the posterior estimates given in Table 5-5.

Table 5-5. Summary of posterior estimates for model parameters from MCMC simulations (5×10^4 realisations) assuming the abbreviated decay chain model variant (M2). Results are shown as θ-values directly estimated by the simulation tool, as well as inverted back to their arithmetic form.

θ-Variable (MCMC)		Inverted variable	
$\theta\eta$ (logit)	8.69 ± 0.54	η_p (%)	99.98 ± 0.02
θ_U ($\log_{10}$)	-0.782 ± 0.06	m_U (ppm)	0.17 ± 0.02
θ_K ($\log_{10}$)	-1.82 ± 0.05	K_d (m³/kg)	$(1.53 \pm 0.17) \times 10^{-2}$
θ_F ($\log_{10}$)	-5.10 ± 0.12	$F_f (-)$	$(8.3 \pm 2.3) \times 10^{-6}$

As in the previous case, it is difficult to ascertain an appropriate burn in length in the calculated MCMC chain (Figure 5-10). It is also difficult to identify clear burn-in or chain convergence when examining trace plots for each of the sampled model parameters (Figure 5-11). As noted previously, the calculated MCMC chain does not appear to be well-mixed even after a few tens of thousands of iterations, although this could be an artefact of optimising against a single data point without additional consideration given to measurement error. The posterior uncertainty distributions for each parameter are shown in Figure 5-12. These are calculated from the final 5×10^4 realisations of the MCMC chain and are presented as kernel density plots, smoothed using a Gaussian filter with a bandwidth of 2. Figure 5-13 shows the pairwise covariance of the model parameters.
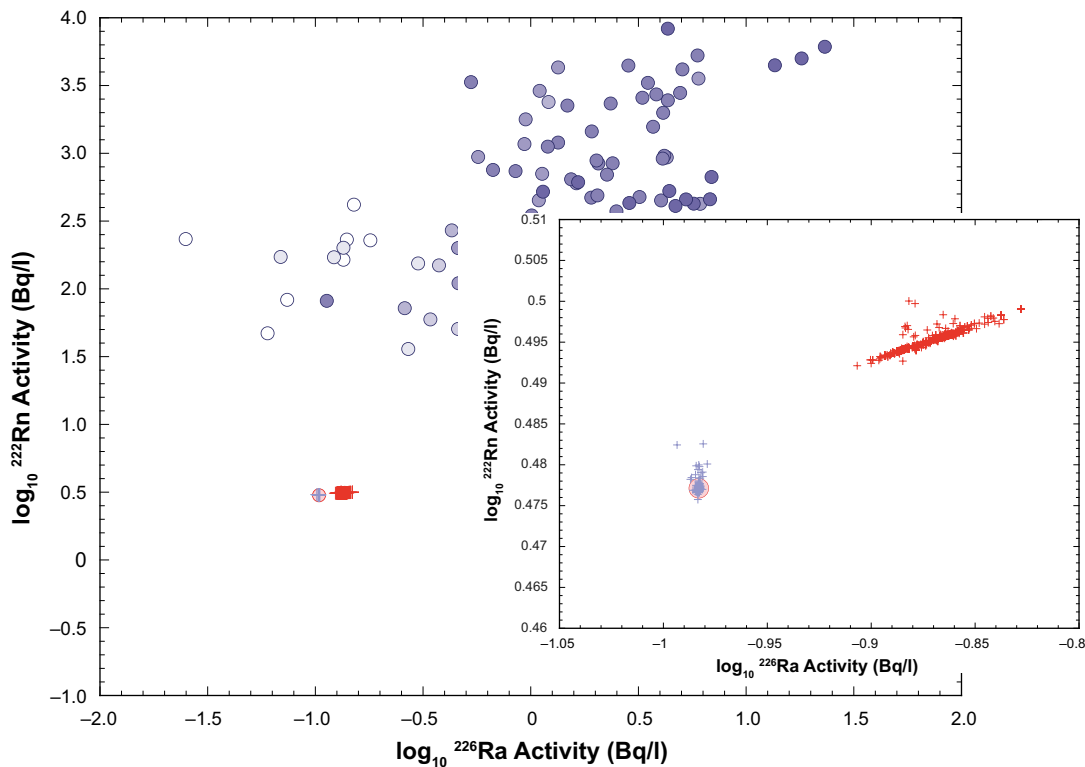
Figure 5-9. *Cross-plot showing measured activities of ²²²Rn and ²²⁶Ra for the REPRO-LTD experiment (red circle marker) with corresponding groundwater measurements made at the Forsmark site for context (blue circular markers). The Forsmark data are shaded proportionally with respect to $\log_{10}$ of groundwater Ca²⁺ concentration with darker shading indicating higher Ca²⁺ concentrations. The light blue "+" symbols indicate 2000 randomly selected simulation results from the MCMC calculations for the abbreviated chain model (M2) exactly overlaying the measurement values calculated at 4.95 y. Red "+" symbols indicate the corresponding results calculated for steady-state conditions.*
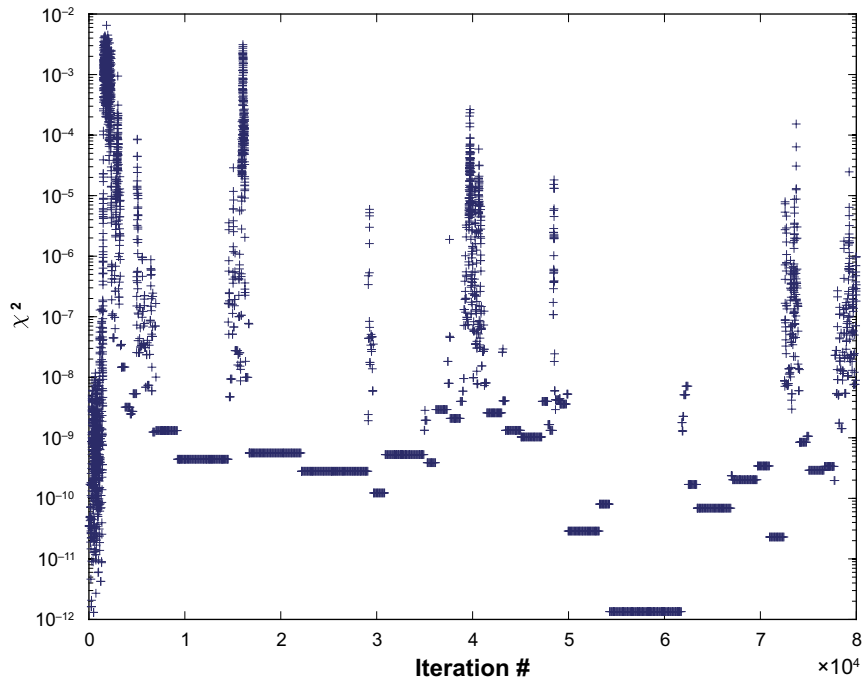
Figure 5-10. *Trace plot showing the calculated sum of squares as a function of iteration number. Although there is no clear burn-in for the sum of squares error, the first 3×10^4 realisations were discarded anyway leaving 5×10^4 realisations from which the posterior uncertainty distributions were calculated.*
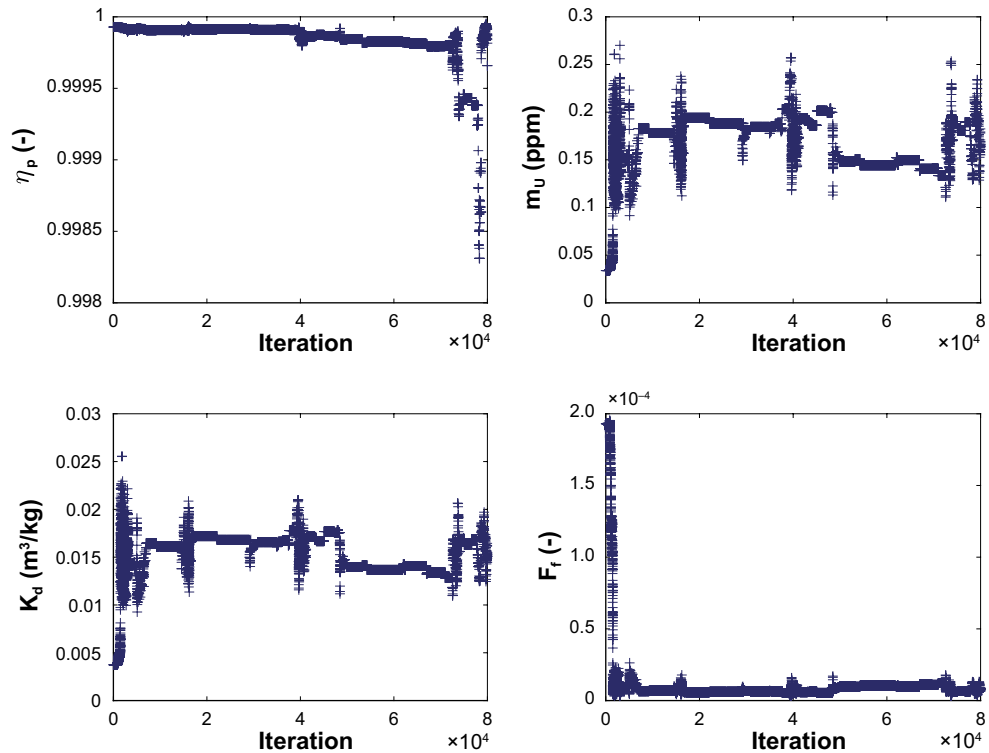
Figure 5-11. *Trace plot showing sampled parameter values as a function of iteration number. The first 3×10^4 realisations were discarded from the calculated chain leaving 5×10^4 realisations from which the posterior uncertainty distributions were calculated.*
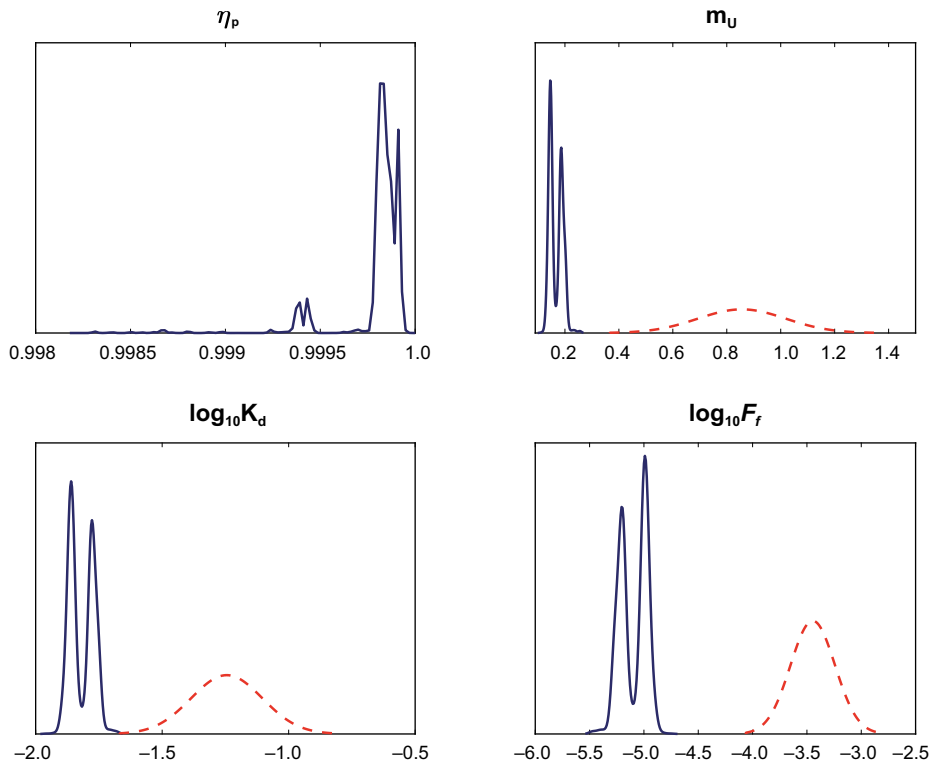
Figure 5-12. *Plot showing posterior probability densities (blue curves) calculated for 5×10^4 MCMC realisations of η_p, m_U, $\log_{10}K_d$, and $\log_{10}F_f$ after discarding the first 3×10^4 realisations as burn in. Results are smoothed using a Gaussian filter with a bandwidth of 2. To aid interpretation, the η_p and m_U parameters have been inverted from their transformed values used in the MCMC calculation and correspond to their arithmetic values. For $\log_{10}K_d$, and $\log_{10}F_f$ the prior Gaussian uncertainty distribution is also plotted (red broken curves).*
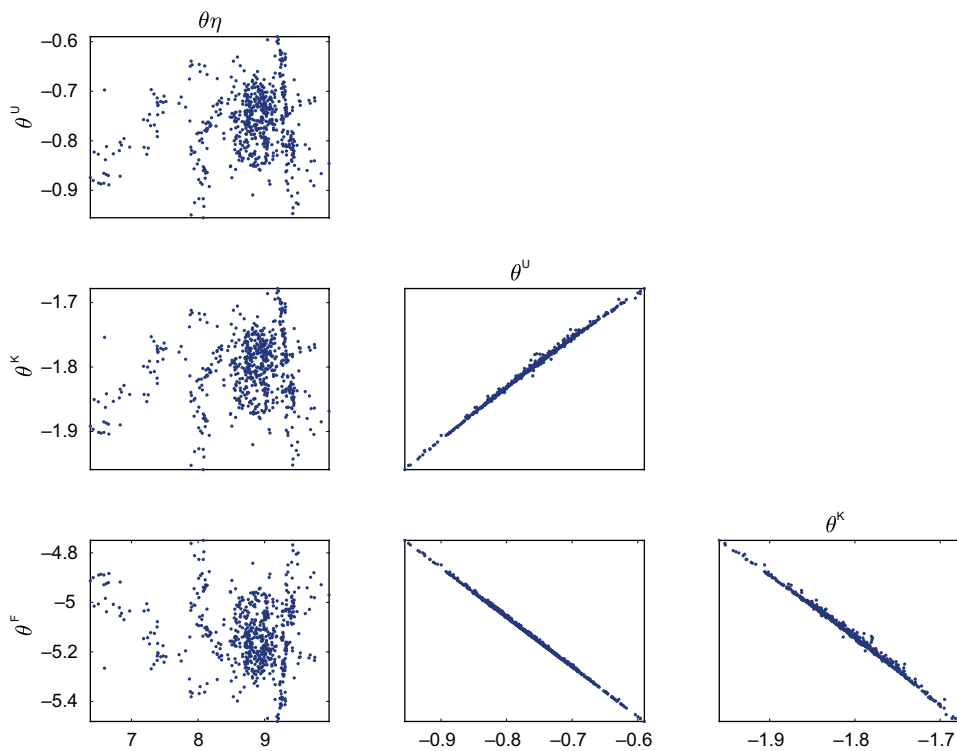
Figure 5-13. *Plot showing pairwise covariance of posterior model parameter estimates. While θ_U, θ_K, and θ_F exhibit relatively strong mutual correlations, there is no apparent mutual correlation between θ_η and θ_U, or θ_η and the other fitted parameters.*
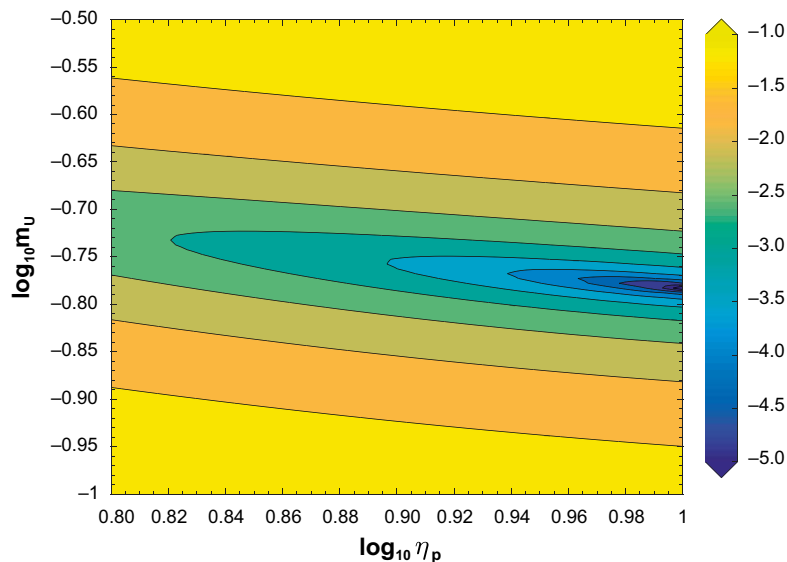
Figure 5-14. *Plot showing the sum-of-squares cost function (χ2) for systematically varied m_U (ppm) and η_p assuming $log_{10}K_d$ and $log_{10}F_f$ set to their best estimate values (θ_K and θ_F) from Table 5-5. There is at least one optimal parameter combination for the abbreviated decay chain model (M2) in the immediate vicinity of $\eta_p >> 1$ and $m_U >> 0.17$ ppm as identified by the MCMC calculation tool.*

5.2.3   Comparison of non-steady state solutions and conclusions

If the non-steady state solutions are compared side-by-side as in Figure 5-15 there is essentially no difference between the models. It should be noted, however, that the meaning of η_p as an effective recoil capture parameter is context specific and differs between the M1 and M2 model variants. The simulation results shown in Figure 5-15 assume parameter values corresponding to the mean of the MCMC chain. Since the parameters comprising the MCMC chain have not converged to a "proper" multivariate Gaussian distribution in the scoping calculations, the naïve mean of the sampled chain does not necessarily give an accurate representation of the best estimate trajectory of time dependent specific activity development in the monitored borehole section. A 95 % credible interval based on random sampling of the chain can be readily calculated, however, and the mean or median trajectory can be estimated from the ensemble of predictions as shown in Figure 5-16.

As can be readily appreciated from the time scales associated with the ingrowth of activity in the borehole section, additional activity measurements made after 1-3 days, 1 week, and perhaps a month would give the data far greater constraining power. This is mostly important for [226]Ra, however, as the [222]Rn levels tend to plateau after about a week, after which any long-term changes would be barely perceptible against the background measurement error.

In the initial scoping calculations documented in this work, the posterior uncertainty distributions calculated for sorptivity (K_d) and the geometric formation factor (F_f) were found to have lower central estimates relative to the prior distributions assigned from independent laboratory measurement data described in the Task Description. For K_d the posterior mean was estimated to be 4-5 times lower than the prior mean, while for F_f the posterior was 20-50 times lower (see Table 5-6). Although this agrees with expectations based on known biases in the estimation of these parameters in the laboratory, it is unclear whether the effect should be so large in the immediate vicinity of the borehole. The average depth of rock matrix from which an emanating radionuclide will reach the borehole surface is calculated in Table 5-6 using the previously given relation (Equation 5-1). The average escape depth calculated using the lab-estimated parameter values are roughly 7 mm and 10 mm for [222]Rn and [226]Ra, respectively. From the posterior central estimates of K_d and F_f, however, the corresponding escape depths are 1.4 mm and 5 mm for the full decay chain (M1) model, and on the order of 1 mm and 3 mm for the abbreviated decay chain (M2) model. Although an effectively unbounded rock matrix is assumed in the calculations presented here, the actual depth of rock matrix beyond which the presence of a diffusion boundary would influence the results is approximately three times the average escape depth (Crawford and Löfgren 2019).
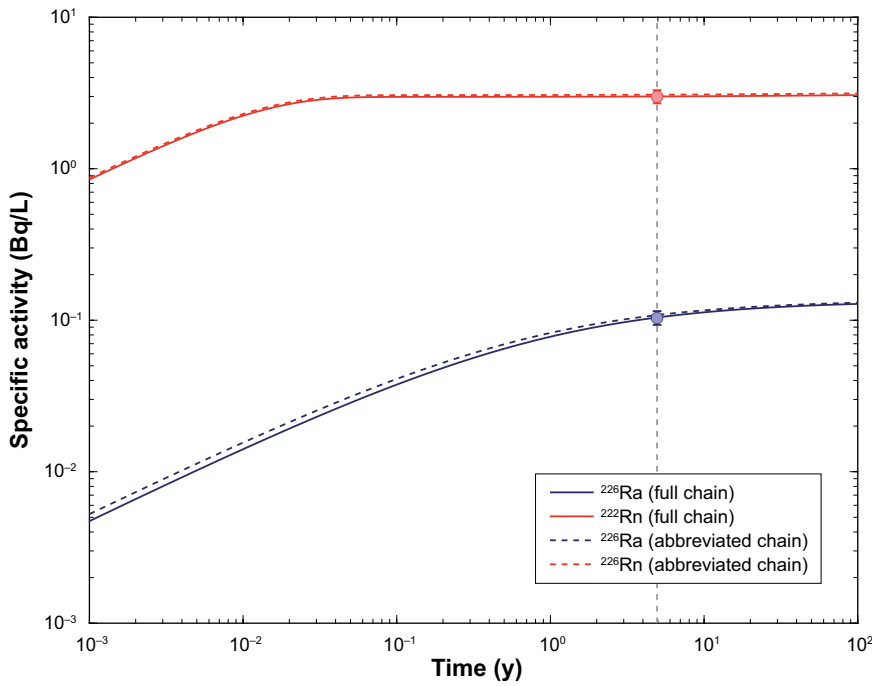
Figure 5-15. *Plot showing the development of borehole specific activity (Bq/l) as a function of time calculated using the full decay chain (M1) and abbreviated decay chain (M2) models assuming parameter values equal to the mean of the MCMC chain. The measured specific activities after a contact time of 4.95 y are shown as circular markers with 1-σ error bars based on the reported measurement error. Both the full decay chain and abbreviated decay chain models give very similar results.*
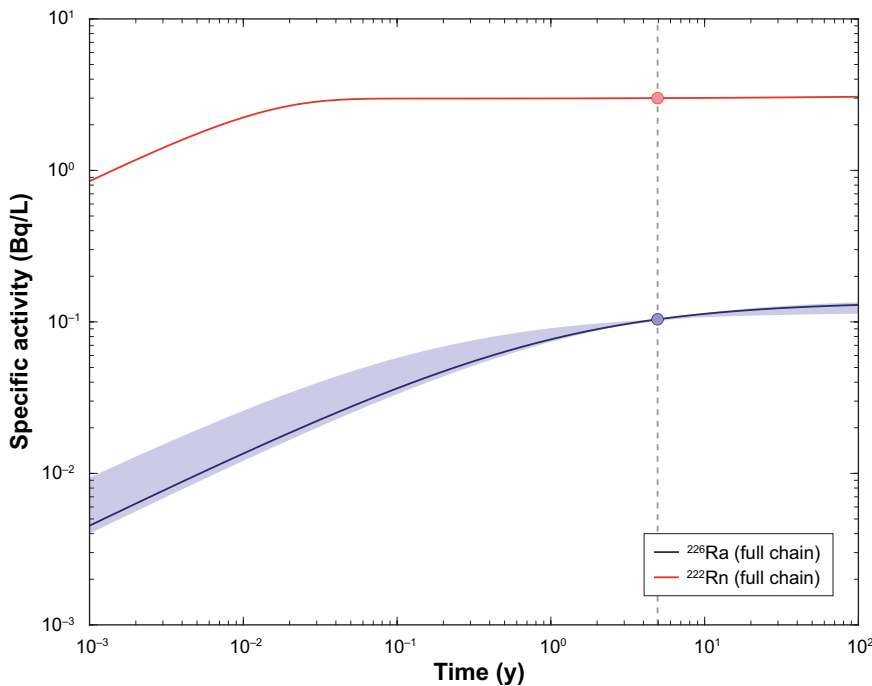
Figure 5-16. *Plot showing the development of borehole specific activity (Bq/l) as a function of time calculated using the full decay chain (M1) model. 95 % credibility intervals are shown (shaded regions) based on random sampling (104 samples) of the MCMC chain (details only visible for ^{226}Ra). The fully drawn curves show the median of calculated specific activity ensemble at each modelled time point. The modelled specific activities after a contact time of 4.95 y (median parameterisation case) are shown as circular markers.*

Table 5-6. Comparison of prior and posterior parameter estimates for natural radionuclide accumulation in the REPRO-TDE borehole section ONK-PP327.

Parameter	Prior	Posterior-M1	Posterior-M2
η_p (%)	0 %–100 %	36.4 ± 0.1	99.98 ± 0.02
m_U (ppm)	7.7 ± 3.0	0.19 ± 0.07	0.17 ± 0.02
K_d (m³/kg)	$(6.0 \pm 2.0) \times 10^{-2}$	$(1.23 \pm 0.31) \times 10^{-2}$	$(1.53 \pm 0.17) \times 10^{-2}$
F_f (−)	$(4.0 \pm 2.0) \times 10^{-4}$	$(1.84 \pm 2.5) \times 10^{-5}$	$(8.3 \pm 2.3) \times 10^{-6}$
δ_m (mm), ^{226}Ra	10.3	4.90	2.95
δ_m (mm), ^{222}Rn	6.56	1.41	0.95

A much more interesting result in the present context is, however, that the posterior estimate for the U-content is roughly 40-45 times less than the bulk average for the rock type based on whole rock geochemistry analyses. The effective recoil capture fraction estimated in both models is also unexpectedly high, ranging between 36 % for the full decay chain model and ~ 100 % for the abbreviated decay chain model. Although it is recognised that the description of emanation is simplified by not considering recoil implantation and secondary return fluxes affecting the mass balance in the porewater, the coupling of the mass balances for ^{226}Ra and ^{222}Rn place a relatively non-linear constraint on the feasible values that η_p can have in the model. This is the case for η_p values greater than about say, 10 % where the mass balance correction given in Table 5-1 starts to become non-negligible. For very low values of η_p, on the other hand, one would expect the production rate of both nuclides to be roughly proportional to the product of η_p and m_U meaning that varying one, or the other parameter should give the same result provided their product is constant. Given the inverse correlation implied by the above, it is not clear why the MCMC model appears to favour simultaneously low uranium content, m_U and relatively high recoil capture fractions, η_p so consistently in the present calculations. This remains a curious result that will need to be investigated more fully to rule out modelling bias.

Although neither of the models are competent to say anything specific about the physical state of U-bearing mineral grains in the rock matrix, very high recoil capture fractions can only realistically occur if the grain size is exceptionally small. It cannot be ruled out, however, that estimated recoil capture fractions based on a simplified description of emanation gives an inaccurate account of the true physical situation. For a 36 % recoil capture fraction, the average grain diameter must be less than 100 nm while for a 100 % recoil capture fraction, the grain size must be less than the recoil stopping distance in the mineral crystal and thus no larger than about 20 nm (assuming UO_2 mineralogy). While micro-precipitates of UO_2 and other secondary U-bearing minerals hosted in grain boundary porosity and microfractures are likely to be in this size range, primary U-bearing minerals found as inclusions in the rock (e.g., zircons, alanite, uranothorite, etc.) are typically far larger (i.e., 1-100 μm).

The very low posterior U-content predicted by both models could, in principle, be the result of larger and volumetrically dominant U-bearing minerals comprising the bulk of the U-content of the rock not being accessible to porewater. The main source of ^{226}Ra and ^{222}Rn would then be mobile radioelements in the porewater and secondary mineralisation hosted in the connected transport porosity, although at much lower levels than would be estimated from the bulk geochemistry. Another possibility is that there is some kind of geochemical disturbance in the first few mm to cm of the rock matrix that is at odds with the assumption of uniform initial conditions in the transient model equal to the expected steady state for the deep rock matrix. The failure of the present version of the transport model to account for loss of progeny nuclides by porewater α-recoil may also be something that needs to be considered further. It is worthwhile noting that the transport model used in this work generally can reproduce approximately the same ranges (order of magnitude) of ^{226}Ra and ^{222}Rn activity measured in fracture water using the prior material property estimates given in Table 5-2 and Table 5-3 assuming recoil capture fractions in the range 1 %–50 % without any further parameter adjustment or optimisation. This implies that there may be a difference in the distribution or accessibility of U-bearing minerals in close proximity to fracture surfaces relative to the deeper rock matrix as studied in this work.

6 Conclusions

6.1 Comparison

6.1.1 Radium measurements in groundwaters in natural fractures

The laboratory measurements of radon/radium are summarized in Table 6-1. One can see clear relationship between Ca concentrations in the groundwater versus the Ra concentrations. This can be mechanistically explained from a cation exchange competition where high calcium concentration causes release of Ra from the rock matrix. Hence one can see concentrations of 113 Bq/l ^{226}Ra in fracture groundwater with 9190 mg/l of Ca while waters containing only 280 mg/l of Ca give only 0.63 Bq/l ^{226}Ra.

Comparison between the groundwaters from natural fractures and the TDE experimental groundwater shows that groundwaters from the artificial 1 mm slit have significantly lower Ra concentrations than natural fracture groundwaters. One could speculate that this is due to the age of the rock-water contact situation, i.e., that the natural fracture situation has had much more time to obtain the natural steady-state situation with higher radium concentrations. However, the results of the modelling efforts indicate that 2 month of contact time should be sufficient for obtaining the maxim radium concentrations, hence the borehole annulus (synthetic fracture) should have obtained steady-state conditions in the experiment. It might be worth mentioning that the physical aperture in the section is about half the effective mass-balance aperture. The mass-balance aperture is given by the circulating water volume (3.13×10^{-4} m^3) divided by the diffusive surface area of the rock (0.178 m^2), which gives 1.76 mm. This is important for Rn although not so much for Ra.

6.1.2 Radon measurements in groundwaters in natural fractures

The radon concentrations in the different groundwaters vary significantly and cannot be correlated to either depth, radium concentrations in water and/or calcium concentrations. One can compare the extremes in the two situations in e.g. OL KR44 766–780 m where 84 % of the radon can originate from radium decay in the fracture groundwater and the ONK-KR15 75.0–75.2 m where < 1 % of the radon can originate from radium dissolved in the groundwater and therefore mainly must originate from radon diffusion from the rock matrix.

The radon concentrations in the synthetic borehole 1 mm slit width are also significantly lower than any radon concentration found in groundwater from natural fractures; ~3 Bq/l in the synthetic borehole compared to 74–396 Bq/l in water from natural fractures. Hence, one can conclude that there must be a mechanistic difference in the radon/radium production and diffusion in rock close to natural fractures compared to the rock matrix studied in the TDE experiment.

Table 6-1. Results of the experimentally obtained radium and radon concentrations in some selected natural fractures in ONKALO combined with the concentrations measured in the TDE observation boreholes ONK-PP324 and ONK-PP327 (1 mm slit).

Sampling site	^{222}Rn Activity (Bq/l)	^{226}Ra Activity (Bq/l)	[Ca] mg/l
ONK-KR15 75.0–75.2 m	396 ± 3	3.8 ± 0.3	1030
OL-KR13 405.5–414.5 m	74 ± 3	2.5 ± 0.3	850
OL-KR11 411–430 m	87 ± 3	0.6 ± 0.2	280
OL-KR45 606–610 m	83 ± 3	10.4 ± 0.4	2710
OL-KR44 766–780 m	144 ± 3	113.1 ± 1.0	9190
ONK-PP324/3.3.2020 1.	2.9 ± 0.3	0.120 ± 0.013	493
ONK-PP324/3.3.2020 2.	3.7 ± 0.3	0.082 ± 0.011	493
ONK-PP327	3.0 ± 0.3	0.104 ± 0.011	493

6.1.3 Comparison of modelling results to the experimental results

In Table 6-2, the experimental results of the TDE observation experiment boreholes are compared to the modelling results presented in Chapter 3. One can summarize that both modelling works overestimate the radon and radium concentrations in the experimental sections, for radon the most pronounced difference is with the measured concentration is 2.9–3.7 Bq/l to the modelled 900–1 200 Bq/l. while for the radium the measured concentrations is in the range of 0.08–0.12 compared to the modelled estimation of 0.12–4.5 Bq/l.

One can compare the modelled results to the concentration found in natural fractures and then one comes closer to the modelled estimations; using natural fracture water the radon concentrations can be up to 400 Bq/l. Radium activities varies a lot, with concentrations up to 113 Bq/l found in extremely calcium rich groundwater, but normally in the range of 0.6–10 Bq/l for most fractures.

One can see from this that the modelling attempts seem to capture the steady state conditions for radium and radon distributions in natural fractures but can be less successfully be used for the prediction of radon and radium mobility in the matrix rock. This is a bit unsatisfactory since the diffusion models used were developed to investigate matrix transport.

Table 6-2. Comparison of model parameters and experimental results from TDE observation boreholes.

Entity	Amphos 21	KTH Neretnieks/Moreno	Experimental results
Porosity	0.03 (BDZ), 0.006 (matrix)	0.007	
Diffusivity	D_e = 3E−13 m²/s (BDZ), 3.6E−14 m²/s (matrix)	D_p(Ra) = 2.9E−11 m²/s , D_e = 2.0E−13 m²/s D_p(Rn) = 6.1E−11 m²/s D_e = 4.3E−13 m²/s	
K_d ^{226}Ra	0.02 m³/kg	0.07 m³/kg	
Emanation factor	1	0.01–1	
BDZ thickness (mm)	21.75	None	
[^{226}Ra] at steady state	4.5 Bq/l	0.12–1.2 Bq/l	0.082–0.12 Bq/l
[^{222}Rn] at steady state	1 000 Bq/l	900–1 200 Bq/l	2.9–3.7 Bq/l

6.1.4 Comparisons of laboratory experiments to field data

It is also of interest to compare these findings to relevant laboratory experiments, i.e., studies of radon concentrations in through-diffusion-experiment cells (Byegård et al. 2002). These consist of measurement of radon concentrations in through-diffusion cells intended for application in diffusivity determinations. These experiments were targeted towards Äspö Hard Rock Laboratory conditions; the major part of samples were from the major rock types Äspö Diorite and Fine Grained Granite, but they were also combined with rock materials sampled from natural fractures.

Given the measurement of the steady state concentrations in the diffusion cells (see results in Table 6-3) and transforming them to a 1-mm-slit conditions one would obtain a concentration conceptually corresponding to the TDE experiment. In this case, one would, for the Fine Grained Granite (3.8 ppm of U), get Rn concentrations in the range of 70–220 Bq/l. On the other hand, for Äspö Diorite (2.6 ppm U), a 1 mm slit borehole gives significantly lower Rn concentration, 6–16 Bq/l. Nevertheless, both of these are higher than the actual ONKALO conditions with ~3 Bq/l from a rock with a measured uranium concentration 7.3 ppm. It is hence an interesting observation that different rock types result in different Rn concentrations which are not to any extent explained by their uranium contents.

An even more striking difference is however the difference in all these radon flux experiments versus the concentrations of radon in the natural fractures. If one for simplicity assumes a natural fracture aperture of 1 mm, it is impossible to match the results from water in contact with rock matrix to the waters in natural fractures. A possibility for this difference could be that rock material close to a natural fracture has a naturally higher content of uranium and uranium daughter-nuclides which causes increased radon fluxes from the matrix to the groundwater. Alternatively, the general rock properties could differ, e.g., different porosity, diffusivity, smaller grain sizes, all giving increased mobility of the radon in the rock phase giving increased radon concentrations in the water phase.

In Byegård et al. (2002), investigations of the radon flux from altered rock material closest to the water-conducting fractures were addressed by studying a mylonite/altered rock material from the particular fracture studied in the TRUE-1 experiment. Water from this fracture was found to contain 400 Bq/l of ^{222}Rn. This was however in clear contrast to the results from the studies of the radon flux from the corresponding fracture rock used in laboratory through-diffusion cells. In the case of a fracture width of a 1 mm fracture, it would correspond to a radon concentration < 11 Bq/l.

Table 6-3. Results from radon flux experiments (Byegård et al. 2002) using intact rock surface material from Äspö Hard Rock Laboratory in Sweden.

Rock type	Measured ^{222}Rn concentration in diffusion cell (Bq/l)	Steady state ^{222}Rn concentration presuming a 1 mm fracture aperture (Bq/l)
Fine Grained Granite (3.8 ppm U)	3–11	70–220
Äspö Diorite (2.6 ppm U)	0.3–07	6–16
Altered fracture surface, mylonite (5.0 ppm U)	< 0.098	< 11

Besides the previous mentioned experiments, radon flux measurements were also performed on naturally unconsolidated fracture filling materials (gouge material) from different Äspö Hard Rock Laboratory locations, however not from the above mentioned TRUE-1 experiment locations (Table 6-4). In this experiment, ~1.5 g of the < 0.063 mm size fraction was isolated and contacted with ~5ml synthetic groundwater in a small test tube. Materials from three different locations with three quite different uranium concentrations (6, 9 and 21 ppm) were studied and the results gave radon concentrations in the samples corresponding to the 20–36 % of the uranium activity. One can calculate from this estimate that to reach a radon activity of 400 Bq/l, one would need to have one litre of water in radon flux equilibrium with 10 kg of fault gouge material (calculated using the most radon producing fault gouge material, i.e., in a sample obtained from borehole KAS04 where it intersects zone EW-1 at 65 m depth, with Rn production of 40 Bq/kg). With an estimation of a rock density of 2 700 kg/m^3, this ratio would correspond to a fracture filling of a fault gouge/groundwater corresponding to a 27 % volume porosity. It is somewhat questionable that a such a fault gouge rich facture could be as conductive as Feature A has proven to be. It is thus, based on the present observations, unlikely that a significant part of the radon in the fracture groundwater is caused by direct interaction with fracture filling material, at least based upon the radon flow measured on the material involved in this investigation.

Table 6-4. Result from radon-flux experiments from fracture filling material.

Rock material	^{222}Rn amount released from the from the fault gouge material	Release factor (presumed a ^{226}Ra equilibrium with ^{238}U)
KI0025F 194 m (6.2 ppm U)	10 ± 3	0.20 ± 0.05
1303 NE-1 (8.9 ppm U)	17 ± 3	0.23 ± 0.04
KAS 04 65m EW-1 (21 ppm U)	41 ± 5	0.35 ± 0.04

The final outcome of the comparisons with radon flux in rock, based on diffusion calculation predictions and laboratory radon flux experiments, does therefore give the following:

a) The use of uranium concentration, a Fickian diffusion model and release factor from the alpha decay daughter around 0.1 to 1 combined with a fracture aperture of 1 mm gives ^{222}Rn concentrations about 900–1 200 Bq/l, a range which to some extent has been found in natural fractures, e.g. ONK-KR 15 and Feature A in Äspö Hard Rock Laboratory (about 400 Bq/l).

b) The synthetically produced 1-mm slit of the TDE boreholes in ONKALO do however only produce ~3Bq/l of steady state concentration of radon., i.e., significantly lower than any of the fracture groundwaters and lower than the predictions made using the diffusion models.

c) The laboratory experiments of radon flux give magnitudes closer to the range of the TDE borehole (synthetic fracture) situation but not to any extent close to the high concentrations found in fracture groundwaters.

The general final outcome is thus that the diffusion models used for the transport between the TDE boreholes cannot in their present form match the measured radon transport characteristics. One can, however, observe a closer match between the field experiment of the TDE synthetic boreholes with the laboratory experiments of radon flux. In Crawford (2010), it was stated that the probability distribution of predicted ^{222}Rn and ^{226}Ra activities made using a model including diffusion and sorption agreed reasonably well with the measurement data when assuming a K_d for rock matrix sorption of roughly the same magnitude as that recommended for transport modelling. However, in the present stage, the outcome of the TDE diffusion experiment cannot be used as a bridge in the process of identifying the observed radon and radium concentration in the groundwater as a supporting proof for a matrix diffusion mechanism occurring in a natural groundwater.

For obtaining a conceptual match of the observations made in this piece of work, it is necessary to set up a concept of a source of radon flux being present close to natural fractures compared to intact matrix rock. This source then would have to be far more pronounced than in the intact matrix rock in order to explain the much higher radon and radium concentrations in the fracture groundwater compared to the concentrations in the pore matrix fluids (here represented by the TDE Slit groundwater). Possible explanations to this deviation could be:

• Increased concentrations of uranium (or any other of the element in the uranium decay series) close the fractures compared to the matrix rock. This could be caused by:

- Naturally increased uranium concentrations in rock close to the fractures (e.g., fracture fillings and/or rim zone material).

- Diffusion of a species within the uranium series causing an increase of a radon/radium parent radionuclide into the rock closest to the fractures.

• Closer to the fractures, uranium would be present in rock material grains that could be characterized with the uranium deposited in surfaces closer to the pore liquid and hence associated with higher release factors compared to ordinary matrix rock.

• Generally increased diffusion properties in the rock closest to the fractures compared to the ordinary matrix rock.

• Generally lower adsorption properties in the rock closest to the fractures compared to the ordinary matrix rock. Thereby radium and all the parent radionuclides in the fracture rock would have a higher apparent diffusion and more radium and radon would reach the fracture groundwater.

However, according to all these four explanations, one should have observed increased radon concentrations in the laboratory experiments for the radon flux from natural fracture samples. Since the laboratory experiments referred to in this report (however numerically restricted) do not support any of these explanations.

Questions may be raised whether the conditions of transfer of dissolved gasses from pore liquids to bulk water phase (e.g., fracture water and/or borehole water) are difficult to reproduce in laboratory experiment and in in-situ experiments with drilled borehole walls. A concept of a "skin effect" could possibly explain the deviations observed in this report, e.g., lack of high-pressure conditions in the laboratory experiment combined with restricted dissolved gas transfer from synthetically produced rock surfaces. However, this explanation has to the authors knowledge not been confirmed by any experiment, so it is at this stage just a speculation.

As mentioned, one can thus not in the present stage, regard the outcome of the TDE diffusion experiment as a bridge in the process of identifying the observed radon and radium concentration in the groundwater as a supporting proof for a matrix diffusion mechanism occurring in a natural groundwater. It is obvious that there are some mechanisms in the in-situ matrix diffusion of the natural radionuclide tracers radon and radium that cannot solely be reproduced by laboratory data and an ordinary diffusion model.

Regarding the inverse modelling of transport parameters, it can be concluded that it is necessary to invoke a very low production rate of Ra and Rn in the rock matrix to obtain a satisfactory match with the measurement data in the experimental borehole sections. This could imply that the bulk of U-enriched mineral phases are insufficiently accessible to porewater to contribute significantly to Ra and Rn production. The estimated sorptivity (K_d) and pore diffusivity (D_p) of the rock matrix is slightly less than that measured in the laboratory, although not more than what might be expected for in-situ formation conditions. The fitted transport parameters suggest an average depth from which Ra and Rn are released into the borehole of no more than 1–5 mm. Given the estimated proximity of released radionuclides to the borehole outer wall, however, the estimated effective transport properties may not be fully representative of undisturbed rock depending on the extent of the core drill damaged zone. It is not clear whether the results might be explained by limited connectivity of the bulk rock matrix, although this seems unlikely given the results of the tracer experiments performed in the same borehole sections.

A possible confounding factor is the assumption of initially uniform steady-state concentrations in the rock matrix for transient modelling. If the bulk of the out-diffusing Ra (and Rn) originates from porewater associated sources rather than U-enriched accessory minerals, any disturbance of the initial Ra concentration profile in the first few mm of rock matrix might be expected to have a significant impact on the fluxes of Ra and Rn subsequently measured in the borehole. The consequences of this assumption could be tested in further work by using a multilayer rock matrix with differing initial conditions assigned to a disturbed zone to see if this can better replicate the measurements. In any case, the experimental results clearly indicate that the production and transport of natural radionuclides in the undisturbed rock matrix some distance from fracture surfaces is not fully understood at present and further work will need to be done to properly elucidate the transport mechanisms underlying these unexpected results. The closer agreement of results obtained by the modelling groups with typical radionuclide levels in groundwater, however, suggests that the models adequately represent transport processes associated with altered rock surrounding flow-bearing fractures.

Measurement of the ^{226}Ra content of the borehole section-specific rock rather than assuming isotopic equilibrium with an assumed site average ^{238}U content would allow a more accurate account of radio-nuclide production than is achievable at present. Also, if Ra-containing porewater can be "flushed" from a larger core sample using a technique such as through-electromigration with a high salinity background electrolyte, it should be possible to discriminate between mobile ^{226}Ra in the porewater and that bound in accessory minerals residing in the matrix. These two measurements together would go some way towards excluding the previously suggested confounding factor associated with the transient modelling of Ra and Rn emanation.

References

SKB's (Svensk Kärnbränslehantering AB) publications can be found at www.skb.com/publications.

Aaltonen I (ed), Lahti M, Engström J, Mattila J, Paananen M, Paulamäki S, Gehör S, Kärki A, Ahokas T, Torvela T, Front K, 2010. Geological model of the Olkiluoto site – Version 2. Posiva Working Report 2010-70, Posiva Oy, Finland.

Al-Jarallah M I, Fazal-ur-Rehman, Musazay M S, Aksoy A, 2005. Correlation between radon exhalation and radium content in granite samples used as construction material in Saudi Arabia. Radiation Measurements 40, 625–629.

Andersson P, Nilsson K, Löfgren M, 2020. Task description of Task 9C – Modelling of REPRO experiment TDE. Task 9 of SKB Task Force GWFTS – Increasing the realism in solute transport modelling based on the field experiments REPRO and LTDE-SD. SKB P-17-31, Svensk Kärnbränslehantering AB.

André M, Neretnieks I, Malmström M E, 2008. Measuring sorption coefficients and BET surface areas on intact drillcore and crushed granite samples. Radiochimica Acta 96, 673–677.

André M, Malmström M E, Neretnieks I, 2009. Specific surface area determinations on intact drillcores and evaluation of extrapolation methods for rock matrix surfaces. Journal of Contaminant Hydrology 110, 1–8.

Andrews J N, Giles I S, Kay R L F, Lee D J, Osmond J K, Cowart J B, Fritz P, Barker J F, Gale J, 1982. Radioelements, radiogenic helium and age relationships for groundwaters from the granites at Stripa, Sweden. Geochimica et Cosmochimica Acta 46, 1533–1543.

Andrews J N, Davis S N, Fabryka-Martin J, Fontes J-C, Lehmann B E, Loosli H H, Michelot J-L, Moser H, Smith B, Wolf M, 1989a. The *in situ* production of radioisotopes in rock matrices with particular reference to the Stripa granite. Geochimica et Cosmochimica Acta 53, 1803–1815.

Andrews J N, Ford D J, Hussain N, Trivedi D, Youngman M J, 1989b. Natural radioelement solution by circulating groundwaters in the Stripa granite. Geochimica et Cosmochimica Acta 53, 1791–1802.

Baretto P M C, 1971. Radon-222 emanation from rocks, soils, and lunar dust. Master of Arts thesis. Rice University, Texas.

Bossus D A W, 1984. Emanating power and specific surface area. Radiation Protection Dosimetry 7, 73–76.

Bourdon B, Bureau S, Andersen M B, Pili E, Hubert A, 2009. Weathering rates from top to bottom in a carbonate environment. Chemical Geology 258, 275–287.

Byegård J, Ramebäck H, Widestrand H, 2002. Äspö Hard Rock Laboratory. TRUE-1 continuation project. Use of radon concentrations for estimation of fracture apertures – Part 1: Some method developments, preliminary measurements and laboratory experiments. SKB IPR-02-68, Svensk Kärnbränslehantering AB.

Cameron C P, 1987. A review of radon emanation and mobilization in minerals and rocks. Miscellaneous Paper GL-87-27 (AD-A189 764), U.S. Army Corps of Engineers, Washington, DC.

Carbol P, Engkvist I, 1997. Compilation of radionuclide sorption coefficients for performance assessment. SKB R-97-13, Svensk Kärnbränslehantering AB .

Cartwright J, 1962. Particle shape factors. The Annals of Occupational Hygiene 5, 163–171.

Crawford J, 2010. Bedrock K_d data and uncertainty assessment for application in SR-Site geosphere transport calculations. SKB R-10-48, Svensk Kärnbränslehantering AB.

Crawford J, Löfgren M, 2019. Modelling of radionuclide retention by matrix diffusion in a layered rock model. SKB R-17-22, Svensk Kärnbränslehantering AB.

CRC, 2000. Ionic conductivity and diffusion at infinite dilution. In Lide D R (ed). CRC Handbook of chemistry and physics. 81st ed. Boca Raton, FL: CRC Press.

Currie L A, 1968. Limits for qualitative detection and quantitative determination. Application to radiochemistry. Analytical Chemistry 40, 586–593.

Davidson-Pilon C, 2015. Bayesian methods for hackers: probabilistic programming and Bayesian inference. New York: Addison-Wesley.

de Hoog F R, Knight J H, Stokes A N, 1982. An improved method for numerical inversion of Laplace transforms. SIAM Journal on Scientific and Statistical Computing 3, 357–366.

Diego-Feliu M, Rodellas V, Saaltink M W, Alorda-Kleinglass A, Goyetche T, Martínez-Pérez L, Folch A, Garcia-Orellana J, 2021. New perspectives on the use of ^{224}Ra/^{228}Ra and ^{222}Rn/^{226}Ra activity ratios in groundwater studies. Journal of Hydrology 596. doi:10.1016/j.jhydrol.2021.126043

Dongara J, Sullivan F, 2000. Guest Editors Introduction to the top 10 algorithms. Computing in Science & Engineering 2, 22–23.

Drake H, Sandström B, Tullborg E-L, 2006. Mineralogy and geochemistry of rocks and fracture fillings from Forsmark and Oskarshamn: Compilation of data for SR-Can. SKB R-06-109, Svensk Kärnbränslehantering AB.

Eggeling L, Genter A, Kölbel T, Münch W, 2013. Impact of natural radionuclides on geothermal exploitation in the Upper Rhine Graben. Geothermics 47, 80–88.

Fleischer R, 1983. Theory of alpha recoil effects on radon release and isotopic disequilibrium. Geochimica et Cosmochimica Acta 47, 779–784.

Flügge S, Zimens K, 1939. Die Bestimmung von Korngrößen und von Diffusionskonstanten aus dem Emaniervermögen. Zeitschrift für Physikalische Chemie 42B, 179–220. (In German.)

Gelfand A E, 2000. Gibbs sampling. Journal of the American Statistical Association 95, 1300–1304.

Gelman A, Carlin J B, Stern H S, Rubin D B, 2003. Bayesian data analysis. 2nd ed. Boca Raton, FL: Chapman & Hall/CRC Press.

Geyer C J, 2011. Introduction to Markov chain Monte Carlo. In Brooks S, Gelman A, Jones G L, Meng X-L (eds). Handbook of Markov chain Monte Carlo. Boca Raton, FL: Chapman & Hall/CRC, 3–48.

Girault F, Perrier F, Przylibski T A, 2018. Radon-222 and radium-226 occurrence in water: a review. In Gillmore G K, Perrier F E, Crockett R G M (eds). Radon, health and natural hazards. Bath: The Geological Society. (Geological Society London Special Publication 451), 131–154.

Haario H, Saksman E, Tamminen J, 2001. An adaptive Metropolis algorithm. Bernoulli, 7, 223–242.

Haario H, Laine M, Mira A, Saksman E, 2006. DRAM: Efficient adaptive MCMC. Statistics and Computing 16, 339–354.

Hassan N M, Hosoda M, Ishikawa T, Sorimachi A, Sahoo S K, Tokonami S, Fukushi M, 2009. Radon migration process and its influence factors; review. Japanese Journal of Health Physics 44, 218–231.

Hastings W K, 1970. Monte Carlo sampling methods using Markov chains and their applications. Biometrika 57, 97–109.

Hollenbeck K J, 1998. INVLAP.M: A matlab function for numerical inversion of Laplace transforms by the de Hoog algorithm. Department of Hydrodynamics and Water Resources (ISVA), Technical University of Denmark, Lyngby, Denmark. Available at: https://web.archive.org/web/20030514065058/http://www.isva.dtu.dk/staff/karl/invlap.htm

Jelinek C, Eliasson T, 2015. Strålning från bergmaterial. SGU-rapport 2015:34, Geological Survey of Sweden. (In Swedish.)

Jia G, Jia J, 2012. Determination of radium isotopes in environmental samples by gamma spectrometry, liquid scintillation counting and alpha spectrometry: a review of analytical methodology. Journal of Environmental Radioactivity 106, 98–119.

Key R M, Guinasso N L, Schink D R, 1979. Emanation of radon-222 from marine sediments. Marine Chemistry 7, 221–250.

Kigoshi K, 1971. Alpha-recoil thorium-234: Dissolution into water and the uranium 234/uranium 238 disequilibrium in nature. Science 173, 47–48.

Kornelsen E V, 1964. The ionic entrapment and thermal desorption of inert gases in tungsten for kinetic energies of 40 eV to 5 keV. Canadian Journal of Physics 42, 364–381.

Krall L, Sandström B, Tullborg E-L, Evins L, 2015. Natural uranium in Forsmark, Sweden: The solid phase. Applied Geochemistry 59, 178–188.

Laine M, 2018. MCMC toolbox for Matlab. Available at: https://mjlaine.github.io/mcmcstat/

Langmuir D, 1997. Aqueous environmental geochemistry. Upper Sadle River, NJ: Prentice Hall.

Lee V E, DePaolo D J, Christensen J N, 2010. Uranium-series comminution ages of continental sediments: Case study of a Pleistocene alluvial fan. Earth and Planetary Science Letters 296, 244–254.

Liu J, Neretnieks I, 1994. Some evidence of radiolysis in a uranium ore body – Quantification and interpretation. In Murakami T, Ewing R (eds). Scientific basis for nuclear waste management XVIII: symposium held in Kyoto, Japan, 23–27 October 1994. Pittsburgh, PA: Materials Research Society. (Materials Research Society Symposium Proceedings 353), 1179–1186.

Liu J, Neretnieks I, 1996. A model for radiation energy deposition in natural uranium-bearing systems and its consequence to water radiolysis. Journal of Nuclear Materials 231, 103–112.

Mahmoudzadeh B, Liu L, Moreno L, Neretnieks I, 2014. Solute transport in a single fracture involving an arbitrary length decay chain with rock matrix comprising different geological layers. Journal of Contaminant Hydrology 164, 59–71.

Mauerhofer E, Zhernosekov K, Rösch F, 2004. Limiting transport properties and hydration numbers of actinyl ions in pure water. Radiochimica Acta 92, 5–10.

Metropolis N, Rosenbluth A W, Rosenbluth M N, Teller A H, Teller E, 1953. Equation of state calculations by fast computing machines. The Journal of Chemical Physics 21, 1087–1092.

Nayar K G, Sharqawy M H, Banchik L D, Lienhard J H, 2016. Thermophysical properties of seawater: A review and new correlations that include pressure dependence. Desalination 390, 1–24.

Neretnieks I, 2013. Some aspects of release and transport of gases in deep granitic rocks: possible implications for nuclear waste repositories. Hydrogeology Journal 21, 1701–1716.

Nicolas A, Girault F, Schubnel A, Pili É, Passelègue F, Fortin J, Deldicque D, 2014. Radon emanation from brittle fracturing in granites under upper crustal conditions. Geophysical Research Letters 41, 5436–5443.

Pereira A, Lamas R, Miranda M, Domingos F, Neves L, Ferreira N, Costa L, 2017. Estimation of the radon production rate in granite rocks and evaluation of the implications for geogenic radon potential maps: A case study in Central Portugal. Journal of Environmental Radioactivity 166, 270–277.

Przylibski T A, 2000. Estimating the radon emanation coefficient from crystalline rocks into groundwater. Applied Radiation and Isotopes 53, 473–479.

Rona E, 1917. Diffusiongrosse and Atomdurchmesser der Radiumemanation. Zeitschrift für Physikalische Chemie 92, 213–218. (In German.)

Roy V, 2020. Convergence diagnostics for Markov chain Monte Carlo. Annual Review of Statistics and Its Application 7, 387–412.

Saarinen L, Suksi J, 1992. Determination of uranium series radionuclides Pa-231 and ^{226}Ra by liquid scintillation counting. Report YJT-92-20, Nuclear Waste Commission of Finnish Power Companies.

Sakoda A, Ishimori Y, Yamaoka K, 2011. A comprehensive review of radon emanation measurements for mineral, rock, soil, mill tailing and fly ash. Applied Radiation and Isotopes 69, 1422–1435.

Salonen L, 1993. Measurement of low levels of ^{222}Rn in water with different commercial liquid scintillation counters and pulse-shape analysis. In Noakes J E, Schönhofer F, Polach H A (eds). Liquid scintillation spectrometry 1992. Tucson, AZ: Radiocarbon, 361–372.

Sandström B, Stephens M, 2009. Mineralogy, geochemistry, porosity and redox properties of rocks from Forsmark. Compilation of data from the regional model volume for SR-Site. SKB R-09-51, Svensk Kärnbränslehantering AB.

Semkow T M, 1990. Recoil-emanation theory applied to radon release from mineral grains. Geochimica et Cosmochimica Acta 54, 425–440.

Semkow T M, 1991. Fractal model of radon emanation from solids. Physical Review Letters 66, 3012–3015.

Sharqawy M H, Lienhard J H, Zubair S M, 2010. Thermophysical properties of seawater: A review of existing correlations and data. Desalination and Water Treatment 16, 354–380.

Soler J M, Kekäläinen P, Pulkkanen V-M, Moreno L, Iraola A, Trinchero P, Hokr M, Říha J, Havlová V, Trpkošová D, Vetešník A, Reimitz D, Višňák J, Vopálka D, Gvoždík L, Milický M, Polák M, Fukatsu Y, Ito T, Tachi Y, Svensson U, Park D K, Ji S-H, Gylling B, Lanyon G W, 2021. Evaluation report of Task 9C based on comparisons and analyses of modelling results for the ONKALO REPRO-TDE experiment. Task 9 of SKB Task Force GWFTS – Increasing the realism in solute transport modelling based on the field experiments REPRO and LTDE-SD. SKB TR-21-09, Svensk Kärnbränslehantering AB.

Speagle J S, 2020. A conceptual introduction to Markov chain Monte Carlo methods. arXiv preprint Physics and Society. Available at: https://arxiv.org/pdf/1909.12313.pdf

Stajic J M, Nikezic D, 2014. Theoretical calculation of radon emanation fraction. Nuclear Instruments and Methods in Physics Research Section B: Beam Interactions with Materials and Atoms 336, 19–25.

Suksi J, Rasilainen K, Pitkänen P, 2006. Variations in ^{234}U/^{238}U activity ratios in groundwater – A key to flow system characterisation? Physics and Chemistry of the Earth 31, 556–571.

Sun H, Furbish D J, 1995. Moisture content effect on radon emanation in porous media. Journal of Contaminant Hydrology 18, 239–255.

Sun H, Semkow T M, 1998. Mobilization of thorium, radium and radon radionuclides in ground water by successive alpha-recoils. Journal of Hydrology 205, 126–136.

Trinchero P, Sidborn M, Puigdomenech I, Iraola A, Bosbach D, Deissmann G, 2019. Groundwater age dating in fractured rock using ^{4}He data. Journal of Hydrology X 4. doi:10.1016/j.hydroa.2019.100036

Usman S S, Spitz H, Weisman J, 2004. Transport of Radon in still water under steady-state and transient conditions. In Proceedings of the 11th International Congress of the International Radiation Protection Association, Madrid, 23–28 May 2004.

van Ravenzwaaij D, Cassey P, Brown S D, 2018. A simple introduction to Markov chain Monte-Carlo sampling. Psychonomic Bulletin & Review 25, 143–154.

Vesterbacka P. 2005. ^{238}U series radionuclides in Finnish groundwater-based drinking water and effective doses. STUK-A213, Radiation and Nuclear safety Authority (STUK), Finland.

Voutilainen A, 1998. Käytetyn ydinpolttoaineen loppusijoituspaikkavaihtoehtojen ympäristön radioaktiiviset aineet ja ionisoiva säteily. Posiva Työraportti 98-63, Posiva Oy, Finland. (In Finnish.)

Yamaguchi T, Nakayama S, 1998. Diffusivity of U, Pu and Am carbonate complexes in a granite from Inada, Ibaraki, Japan studied by through diffusion. Journal of Contaminant Hydrology 35, 55–65.

Task description of Task 9C Extension

SKB Task Force on Modelling of Groundwater Flow and Transport of Solutes

Task 9: Increasing the realism in solute transport modelling – Modelling the field experiments of REPRO and LTDE-SD

Task description – 9C Extension. Radon and radium concentrations in REPRO TDE groundwater as a result of diffusion

Johan Byegård, 2019-07-12

Updates compared to the original Task description are marked with grey:

- Addendum C – Some key differences between radiolysis & emanation, is removed.

- Some editorial modifications are made only to adjust the contents for inclusion in this report.

A1　Background

The Task 9C within the GWFTS Task Force has been focused on the diffusive transport in crystalline rock and the models set up have been aimed towards studying the results of the REPRO Through-Diffusion Experiment (TDE) in ONKALO. This experiment was set up as a through diffusion experiment where a synthetic groundwater and radiotracer cocktail was transferred into one borehole and the diffusive transport studied by tracer breakthrough in the two adjacent boreholes at ~ decimetre distance; one in the foliation direction and one perpendicular to the foliation.

A natural process which is also dependent on the diffusivity in rock is the radon and radium production and transport in natural groundwater. Radon and radium are produced by radioactive decay mainly in the rock matrix and thereafter transported by diffusion out to the groundwater in the fractures. The concentration of these elements in the fracture porewater are therefore favoured by 1) high rock matrix diffusivity 2) long life-time (i.e., half-life) of the radionuclide and 3) high concentration of the parental radionuclides (i.e., the uranium or thorium concentrations). It is therefore obvious that diffusion characteristics applied in the model setup for the TDE diffusion experiment could also be used for the prediction of the radon and radium concentrations in the fracture groundwater.

The present experimental setup in the REPRO TDE experiment (boreholes with a dummy giving a thin and well determined annulus water volume) offers good possibilities of estimating radon and radium fluxes in a rock matrix environment. Showing the capability of predicting and understanding the process of the natural tracers radon and radium in relation to the TDE Experiment with added synthetic tracers will give further justification to the diffusion models applied. The model will, in such case, show its applicability both for through-diffusion processes as well as for the case of production of safety-relevant radionuclides inside the matrix, followed by an out-diffusion.

A2　Subtasks

The following three subtasks can be identified:

1. Blind predictive calculation of the radon and radium concentration in the experimental section of the PP324 and PP327 borehole sections. This should preferentially be done by using the diffusion model that has been set up and calibrated from Task 9C, i.e., the experimental results of diffusion breakthrough in the observation boreholes as well as the tracer lost in the injection borehole due to diffusion and sorption.

2. When experimental results of the radon and radium concentrations are available, calibration of the radium and radon-specific parameters can be done in order to fit the calculated concentrations to the experimentally obtained concentrations.

3. (Possible) Make estimations of what concentrations of radium and radon one should expect (when applying the radium/radon production and diffusion model developed in (2)) in natural fracture groundwater in ONKALO, and thereafter make comparisons to measured concentrations.

A3 Recommendations concerning the data to be used

A3.1 Production process

A3.1.1 Tracer concentration

The radon and radium isotopes that are proposed to be used in this calculation are the ones within the uranium series, this since they are the most long-lived and therefore expected to move longer distances compared e.g. to the isotopes in the Thorium series.

The decay series of Uranium-238, up to the radium and radon isotopes, consists of:

^{238}U (t$_{1/2}$=4.47E9 y) ->

-> ^{234}Th (t$_{1/2}$=24.1 d) ->

-> ^{234}Pa (t$_{1/2}$=1.17 min) ->

-> ^{234}U (t$_{1/2}$=2.45E5 y) ->

-> ^{230}Th (t$_{1/2}$=7.5E4 y) ->

-> ^{226}Ra (t$_{1/2}$=1 600 y) ->

-> ^{222}Rn (t$_{1/2}$=3.82 d)

The amount of radium and radon in the rock is thus dependent on the total concentration of uranium. The measured concentration of uranium C_U (mg/kg) is thus an important input parameter. It seems convenient for this particular case to assume that a full secular equilibrium (same activity of all isotopes in the decay chain) is present at the start of the calculation; i.e., to simplify the problem to a constant and homogeneous concentration of ^{226}Ra, A_{Ra} (Bq/kg) at the start of the experiment. This can be calculated according to:

$$A_{Ra} = \frac{\frac{c_U}{1000}}{238} \cdot N_a \cdot \ln(2)/t_{1/2(U)} \tag{A-1}$$

where N_a is the Avogadro number (6.022×10^{23}), and $t_{1/2}(U)$ is the half-life of ^{238}U expressed in seconds.

Recommendations of uranium concentrations to be used are found in Table A-1. A full data set for uranium measurements in ONKALO is given in Addendum A for modellers who want to study the concentration variation observed. As an example, a few very high values for the uranium concentration in pegmatitic granite can be observed, which is the reason for the high standard deviation.

Table A-1. Uranium concentration in Pegmatitic granite and Veined gneiss. The compilation is based on the total number of measurements which are detailed in Addendum A.

Rock type	U (ppm) all samples	+/-	U (ppm) only ONKALO samples selected	+/-
Pegmatitic granite	8.3	16.5	7.0	3.4
Veined gneiss	6.9	3.7	7.7	3.0

A3.1.2 Release factor

In the model used for calculation of diffusion of daughter products from alpha decay, a release factor is most often applied, which is the measure of the fraction of the produced daughter radionuclide that is deposited in water compared to the fraction that remains locked in mineral grains of the rock matrix after the decay. A theory behind this and attempts to theoretically calculate this factor as a result of an alpha recoil effect have been presented by e.g. Neretnieks (2013), and a compilation of theories and practice from the literature concerning this subject is given in Addendum B.

Some proposed ranges of values for the release factor are shown in Figure A-1 and are based on an estimated relationship between porosity and the release factor. The mechanistic basis for this, however, is complex and might be expected to differ among rocks of different origin and with

microstructural characteristics. From the representation shown in Figure A-1, a value in the range of 1–10 % is roughly estimated. The modelers are however free to make their own choice of release factors to be used for the calculation. Possible alternative sources for the release factor (or alternative concepts for the daughter radionuclide reaching the connected porosity) could be:

- Other literature sources for the release factor.
- Calibrations of the release factor from experimental results and/or from the results of measurements of radon/radium concentrations in ONKALO groundwater.
- Applying a microstructural model (e.g., the one already used in the Task 9C for the through diffusion experiment) with estimations of dead-end porosity and the pore size effect.

A3.1.3   Diffusion rate

The transport rate of the matrix produced radionuclide to the borehole groundwater should be estimated using the same diffusion model as applied in calculations of the REPRO TDE through-diffusion experiment.

A3.1.4   Pore diffusivity

The pore diffusivity of Rn(aq) and Ra^{2+} in the rock type can be estimated by the relation:

$$D_{px} = F_f/e \cdot D_w \quad \text{(A-2)}$$

where the F_f ("formation factor) is obtained from the laboratory experiment determination of the pore diffusivity, e is the porosity and D_w is the tabulated diffusivity of the compound in pure water. The formation factor is usually calculated from the measured effective diffusivity of tritiated water in the rock in comparison to the tabulated free diffusivity of water in water, according to:

$$F_f = D_{e(HTO)}/D_{w(HTO)} \quad \text{(A-3)}$$

Or, can also be directly obtained from the electrical resistivity measurements.

Diffusivity of Rn in pure water are reported by Usman et al. (2004) to be in the range of 1.14×10^{-9} to 1.56×10^{-9} m^2/s. The corresponding diffusivity of Ra^{2+} has been estimated to be in the range of 4.02×10^{-10} to 8.89×10^{-10} m^2/s.
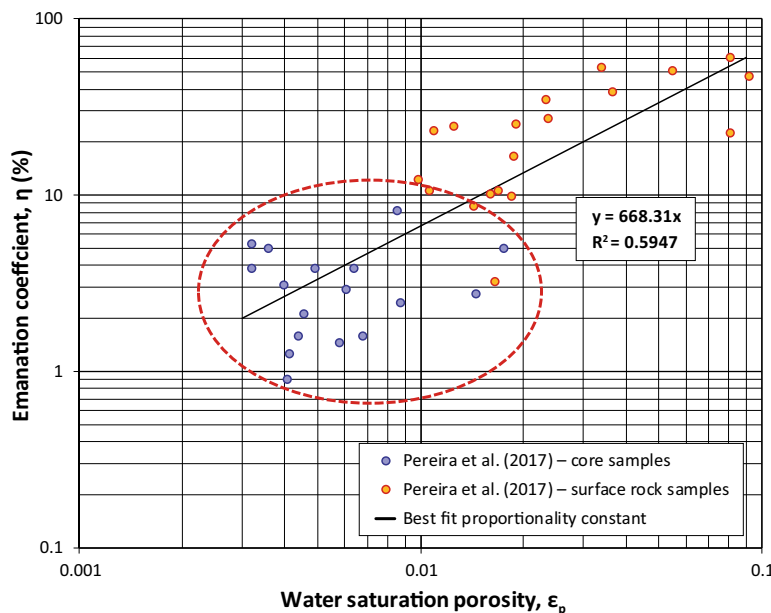
Figure A-1. Experimentally determined release factors as a function of the water saturation porosity, from Pereira et al. (2017) (details in Addendum B). A rough selection has here been made when selecting porosities < 1 % which correspond to a release factor interval of 1–10 %.

A3.1.5 Sorption

Since radon is a noble gas dissolved in water, no adsorption process is recommended for this tracer. Ra^{2+} is expected to undergo mainly cation exchange sorption processes, which under the present circumstances should be possible to be modelled using a linear adsorption coefficient, K_d. K_d values for radium are given assuming geochemical similarity between Ra^{2+} and Ba^{2+} and therefore based on the K_d values reported in the Task 9C description, i.e. Table 2.4-9 in that report. This implies a K_d of 0.06 m^3/kg for Ra^{2+} in veined gneiss and a value of 0.08 m^3/kg in pegmatitic rock.

A3.1.6 General experimental conditions in the TDE experiment

All experimental conditions are already described in the Task 9C description.

A3.2 Natural Fracture

If the modelers want to expand their models and perform calculations of radium and radon concentrations in a natural fracture, this is encouraged. Results could then be compared to the radon and radium measurements that have been made in ONKALO. At this stage, however, it is not considered necessary to provide conditions for a specific facture and/or fracture type to be targeted in these calculations. If this extension of the task is considered successful and there is further interest, this might be done at a later stage.

Compilation of uranium concentrations measured in ONKALO rock

Table AA-1. Uranium concentrations in diatexitic gneiss (DGN) and veined gneiss (VGN) rock types.

Location	C_U (mg/kg)	Rock type	Location	C_U (mg/kg)	Rock type
OLKR12-672.00	4.59	DGN	OLKR12-313.40	3.97	VGN
ONK-PL2282.5	10.4	DGN	OLKR12-536.80	7.76	VGN
ONK-PL2292.5	3.7	DGN	OLKR12-650.20	5.12	VGN
ONK-PL2300.0	2	DGN	OLKR12-761.77	4.39	VGN
ONK-PL2302.5	8.7	DGN	ONK-PL2275.0	4.7	VGN
ONK-PL2307.5	7.1	DGN	ONK-PL2277.5	4.8	VGN
ONK-PL2310.0	7.9	DGN	ONK-PL2280.0	3.7	VGN
ONK-PL2312.5	6.3	DGN	ONK-PL2332.5	7.5	VGN
ONK-PL2337.5	4.8	DGN	ONK-PL2342.5	7.2	VGN
ONK-PL2340.0	3.2	DGN	ONK-PL2345.0	9.9	VGN
ONK-PL2355.0	4.5	DGN	ONK-PL2347.5	8.9	VGN
ONK-PL2357.5	11.3	DGN	ONK-PL2350.0	6.7	VGN
ONK-PL2362.5	11.6	DGN	ONK-PL2352.5	8.8	VGN
ONK-PL2387.5	8.8	DGN	ONK-PL2360.0	7.3	VGN
ONK-PL2392.5	9	DGN	ONK-PL2367.5	3.3	VGN
ONK-PL2400.0	11.3	DGN	ONK-PL2370.0	8.3	VGN
ONK-PL2407.5	7.7	DGN	ONK-PL2372.5	3.6	VGN
ONK-PL2422.5	13.8	DGN	ONK-PL2377.5	2.9	VGN
ONK-PL2425.0	10.5	DGN	ONK-PL2380.0	4.8	VGN
ONK-PL2427.5	8.9	DGN	ONK-PL2382.5	4.5	VGN
ONK-PL2440.0	8.2	DGN	ONK-PL2385.0	6.5	VGN
ONK-PL2442.5	8.8	DGN	ONK-PL2390.0	6.3	VGN
ONK-PL2445.0	13.6	DGN	ONK-PL2395.0	6.9	VGN
ONK-PL2447.5	12.2	DGN	ONK-PL2397.5	5.5	VGN
ONK-PL2450.0	11.2	DGN	ONK-PL2410.0	9	VGN
ONK-PL2452.5	20.9	DGN	ONK-PL2412.5	12.2	VGN
ONK-PL2465.0	10	DGN	ONK-PL2415.0	6	VGN
ONK-PL2467.5	19.1	DGN	ONK-PL2417.5	6.9	VGN
ONK-PL2475.0	9.5	DGN	ONK-PL2420.0	5.3	VGN
ONK-PL2477.5	8.8	DGN	ONK-PL2455.0	10.8	VGN
ONK-PL2495.0	8.7	DGN	ONK-PL2460.0	11.7	VGN
ONK-PL2500.0	14.6	DGN	ONK-PL2480.0	0.25	VGN
ONK-PL2512.5	11.7	DGN	ONK-PL2482.5	5.9	VGN
ONK-PL2517.5	15.5	DGN	ONK-PL2485.0	9.7	VGN
ONK-PL2525.0	7.7	DGN	ONK-PL2487.5	11.2	VGN
ONK-PL2537.5	8.7	DGN	ONK-PL2490.0	7.2	VGN
ONK-PL2540.0	8.4	DGN	ONK-PL2492.5	8.8	VGN
ONK-PL2542.5	9.4	DGN	ONK-PL2505.0	8.1	VGN
ONK-PL2545.0	9.2	DGN	ONK-PL2510.0	8.8	VGN
ONK-PL2547.5	45.6	DGN	ONK-PL2520.0	7	VGN
ONK-PL2550.0	13.2	DGN	ONK-PL2522.5	5.8	VGN
ONK-PL2560.0	9.3	DGN	ONK-PL2530.0	5.2	VGN
ONK-PL2562.5	29.1	DGN	ONK-PL2567.5	7.9	VGN
ONK-PL2570.0	6.4	DGN	ONK-PL2575.0	8.6	VGN
ONK-PL2587.5	12.3	DGN	ONK-PL2577.5	6.8	VGN
ONK-PL2592.5	18.1	DGN	ONK-PL2595.0	13.1	VGN
ONK-PL2605.0	10.9	DGN	ONK-PL2600.0	7.5	VGN
ONK-PL2610.0	12.7	DGN	ONK-PL2602.5	7.2	VGN
ONK-PL2612.5	9.4	DGN	ONK-PL2615.0	9.3	VGN

Location	C_U (mg/kg)	Rock type	Location	C_U (mg/kg)	Rock type
ONK-PL2617.5	22	DGN	ONK-PL2622.5	8.7	VGN
ONK-PL2620.0	8.2	DGN	ONK-PL2627.5	5.2	VGN
ONK-PL2625.0	8.2	DGN	ONK-PL2632.5	8.5	VGN
ONK-PL2635.0	4.5	DGN	ONK-PL2640.0	3.4	VGN
ONK-PL2645.0	6.9	DGN	ONK-PL2647.5	9.8	VGN
ONK-PL2652.5	10.6	DGN	ONK-PL2650.0	8	VGN
ONK-PL2655.0	10.8	DGN	ONK-PL2672.5	3.1	VGN
ONK-PL2657.5	10.8	DGN	ONK-PL2677.5	7.1	VGN
ONK-PL2670.0	9.3	DGN	ONK-PL2685.0	7.3	VGN
ONK-PL2675.0	9.6	DGN	ONK-PL2690.0	6.2	VGN
ONK-PL2680.0	7.9	DGN	ONK-PL2740.0	3.7	VGN
ONK-PL2682.5	12.6	DGN	ONK-PL2742.5	11.2	VGN
ONK-PL2687.5	9.9	DGN	ONK-PL2760.0	11.6	VGN
ONK-PL2700.0	11.3	DGN	ONK-PL2767.5	12.6	VGN
ONK-PL2702.5	18.8	DGN	ONK-PL2777.5	13	VGN
ONK-PL2705.0	19.7	DGN	ONK-PL2807.5	8.8	VGN
ONK-PL2707.5	10.8	DGN	ONK-PL2822.5	3.5	VGN
ONK-PL2710.0	3.8	DGN	ONK-PL2825.0	8.7	VGN
ONK-PL2712.5	2.9	DGN	ONK-PL2830.0	17	VGN
ONK-PL2715.0	13.7	DGN	ONK-PL2832.5	10.5	VGN
ONK-PL2717.5	13.8	DGN	ONK-PL2835.0	7.3	VGN
ONK-PL2720.0	15.8	DGN	ONK-PL2837.5	13.8	VGN
ONK-PL2725.0	10.9	DGN	ONK-PL2840.0	11.3	VGN
ONK-PL2727.5	11.2	DGN	OL-KR2_533.3_1	5.2	VGN
ONK-PL2730.0	15.9	DGN	OL-KR4_661.8_10	4	VGN
ONK-PL2735.0	3.9	DGN	OL-KR9_500.1_38	4.3	VGN
ONK-PL2737.5	10.8	DGN	OL-KR11_212_40	3.4	VGN
ONK-PL2747.5	17.7	DGN	OL-KR11_282_43	29.2	VGN
ONK-PL2750.0	10	DGN	OL-KR6_318.02_52	8.8	VGN
ONK-PL2752.5	9.9	DGN	OL-KR6_357.05_53	8	VGN
ONK-PL2755.0	9.9	DGN	OL-KR6_543.04_55	5.5	VGN
ONK-PL2762.5	11.3	DGN	OL-KR7_500.97_58	9.5	VGN
ONK-PL2765.0	15.9	DGN	OL-KR7_782.46_60	7.3	VGN
ONK-PL2770.0	13.8	DGN	OL-KR12_789.91_71	7.6	VGN
ONK-PL2772.5	10.4	DGN	OL-KR13_172.05_78	3.85	VGN
ONK-PL2775.0	9.2	DGN	OL-KR13_434.4_85	5.34	VGN
ONK-PL2780.0	6.7	DGN	OL-KR14_39.12_88	12.8	VGN
ONK-PL2790.0	0.25	DGN	OL-KR14_156.43_93	6.37	VGN
ONK-PL2810.0	6.2	DGN	OL-KR15_136.83_105	7.87	VGN
ONK-PL2817.5	9.2	DGN	OL-KR1_69_123	7.07	VGN
ONK-PL2827.5	11.4	DGN	OL-KR1_234.45_128	9.07	VGN
ONK-PL2842.5	11	DGN	OL-KR1_368.13_134	4.06	VGN
OL-KR2_997.7_6	8.3	DGN	OL-KR1_406.43_135	3.3	VGN
OL-KR4_513.95_7	3.1	DGN	OL-KR1_552.18_136	2.74	VGN
OL-KR4_572.05_8	4.2	DGN	OL-KR1_562.6_137	3.27	VGN
OL-KR7_30.8_13	3.7	DGN	OL-KR1_601.4_138	8.31	VGN
OL-KR7_36.1_14	7.6	DGN	OL-KR1_738.9_140	4.76	VGN
OL-KR7_241.95_17	3.4	DGN	OL-KR1_761.83_141	3.19	VGN
OL-KR8_4.6_19	5.6	DGN	OL-KR1_843.86_143	5.05	VGN
OL-KR8_148.05_20	4.7	DGN	OL-KR5_74.4_146	3.87	VGN
OL-KR10_149.9_25	4.4	DGN	OL-KR5_167.93_148	3.66	VGN
OL-KR10_271.25_27	4.8	DGN	OL-KR5_266.9_150	2.5	VGN
OL-KR10_355.1_28	6.1	DGN	OL-KR5_412.5_155	6.44	VGN
OL-KR10_438.1_29	3.6	DGN	OL-KR5_502.42_156	6.03	VGN
OL-KR9_162.15_33	7.9	DGN	OL-OC_164	13	VGN

Location	C_U (mg/kg)	Rock type	Location	C_U (mg/kg)	Rock type
OL-KR11_123.9_39	3.2	DGN	OL-OC_173	5.63	VGN
OL-KR11_242.2_42	3.8	DGN	OL-OC_180	5.19	VGN
OL-KR11_506.9_46	5.7	DGN	OL-KR15_286.97_186	7.7	VGN
OL-KR11_713.4_47	3	DGN	OL-KR15_334.61_187	3.1	VGN
OL-KR11_897.6_49	0.6	DGN	OL-KR19_68.13_189	3.1	VGN
OL-KR11_932_50	0.9	DGN	OL-KR19_266.4_196	2.8	VGN
OL-KR7_421.65_57	5.8	DGN	OL-KR19_334.23_197	3.8	VGN
OL-KR12_81.92_61	13.1	DGN	OL-KR19_395.74_199	8.8	VGN
OL-KR12_300.52_65	6.7	DGN	OL-KR19_435.5_201	5.7	VGN
OL-KR12_352.47_66	6.2	DGN	OL-KR20_114.35_210	5.1	VGN
OL-KR12_500.93_67	6.8	DGN	OL-KR20_139.22_211	8.2	VGN
OL-KR12_574.65_68	5	DGN	OL-KR20_180.45_212	5	VGN
OL-KR13_51.32_73	9.75	DGN	OL-KR20_216.4_213	5.5	VGN
OL-KR8_369.28_183	9.2	DGN	OL-KR20_350.5_217	6	VGN
OL-KR8_512.03_185	5.3	DGN	OL-KR20_459.62_218	5.8	VGN
OL-KR22_93.25_235	5.6	DGN	OL-KR20_44.62_222	13	VGN
OL-KR22_202.59_238	7.8	DGN	OL-KR21_31.04_223	5	VGN
OL-KR22_227.85_239	12	DGN	OL-KR21_142.08_227	3.3	VGN
OL-KR22_288.1_240	9.2	DGN	OL-KR21_170.11_229	4.1	VGN
OL-KR22_343.02_241	10	DGN	OL-KR21_213.12_230	4.4	VGN
OL-KR22_433.07_243	5.5	DGN	OL-KR21_221.25_231	3.9	VGN
OL-KR22_477.9_244	10	DGN	OL-KR21_245.16_232	4.3	VGN
OL-KR22_31.16_245	2.1	DGN	OL-KR22_127.85_237	6.9	VGN
OL-KR23_77.82_247	3.3	DGN	OL-KR23_167.14_249	6.2	VGN
OL-KR25_96.79-96.87	6.55	DGN	OL-KR23_293.61_250	21.9	VGN
OL-KR47_899.45	1.31	DGN	OL-KR23_18.61_251	3.5	VGN
OL-KR45_176.90	5.02	DGN	OL-KR11_421.44-421.52	4.02	
14-ISAA-09	5.25	DGN	OL-KR25_492.62-492.73	4.05	VGN
15.1-ISAA-09	4.61	DGN	OL-KR25_51.07	11.6	VGN
15.2-ISAA-09	4.64	DGN	OL-KR25_56.42	6.14	VGN
16-ISAA-09	8.35	DGN	OL-KR20_217.44	4.22	VGN
17-ISAA-09	4.81	DGN	OL-KR20_223.60	4.5	VGN
23-ISAA-09	4.49	DGN	OL-KR20_223.73	3.8	VGN
35-ISAA-09	6.17	DGN	OL-KR20_421.65-421.78	3.78	VGN
OLKR12-367.17	33.4	DGN	OL-KR15_212.85	5.66	VGN
OLKR22b-19.86	5.31	DGN	OL-KR15_267.38	11.9	VGN
OLKR23-43.01	7.68	DGN	OL-KR4_167.51	6.41	VGN
OLKR28-359.60	8.36	DGN	OL-KR4_523.85	4.18	VGN
OLKR9-561.97	7.03	DGN	OL-KR4_758.85	3.09	VGN
			OL-KR4_759.50	3.5	VGN
			11-ISAA-09	6.19	VGN
			12-ISAA-09	8.97	VGN
			13-ISAA-09	4.46	VGN
			45-ISAA-09	5.36	VGN
			48-ISAA-09	8.51	VGN
			OLKR12-794.75	10.6	VGN
			OLKR39-320.34	5.03	VGN
			OLKR4-370.40	2.19	VGN
			OLKR55-277.90	1.31	VGN
			OLKR9-502.64	4.24	VGN

Table AA-2. Uranium concentrations in mafic gneiss (MFGN) and pegmatitic granite (PGR) rock types.

Location	C_U (mg/kg)	Rock type	Location	C_U (mg/kg)	Rock type
OL-KR4_781.8_11	5.3	MFGN	OLKR12-660.54	1.2	PGR
OL-KR7_204.7_16	2.1	MFGN	OLKR12-561.28	3.38	PGR
OL-KR10_528.4_30	5.3	MFGN	OLKR12-671.74	1.39	PGR
OL-KR9_124.65_32	1.2	MFGN	ONK-PL2267.5	3.6	PGR
OL-KR11_240.3_41	2.4	MFGN	ONK-PL2290.0	10.8	PGR
OL-KR13_163.72_76	1.54	MFGN	ONK-PL2295.0	4.9	PGR
OL-KR17_10.37_115	1.04	MFGN	ONK-PL2297.5	3.9	PGR
OL-KR17_16.52_116	0.9	MFGN	ONK-PL2315.0	8.2	PGR
OL-KR17_20.85_117	1.37	MFGN	ONK-PL2330.0	5.1	PGR
OL-KR1_875.25_144	0.95	MFGN	ONK-PL2335.0	5.7	PGR
OL-KR5_325.75_151	3.09	MFGN	ONK-PL2405.0	7.1	PGR
OL-KR5_347.77_152	2.46	MFGN	ONK-PL2462.5	0.7	PGR
OL-KR5_354.5_153	2.1	MFGN	ONK-PL2470.0	3.7	PGR
OL-OC_171	2.41	MFGN	ONK-PL2472.5	13.8	PGR
OL-OC_174	2.68	MFGN	ONK-PL2502.5	9.9	PGR
OL-OC_175	0.68	MFGN	ONK-PL2692.5	5	PGR
OL-KR19_365.5_198	2.1	MFGN	ONK-PL2697.5	4.7	PGR
OL-KR20_490.61_219	2	MFGN	ONK-PL2745.0	12.4	PGR
OL-KR22_124.37_236	1.6	MFGN	ONK-PL2757.5	7.3	PGR
OLKR12-384.50	8.89	MGN	ONK-PL2782.5	6.7	PGR
ONK-PL2262.5	6.3	MGN	ONK-PL2785.0	9.2	PGR
ONK-PL2265.0	14	MGN	ONK-PL2787.5	10.2	PGR
ONK-PL2270.0	7.7	MGN	OL-KR2_750.5_5	15.1	PGR
ONK-PL2272.5	6.6	MGN	OL-KR4_844.1_12	2.1	PGR
ONK-PL2285.0	6.8	MGN	OL-KR7_271.9_18	5.1	PGR
ONK-PL2287.5	5.4	MGN	OL-KR8_209.3_21	4.1	PGR
ONK-PL2305.0	2.7	MGN	OL-KR10_209.2_26	6.1	PGR
ONK-PL2327.5	8.8	MGN	OL-KR9_362.1_36	11	PGR
ONK-PL2365.0	2.7	MGN	OL-KR11_828.6_48	9.7	PGR
ONK-PL2375.0	2.7	MGN	OL-KR7_541.64_59	3.4	PGR
ONK-PL2630.0	5.3	MGN	OL-KR12_213.6_62	4.8	PGR
ONK-PL2642.5	0.25	MGN	OL-KR12_634.92_70	1.3	PGR
ONK-PL2695.0	3.5	MGN	OL-KR13_75.8_75	5.41	PGR
ONK-PL2732.5	6.2	MGN	OL-KR13_269.18_79	3.74	PGR
ONK-PL2820.0	13.2	MGN	OL-KR13_454_86	42.6	PGR
OL-KR2_636.15_2	3.6	MGN	OL-KR14_71.25_89	3.55	PGR
OL-KR2_647.8_3	2.6	MGN	OL-KR14_322.94_94	1.59	PGR
OL-KR8_313.1_24	2.9	MGN	OL-KR14_361.56_95	4.22	PGR
OL-KR9_243.6_35	4.2	MGN	OL-KR15_72.27_101	1.17	PGR
OL-KR9_400.1_37	4.6	MGN	OL-KR15_87.64_102	6.88	PGR
OL-KR12_617.85_69	4.5	MGN	OL-KR16_109.39_108	126	PGR
OL-KR13_24.8_72	10.4	MGN	OL-KR17_42.28_111	7.88	PGR
OL-KR13_56.8_74	3.74	MGN	OL-KR18_70.37_119	9.2	PGR
OL-KR13_167.69_77	4.53	MGN	OL-KR4_747.69	5.32	PGR
OL-KR13_271.9_80	2.98	MGN	24-ISAA-09	2.47	PGR
OL-KR13_325.37_83	3.8	MGN	30-ISAA-09	3.29	PGR
OL-KR13_469.92_87	3.32	MGN	31-ISAA-09	2.86	PGR
OL-KR14_369.7_96	3.64	MGN	32-ISAA-09	1.86	PGR
OL-KR14_446.16_100	4	MGN	34-ISAA-09	1.78	PGR
OL-KR15_94.15_103	3.88	MGN	36-ISAA-09	11.8	PGR
OL-KR16_52.36_107	2.96	MGN	37-ISAA-09	1.05	PGR
OL-KR16_34.25_110	4.88	MGN	38-ISAA-09	12.1	PGR
OL-KR17_80.58_112	5.59	MGN	43-ISAA-09	12.3	PGR
OL-KR17_92.8_113	4.67	MGN	44-ISAA-09	9.22	PGR
OL-KR1_74.6_124	5.55	MGN	OLKR11-449.67	0.53	PGR

Location	C_U (mg/kg)	Rock type	Location	C_U (mg/kg)	Rock type
OL-KR1_107.85_125	2.21	MGN	OLKR13-21.87	5.54	PGR
OL-KR1_130.7_126	5.16	MGN	OLKR13-40.16	4.21	PGR
OL-KR1_262.1_129	4.09	MGN	OLKR16-98.70	1.39	PGR
OL-KR1_349.5_133	4.19	MGN	OLKR28-522.04	7.81	PGR
OL-KR1_831.35_142	3.33	MGN	OLKR37-73.14	2.49	PGR
OL-OC_165	6.45	MGN			
OL-OC_167	4.5	MGN			
OL-OC_169	4.33	MGN			
OL-OC_170	4.05	MGN			
OL-OC_179	5.73	MGN			
OL-OC_181	4.87	MGN			
OL-KR19_88.16_190	3.15	MGN			
OL-KR19_136.63_191	2.2	MGN			
OL-KR19_197.15_192	3.6	MGN			
OL-KR19_240.73_194	4.1	MGN			
OL-KR19_428.45_200	3.6	MGN			
OL-KR19_467.54_202	5.5	MGN			
OL-KR19_509.46_204	3.3	MGN			
OL-KR19_509.83_205	2.4	MGN			
OL-KR19_18.9_206	5.3	MGN			
OL-KR20_47.46_208	8.2	MGN			
OL-KR20_107.21_209	4.6	MGN			
OL-KR20_247.4_214	2.6	MGN			
OL-KR20_492.36_220	2.6	MGN			
OL-KR20_34.64_221	4.2	MGN			
OL-KR22_69.07_234	1.9	MGN			
OL-KR22_369.86_242	4.8	MGN			
OL-KR14_461.91-462.04	3.36	MGN			
OL-KR14_491.09-491.19	4.06	MGN			
OL-KR4_891.71	5.16	MGN			
OL-KR12_311.00	4.04	MGN			
OL-KR12_384.00	6.5	MGN			
OL-KR12_392.00	5.06	MGN			
OL-KR12_536.00	11.9	MGN			
OL-KR12_561.00	1.34	MGN			
OL-KR12_566.00	8.32	MGN			
OL-KR12_671.00	4.86	MGN			
OL-KR12_737.00	2.2	MGN			
OL-KR47B_18.90-19.20	1.31	MGN			
22-ISAA-09	4.31	MGN			
27-ISAA-09	4.03	MGN			
33-ISAA-09	10.4	MGN			
47-ISAA-09	7.31	MGN			
OLKR3-390.36	3.07	MGN			
OLKR4-807.00	1.5	MGN			
OLKR42-192.39	5.08	MGN			
OLKR52-423.93	4.2	MGN			

Table AA-3. Uranium concentrations in quartz gneiss (QGN) and tonalitic-granodioritic-granitic (TGG) rock type.

Location	C_U (mg/kg)	Rock type	Location	C_U (mg/kg)	Rock type
OLKR29-749.50	2.26	QGN	OLKR1-637.32	7.46	TGG
ONK-PL2457.5	6	QGN	OLKR1-618.44	2.82	TGG
ONK-PL2497.5	4.2	QGN	OL-KR2_703.1_4	7.5	TGG
ONK-PL2515.0	2.4	QGN	OL-KR8_238.55_22	2.1	TGG
ONK-PL2565.0	3.8	QGN	OL-KR8_262.1_23	2.5	TGG
ONK-PL2722.5	3.9	QGN	OL-KR9_52.9_31	1.6	TGG
OL-KR4_620.34_9	2.7	QGN	OL-KR11_358.8_44	3.6	TGG
OL-KR7_133.25_15	3.2	QGN	OL-KR11_443.4_45	2.5	TGG
OL-KR9_216.35_34	2.9	QGN	OL-KR11_990.2_51	9.3	TGG
OL-KR7_327.88_56	4.9	QGN	OL-KR12_270.6_63	11.1	TGG
OL-KR14_100.5_91	2.88	QGN	OL-KR12_275.12_64	12.9	TGG
OL-KR18_52.79_118	3.35	QGN	OL-KR13_282.15_81	5.87	TGG
OL-KR18_98.73_121	2.81	QGN	OL-KR13_302.93_82	7.25	TGG
OL-KR1_145.35_127	2.76	QGN	OL-KR13_389.29_84	6.4	TGG
OL-KR1_279.13_130	3.26	QGN	OL-KR14_82.27_90	13.3	TGG
OL-KR5_523.15_157	2.39	QGN	OL-KR14_112.43_92	8.06	TGG
OL-OC_158	3.26	QGN	OL-KR14_375.48_97	4.3	TGG
OL-OC_162	2.73	QGN	OL-KR14_424.02_99	6.95	TGG
OL-OC_163	3.41	QGN	OL-KR15_104.35_104	14.1	TGG
OL-KR8_497.06_184	1.9	QGN	OL-KR15_36.85_106	14.5	TGG
OL-KR19_250_195	2.5	QGN	OL-KR16_122.07_109	17.9	TGG
OL-KR19_504.08_203	2.8	QGN	OL-KR18_83.23_120	17.9	TGG
OL-KR19_21.38_207	2.8	QGN	OL-KR1_297.45_131	5.99	TGG
OL-KR21_50.9_224	2.6	QGN	OL-KR1_333.9_132	8.01	TGG
			OL-KR1_637.76_139	3.66	TGG
			OL-KR1_943.65_145	5.9	TGG
			OL-KR5_151.45_147	2.88	TGG
			OL-KR5_225_149	4.61	TGG
			OL-KR5_378.55_154	2.56	TGG
			OL-OC_159	3.66	TGG
			OL-OC_160	2.75	TGG
			OL-OC_161	6.32	TGG
			OL-OC_166	3.8	TGG
			OL-OC_168	8.26	TGG
			OL-OC_172	3.67	TGG
			OL-OC_176	4.91	TGG
			OL-OC_177	3.71	TGG
			OL-OC_178	1.3	TGG
			OL-KR8_317.95_182	8.7	TGG
			OL-KR15_387.98_188	6.7	TGG
			OL-KR19_206.72_193	6.3	TGG
			OL-KR20_258.1_215	4.2	TGG
			OL-KR20_310.35_216	5	TGG
			OL-KR21_82.9_225	5.4	TGG
			OL-KR21_96.38_226	3.1	TGG
			OL-KR21_162.05_228	5.6	TGG
			OL-KR21_273.15_233	5.9	TGG
			OL-KR13_175.19-175.38	14.2	TGG

# On recoil capture processes in granitic rock

James Crawford, Kemakta

Background

Uranium occurs naturally in granitic rocks with an average global abundance of about 4.4 ppm although typically ranges from 1–10 ppm (Langmuir 1997). Pegmatites, on the other hand, can have uranium contents ranging from 40–90 ppm. Median values for Finnish rocks from the Olkiluoto site range from 4–6 ppm (Aaltonen et al. 2010). Similar ranges are reported for site specific rocks from the Forsmark and Laxemar investigation areas (Drake et al. 2006, Sandström and Stephens 2009). Granite from the Stripa mine is somewhat unusual in having a relatively high U content on the order of 44 ppm (Andrews et al. 1989a).

The U-content of granitic rock is not evenly distributed, however, and it tends to be enriched in matrix accessory minerals including zircon, apatite, and monazite (Eggeling et al. 2013). Uranium is also commonly present as uraninite or enriched in thorite and thorianite inclusions in biotite. In the Stripa granite, the highest concentrations have been found in opaque minerals associated with chlorite and biotite filled fractures where local concentrations of 10 000–25 000 ppm are not uncommon while concentrations ranging from 4 000–6 000 ppm are typical along grain boundaries and microfractures (Andrews et al. 1982, and references therein). The U-concentration in non-fractured quartz and feldspar mineral grains, on the other hand, was found to be negligible based on radiographic fission track analysis.

These observations appear to be typical for granitic rocks and pegmatites in general and not specific to the Stripa site. The U found within the microfractures of Stripa granite is predominantly thought to be uraninite, UO_2 (Andrews et al. 1989b), although more recent work using modern microprobe techniques (e.g. SEM-EDS) has also revealed the additional presence of (urano)thorite, haiweeite, uranophane, and coffinite hosted in microfractures of Forsmark rock samples (Krall et al. 2015). The Stripa granite, however, is likely to be an exception given that the high U-concentrations may be due to metasomatic processes that might be unusual relative to more common granitic rock types including metamorphic granites and gneiss found at Forsmark and Olkiuloto. Some typical U-rich inclusions are shown in Figure AB-1 (taken from Jelinek and Eliasson 2015) which also shows some typical examples of radiation damage (microfractures and alteration halos).

Radioactive disequilibrium in natural rocks and groundwater systems has been observed for many years. Typically, one finds higher $^{234}U/^{238}U$ activity ratios in groundwater that has permeated rock than that which would be predicted on the basis of secular equilibrium (i.e. $^{234}U/^{238}U$ » 1). In Forsmark groundwater, for example, the $^{234}U/^{238}U$ activity ratio is roughly 3 ± 1 which, although higher than secular equilibrium, is not unusual. Indeed, many sampled groundwaters in Sweden and Finland have been found to have $^{234}U/^{238}U$ activity ratios in the range of 2–4 and values approaching 10 are not unknown (Suksi et al. 2006). The principal explanatory mechanism for this is the process known as alpha recoil involving daughter radionuclides of the naturally occurring decay chains, although it may be amplified by redox fractionation with larger ratios apparently associated with rapid transition of oxidising to strongly reducing groundwater conditions. Although the decay chain involving ^{238}U is the most well-studied owing to its importance for ^{222}Rn emanation from geological material, the decay chains of ^{232}Th, and to a lesser extent ^{235}U have also been studied extensively as natural analogues.
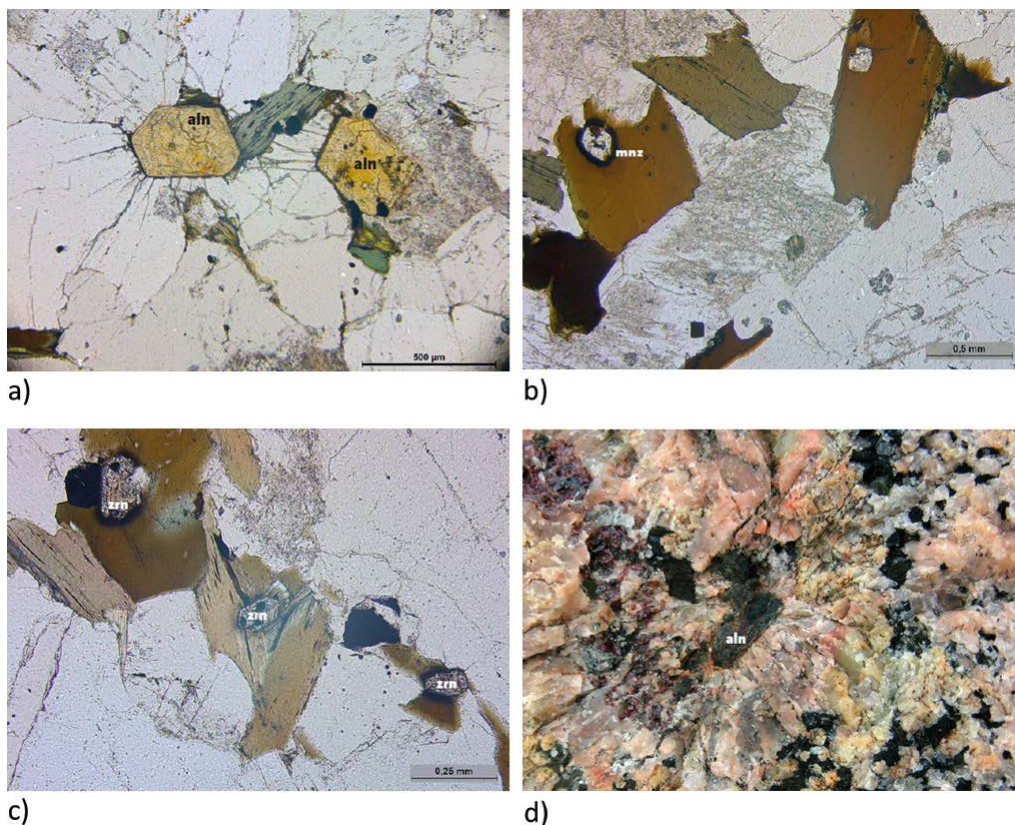
Figure AB-1. *Thin section photographs of Bohus granite (a-c) and pegmatite (d) showing crystal inclusions of U-enriched allanite (a, d) and monazite inclusions in biotite (b), and zircon inclusions in biotite (c). Note the radial microfractures surrounding alanite in response to expansion stress arising due to recoil damage and subsequent chemical alteration. Dark halos (α-damage) are also visible in the biotite surrounding the monazite and zircon inclusions. (Images are reproduced from Jelinek and Eliasson 2015).*

Porewater α-recoil capture processes

Generally, the α-decay energies of the ^{238}U and ^{232}Th chain lie in the interval 4–8 MeV. Upon decay, an equal momentum is imparted to both the α-particle itself and the daughter nucleus. Owing to the large difference in mass, however, the bulk of the decay energy is transmitted to the α-particle while only a small fraction (60–150 keV) is imparted to the daughter nuclide in the form of recoil energy (Sun and Semkow 1998). When travelling through a medium (such as a mineral crystal, water, or air) the energy of the recoiling nucleus is dissipated by coulombic interactions with both nuclei of atoms in the medium as well as with the electron clouds surrounding atoms. The distance over which a recoil nucleus can travel is characterised as the recoil- or stopping range. While the range of a typical α-particle in water is about 50 μm, for a recoil nucleus the range is only about 80 nm. Since the dissipation of kinetic energy in a medium is a stochastic process, there is a probability distribution associated with the recoil range. The standard deviation of the recoil range is referred to as longitudinal and lateral "straggling" for variation along the principal axes relative to the recoil trajectory.

For a radionuclide undergoing α-decay there are several different possible outcomes for the fate of the recoil nucleus depending on the location of the decaying atom in the material. If the decaying atom is close to the surface of a mineral grain, the daughter can recoil deeper into the mineral grain or be ejected into pore space surrounding the mineral grain. For the daughter nuclides that escape into the pore space, this is called "direct recoil" emanation (see arrow 1 depicted in Figure AB-2). There are, however, other possibilities. A recoil nucleus may travel sufficiently far to be implanted into an adjacent geological surface. This may cause the recoil nucleus to be effectively immobilized (arrow 2 in Figure AB-2) or, if deposited at a sufficiently shallow depth in the interface, it may be

leached out again by back-diffusion through the zone of damage caused by the implantation process (arrow 3 in Figure AB-2). Atoms that are re-mobilized in this fashion are referred to as "indirect recoil" emanations. A final possibility if the medium is sufficiently fine grained relative to the stopping distance is a so-called penetrating recoil emanation (arrow 4 in Figure AB-2) where the recoil nucleus has sufficient energy to completely penetrate an adjacent mineral and be deposited in porewater adjoining its reverse side.

Recoiling atoms ejected from a mineral surface have a range of energies ranging from 0 keV up to the original recoil energy of the nucleus (86.13 keV for ^{222}Rn) depending upon from how deep beneath the mineral surface the decay process occurred. For an indirect recoil process, the energy of the implanting nucleus must be less than about ~5 keV for the implanted atom to be sufficiently close to the surface to subsequently leach out into porewater (Kornelsen 1964).

It has been observed in a number of studies (e.g. Sakoda et al. 2011, Sun and Furbish 1995 and references therein) that the emanation of ^{222}Rn is frequently higher by up to a factor of 5 in water-saturated than dry samples. This is partly attributed to the greater stopping power of water since the recoil range in air is ~700 times that in water, and partly due to indirect recoil since water is thought to facilitate the out-diffusion of recoil atoms (see, e.g. Fleischer 1983). When the pore space is air-filled, the ejected recoil nuclei can readily traverse the pore space and be embedded in adjacent mineral interfaces thereby giving a lower emanation fraction than what would be obtained if the pore space were water saturated. Semkow (1991) invokes penetrating recoil and fractal argumentation to explain higher than expected emanation rates as a function of grain size that cannot be explained adequately by the indirect recoil mechanism.

The emanation of ^{222}Rn is complicated by the fact that there are four α-decay events in the decay chain between ^{238}U and ^{222}Rn. Radionuclides above ^{222}Rn (i.e. ^{234}Th, ^{230}Th, ^{226}Ra) that are ejected by α-recoil from a solid may be re-adsorbed to surfaces, or form surface precipitates in the pore space surrounding U-enriched mineral grains. The intermediate nuclides ^{234}Pa (^{234m}Pa), and ^{234}U arise from β-decay processes and are not directly ejected but can only form from decay of the parent nuclide in the pore space. Furthermore, the daughter radionuclides following ^{238}U will be depleted in the surface zone of the U-enriched mineral grains due to each successive α-recoil, implying that the rate of ^{222}Rn emanation will be less than that predicted by assuming secular equilibrium throughout the mineral grain. If the ^{238}U enrichment is sufficiently high in the mineral grain, however, the difference might be minimal compared to other uncertainties.

In principle, the main U-bearing mineral phases such as uraninite (referred to here as a "primary reservoir") can also dissolve in pore water up to their solubility limit and become a disseminated source of daughter radionuclides in the rock matrix (both sorbed and freely dissolved). For a typical granite, however, the rate of production by this mechanism is likely many orders of magnitude less than the rate of production from the primary reservoir even given very pessimistic assumptions for porewater capture efficiency.
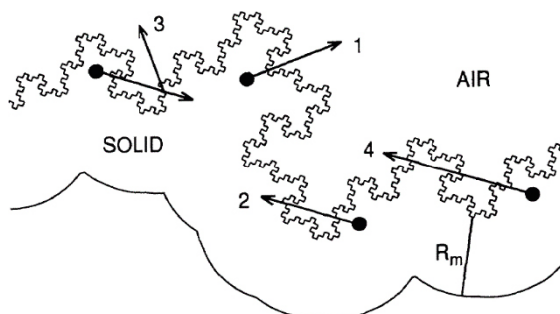
Figure AB-2. *Stylised representation of recoil capture processes within a pore space from a mineral surface here represented as a fractal surface in cross-section. Arrows denote: 1) direct recoil, 2) implantation, 3) indirect recoil (i.e. remobilisation of shallow implanted recoil nuclei), and 4) penetrating recoil capture. (Figure taken from Semkow 1991).*

Each successive α-decay event is associated with its own porewater α-recoil capture probability and implantation probability. In general, it is necessary to take these factors into account when estimating the net emanation rate of ^{222}Rn corresponding to the fourth α-recoil event (see, for example, Sun and Semkow 1998). If the rate of primary reservoir production (i.e. direct emanation of ^{222}Rn from ^{238}U enriched mineral grains) can be shown to be much greater than the disseminated rate of production, then it might be reasonable to neglect multiple recoil fractionation. If calculations only consider the production of ^{222}Rn directly from the measured activity of ^{226}Ra in the rock, on the other hand, then only one α-recoil event needs to be considered. The distribution of ^{226}Ra in the rock then needs to be accounted for, however, since this may differ from the distribution of ^{238}U in the rock matrix.

Theoretical models of porewater α-recoil capture

There are many theoretical models for α-recoil capture in the literature. Some of these are summarised in Table AB-1. In principle, all assume a single α-recoil process from a parent radionuclide contained in a solid phase (primary reservoir). As noted above, however, if the rate of primary production is sufficiently high and surface layer daughter depletion can be presumed negligible, then they may be sufficiently accurate to estimate ^{222}Rn production directly from the bulk ^{238}U content if secular equilibrium is additionally assumed in the U-enriched mineral grain. Most of the equations given in Table AB-1 assume a uniform distribution of radionuclide in the primary reservoir. The equations from Key et al. (1979) and Semkow (1990), however, specifically consider the case of Ra-mineral coatings on spherical particles for the estimation of ^{222}Rn emanation. This might be more appropriate if measured Ra-activities are used as the basis of calculations instead of ^{238}U in which case assuming uniform Ra-activities in the primary mineral phases might underestimate the true emanation fraction of ^{222}Rn.

Since many of the equations given in Table AB-1 are for very specific geometric situations and particle shapes, they are less useful in the general case where there is very little information concerning morphology of the primary U-bearing minerals and their location in the rock matrix. The most general formula ("B84") given by Bossus (1984) makes no particular assumption about U-bearing mineral morphology apart from the underlying assumptions that 1) the characteristic particle dimension is greater than the recoil distance in the mineral, and 2) the scale of surface roughness incorporated in the specific surface area measurement is smaller than the recoil distance in the mineral. It can be noted that the B84 formula should give the maximum rate of ^{222}Rn emanation assuming no implantation in adjacent mineral interfaces. It can be interpreted as an upper limit for uniformly distributed parent radionuclides in a mineral grain. The formula ("S91") by Semkow (1991) is useful if additional information about the fractal nature of the primary U-bearing mineral surface is known, although in the limit of D = 2 (Euclidian case), the result simplifies to the same formula as B84.

The formula ("LN94") given by Liu and Neretnieks (1994) has similar underlying assumptions as the B84 formula although additionally assumes that the film of porewater with thickness, *b* surrounding individual mineral grains is much less than the recoil distance in water (R_w) and that the porewater film thickness is proportional to particle size. The LN94 formula considers implantation effects unlike many of the other formulae given in Table AB-1 which makes it relatively unique (with the exception of the model by Stajic and Nikezic 2014). Provided the porosity in the immediate vicinity of the primary U-bearing mineral can be approximately estimated, this might be useful for setting more realistic bounds on the emanation fraction. It should be noted, however, that the LN94 formula is intended for the quantification of radiolysis rather than emanation which leads to slightly different results. The implications of this were discussed in more detail in Addendum C, but is now removed.

Another aspect of theoretical calculation of α-recoil capture that might be considered is that the formulae given in Table AB-1 typically only consider single characteristic particle sizes. In general, smaller particles with higher surface to volume ratios will emanate ^{222}Rn more effectively than larger particle sizes. This might need to be considered explicitly in calculations since an average U-bearing grain size (and average porosity) may not be representative for the bulk ^{222}Rn emanation fraction.

Table AB-1. Some theoretical expressions used to estimate emanation coefficients for porewater α-recoil capture of radionuclides in geological materials. (note that the emanation coefficient is a fraction in the range 0–1).

Formula	Geometry	Reference
$\eta = \dfrac{3}{4}\dfrac{R_c}{r_0} - \dfrac{1}{16}\left(\dfrac{R_c}{r_0}\right)^3$ r_0 is the particle radius, R_c is recoil range in solid.	sphere $2r_0 \geq R_c$ (unconfined)	Flügge and Zimens (1939), Kigoshi (1971)
$\eta = \Lambda_i f_s + \left(\Lambda_r + \Lambda_0^2\right)f_u + \Lambda_0 f_h$ $\Lambda_i = \dfrac{3}{4}\dfrac{R_c}{r_0} - \dfrac{1}{16}\left(\dfrac{R_c}{r_0}\right)^3 \quad 2r_0 \geq R_c$ $\Lambda_r = \begin{cases} \dfrac{1}{8} + \dfrac{1}{24}\dfrac{R_c}{r_0} & R_c \leq r_0 \\[2mm] \dfrac{15}{24} - \dfrac{4}{24}\dfrac{r_0}{R_c} - \dfrac{7}{24}\dfrac{R_c}{r_0} & R_c > r_0 \end{cases}$ $\Lambda_0 = \dfrac{1}{2}\left(1 + \dfrac{R_c}{2r_0}\right)$ f_s = fraction of supported ^{226}Ra (uniformly distributed in primary reservoir); f_u = fraction of surface sorbed ^{226}Ra derived from unsupported, surface sorbed ^{230}Th; f_h = fraction of surface sorbed unsupported ^{226}Ra of exogenous origin.	surface-coated sphere (unconfined)	Key et al. (1979)
$\eta = \dfrac{1}{4}A_c \rho_c R_c$ A_c is the specific surface area (m²/kg) of the primary radionuclide-bearing phase, ρ_c is crystallographic density of the solid.	Euclidian solid $r_0 > R_c$ (unconfined)	Bossus (1984),
$\eta = \dfrac{\left(2 - \dfrac{d}{R_c} + \dfrac{R_c}{r_0}\left(1 - \dfrac{d}{R_c}\right)^2 - \dfrac{R_c d}{12 r_0^2}\left(1 + \left(1 - \dfrac{d}{R_c}\right)\left(5 - 3\dfrac{d}{R_c}\right)\right)\right)}{4\left(1 - \dfrac{d}{r_0} + \dfrac{1}{3}\left(\dfrac{d}{R_c}\right)^2\right)}$ d is the thickness of surface layer	surface-coated sphere $2r_0 \leq R_c$ $0 \leq d \leq 2r_0 - R_c$ (unconfined)	Semkow (1990)
$\eta = \dfrac{\left(1 - \dfrac{d}{r_0} + \dfrac{1}{3}\left(\dfrac{d}{r_0}\right)^2 - \dfrac{r_0}{3d}\left(1 - \dfrac{3}{4}\dfrac{R_c}{r_0} + \dfrac{1}{16}\left(\dfrac{R_c}{r_0}\right)^3\right)\right)}{4\left(1 - \dfrac{d}{r_0} + \dfrac{1}{3}\left(\dfrac{d}{R_c}\right)^2\right)}$	surface-coated sphere $2r_0 \leq R_c$ $2r_0 - R_c \leq d \leq R_c$ (unconfined)	Semkow (1990)
$\eta = \dfrac{R_c\left(1 - \dfrac{1}{12}\left(\dfrac{R_c}{r_0}\right)^2\right)}{d\left(1 - \dfrac{d}{r_0} + \dfrac{1}{3}\left(\dfrac{d}{R_c}\right)^2\right)}$	surface-coated sphere $2r_0 \leq R_c$ $R_c \leq d$ (unconfined)	Semkow (1990)
$\eta = \dfrac{C}{4-D}\left(\dfrac{R_c}{2r_0}\right)^{3-D}$ $\dfrac{S}{V} = C r_0^{D-3} a^{D-3}$ C is a shape coefficient ($C = 1$ for a plate); S/V is the surface to volume ratio; D is the fractal dimension.	solid with fractal surface (unconfined)	Semkow (1991)

Formula	Geometry	Reference
$\eta = \dfrac{1}{4}\left(\dfrac{2^{D-1}}{4-D}\left(\dfrac{a}{R_c}\right)^{D-2}\right)R_c A_c \rho_c$ a is diameter of the adsorbate molecule used in the BET determination of specific surface area, A_c (3.5Å for N_2); D is the fractal dimension.	solid with fractal surface (unconfined)	Semkow (1991), Bourdon et al. (2009)
$\eta = \dfrac{3}{8}\left(\dfrac{\varepsilon_p}{1-\varepsilon_p}\right)\dfrac{R_c}{R_w}$ R_w is the recoil range in water, ε_p is the local porosity surrounding the U-enriched solid. It is furthermore assumed that the water film thickness, b surrounding individual grains is significantly less than the recoil distance in water (i.e. $b \ll R_w$).	euhedral $r_0 > R_c$ [4] (confined pore space)	Liu and Neretnieks (1994)
$\eta = \dfrac{1}{8}R_c \dfrac{K}{r_0}\lambda_r$ K = 6 for sphere; λ_r = surface roughness factor; for shape factors of prolate spheroids and other forms see: Cartwright (1962).	Spheroidal (unconfined)	Lee et al. (2010)
$\eta_S = \left(\dfrac{1}{2}-\dfrac{3\left(4r_0^2+3R_c^2-8r_0 R_c\right)}{16\left(3r_0^2-3r_0 R_c+R_c^2\right)}\right)\cdot\left(\dfrac{r_0^3-(r_0-R_c)^3}{r_0^3}\right)$	Single sphere (unconfined)	Stajic and Nikezic (2014)
$\eta_{PS} = \eta_S \cdot \dfrac{\int_0^{L_w}\overline{\omega}(\xi)d\xi}{R_w}$ $\overline{\omega}(\xi) = \dfrac{N}{8r_0 R_w^2}\left(\left(1-\dfrac{t_2^2}{3r_0^2}\right)(t_1^3-t_2^3)-3t_2^2(t_1-t_2)+\dfrac{t_1^5-t_2^5}{5r_0^2}\right)-\dfrac{N-2}{2}$ $t_1 = r_0 + R_w$ $t_2 = \sqrt{r_0^2+R_w^2}$	Packed spheres of constant size $r_0 \geq \dfrac{R_w}{\sqrt{3}-1}$ (confined pore space within packed volume)	Stajic and Nikezic (2014)

Note: N is the coordination number for spherical packing, e.g. N = 6 (simple packing), 8 (BCC), 12 (FCC).

Measurements of ^{222}Rn emanation fraction reported in the literature

There are many references in the literature reporting exhalation rates of ^{222}Rn in geological materials (see, e.g. Cameron 1987, Sakoda et al. 2011 and references therein). These are typically reported as mass (Bq/kg h) or surface area normalised units (Bq/m^{2}h) at equilibrium. If the total ^{226}Ra activity in the rock is known, it is possible to simply estimate the emanation fraction (or, emanation coefficient) as the ratio of Rn exhalation to total Rn production in the rock (equal to the ^{226}Ra activity). Care needs to be taken, however, since if the ^{226}Ra or ^{238}U content is measured with γ-spectroscopy using the γ-lines of the ^{214}Pb/^{214}Bi radon daughters, the activity will be underestimated. This is because one is only measuring the ingrowth of daughters from trapped ^{222}Rn and the exhalation fraction needs to be explicitly considered in the estimate (Al-Jarallah et al. 2005).

In many cases for the data reported in the literature, samples are crushed and sieved to small size fractions to reduce equilibration time, or otherwise simplify interpretation. Measurements are mostly made on dry, or nominally unsaturated samples as they would be used in construction materials, although some are reported for saturated, or partially water saturated states (see e.g. Sakoda et al. 2011). Some literature data are reproduced in Figure 2-3, Figure 2-4, and Figure 2-5 for different granitic rock types. In general, there is a significant spread of emanation coefficients reported, although the data mostly fall in the range 1–30 %. Figure 2-3 shows emanation coefficients from some crushed samples (< 0.5 mm) of porphyritic biotite granite taken from Pereira et al. (2017)[5] for Almeida, in central Portugal (henceforth, PLM17).
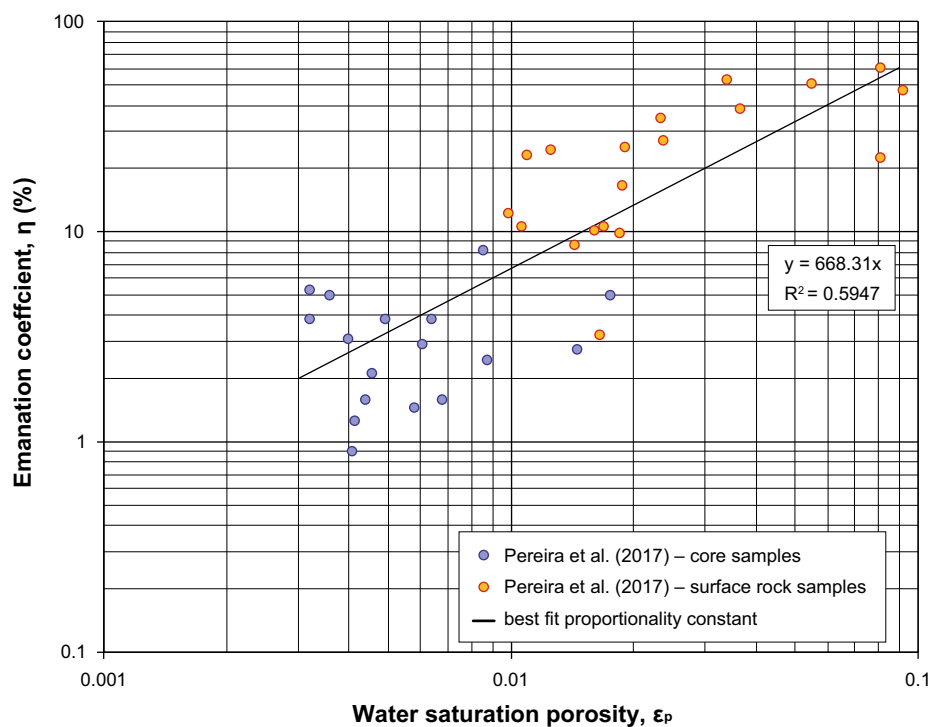
---

[4] See Addendum C for additional assumptions concerning the formula given by Liu and Neretnieks (1994). Addendum C is removed.

[5] The data were digitised from a screen capture of the original Figures in the pdf version of the article using a desktop version of the WebPlotDigitizer tool (https://automeris.io/WebPlotDigitizer/)

SKB R-21-16

This data set is interesting in that the water saturation porosity of the rock was measured as well as the [226]Ra content. The [226]Ra activity was estimated from the [214]Bi peak (1764.5 keV) using γ-spectroscopy assuming secular equilibrium. It is not clear, however, whether the reported [226]Ra measurements are corrected for the [222]Rn emanation loss. Some of the core samples taken from the deep borehole at Almeida are hydrothermally altered, while others are sampled from surface outcrops of the same rock type. The emanation coefficient measured by Pereira et al. (2017) appears to be positively correlated with water saturation porosity in Figure 2-3 (measured prior to crushing), and negatively correlated with Ra-content in Figure 2-4. The negative correlation of the PLM17 data with Ra-content is much weaker than the correlation with porosity. The authors speculate that the negative correlation may be partly due to the data representing two distinct sub-populations and that surface samples with low Ra-content may be more strongly weathered and thus depleted of uranium content. While a clear proportionality between [226]Ra content and [222]Rn exhalation rate is expected, the correlation between [226]Ra content and the [222]Rn emanation coefficient may or may not be mechanistic and related to alteration status and increased porosity with greater weathering.

The data shown in Figure 2-5, on the other hand, appear to show a weak positive correlation with Ra-content. The data in this Figure are from various sources including: Al-Jarallah et al. (2005) who studied granite tablets used as construction materials (AJRM05); Baretto (1971) studied crushed samples of various US granites from different geographical locations (B71); and data compiled by Jelinek and Eliasson (2015) for macadam derived from Swedish granite, veined gneiss, and gneiss granite (JE15). The remaining data (blue symbols in Figure 2-5) are an assortment including: Polish granite and gneiss granite (Przylibski 2000); core samples of porphyritic biotite granite from Pereira et al. (2017); granite, granodiorite, quartz monzonite gneiss, and diorite from Sakoda et al. (2011); granite and other non-specified igneous rock from Hassan et al. (2009); granite samples from various countries as studied by Nicolas et al. (2014). Most of the data sets are based on measurements of finely crushed rock except those reported by Al-Jarallah et al. (2005) and Nicolas et al. (2014) which are based on intact tablets or core samples. The data reported by Jelinek and Eliasson (2015) are for comminuted macadam samples (cm-size) although otherwise relatively intact. There appears to be a relatively good correlation between [226]Ra content and emanation coefficient for the Swedish rocks as can be seen from the best fit correlation in Figure 2-5, although the number of samples is quite small.

Figure AB-3. co-variation of estimated emanation coefficient relative to water saturation porosity for porphyritic biotite granite (Pereira et al. 2017). The high porosities of the surface rock samples appear to be associated with higher degrees of alteration, although this is not stated unambiguously in the reference. Note: data are scanned from original reference.
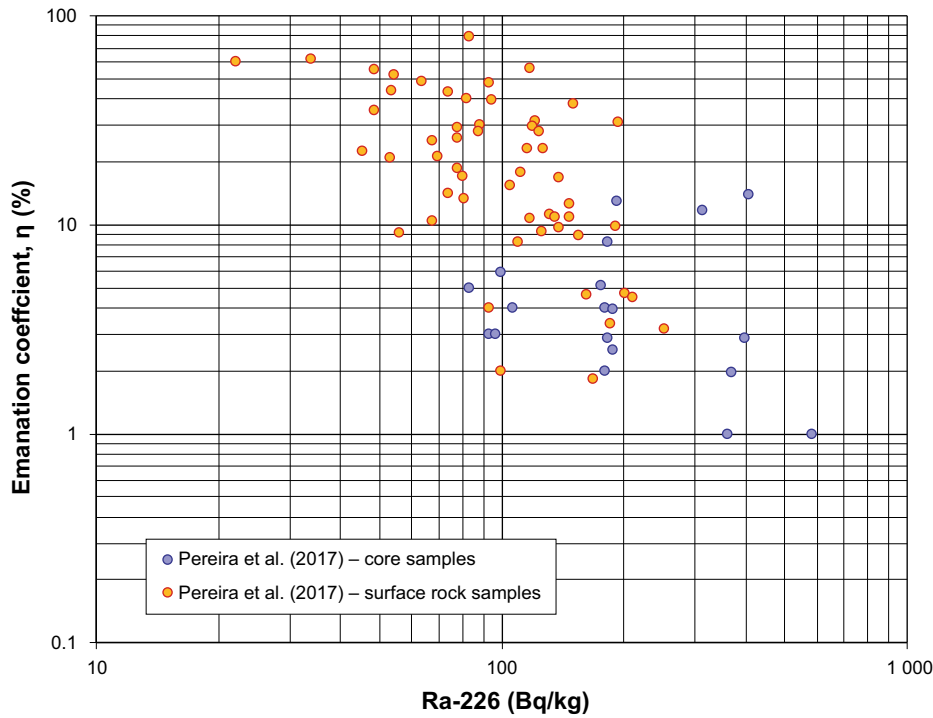
Figure AB-4. *co-variation of estimated emanation coefficient relative to ^{226}Ra content for porphyritic biotite granite (Pereira et al. 2017). Note: data are scanned from original reference.*
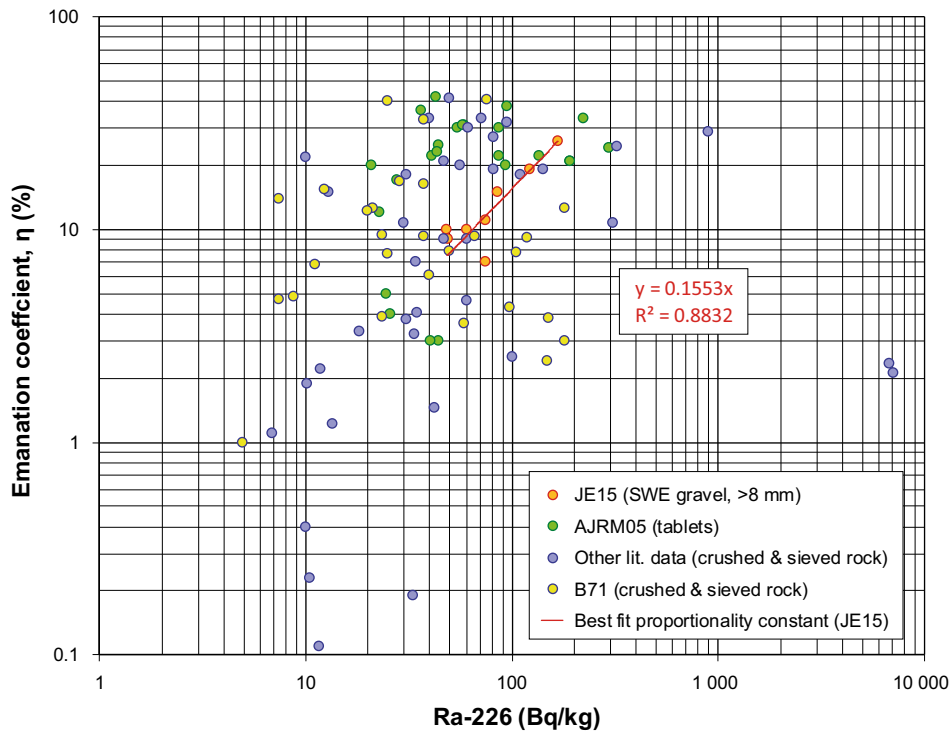
Figure AB-5. *co-variation of estimated emanation coefficient for ^{222}Rn relative to the ^{226}Ra content reported by various authors (see text for additional details) as well as samples of Swedish granite and gneiss-granite macadam, labelled JE15 (Jelinek and Eliasson 2015). A fit is also shown for the JE15 data set showing an apparent proportionality of the emanation coefficient with Ra-content.*

SKB is responsible for managing spent nuclear fuel and radioactive waste produced by the Swedish nuclear power plants such that man and the environment are protected in the near and distant future.

skb.se